Title	Structure and Solid-state Phase Transitions of Micron-sized Single Crystals of Polyoxymethylene Revealed by Microprobe Technique of Vibrational Spectroscopy
Author(s)	森下, 浩史
Citation	大阪大学, 1994, 博士論文
Version Type	VoR
URL	https://doi.org/10.11501/3080043
rights	
Note	

STRUCTURE AND SOLID-STATE PHASE TRANSITIONS OF MICRON-SIZED

SINGLE CRYSTALS OF POLYOXYMETHYLENE REVEALED BY MICROPROBE

TECHNIQUE OF VIBRATIONAL SPECTROSCOPY

A Doctoral Thesis

by

Hirofumi Morishita

Submitted to the Faculty

of Science, Osaka University

May, 1994

Approvals

May, 1994

This thesis is approved as to

style and content by

小林 雅通

Member-in-chief

寺寺明夫

Member

小高 忠一男

Member

吉木 俊夫

Member

田代孝乙

Member

Acknowledgements

森下 浩史

Hirofumi Morishita

May, 1994

CONTENTS

Chapter 1.

General Introduction

Poly(oxymethylene), $\{CH_2O\}_n$, (abbreviated as POM) called polyacetal resin is a typical high-performance engineering plastics exhibiting excellent properties such as high mechanical strength and impact resistance. Recently it has become a center of attraction as a metal-substitute, and the amount of its production and consumption in Japan as well as in the world market has been increasing rapidly.

Poly(oxymethylene) is a typical crystalline polymer having a high melting point and high degree of crystallinity that easily reaches higher than 80%, while its amorphous region has a low glass transition temperature. This biphasic nature of POM imparts the features of a well-balanced strength and impact resistance as an excellent engineering plastics.

This polymer crystallizes into two modifications: A stable trigonal form (t-POM) with the space group $P3_1-C_3^2$ or $P3_2-C_3^3$ and a metastable orthorhombic form (o-POM) with the space group $P2_12_12_1-D_2^4$. The stable trigonal form is exclusively obtained through ordinary crystallization processes from the melt or dilute solution. Fine powder samples recovered from very dilute solution are known to consist of sub-micron size single crystals of a hexagonal plate-like shape, in which the polymer molecules are folded with a stem length of about 10 nm corresponding to the lamellar thickness.[1,2] These crystals belong to a typical folded-chain crystal (FCC).

Extended-chain crystals (ECC), another type of the crystal morphology of t-POM, were obtained by Staudinger et al.[3,4] as hexagonal prism-like crystals consisting of extended-chain molecules via the polymerization of formaldehyde in aqueous alkaline solution under atmospheric pressure. However, Staudinger did not describe details of the extended molecules comprising those crystals of t-POM of an ECC type.[3,4] Baccaredda et al.,[5] on the other hand, obtained fibrous crystal of t-POM of an ECC type by polymerizing trioxane with a boron trifluoride etherate catalyst. Furthermore, about two decades ago, Iguchi et al.[6,7] succeeded in preparing needle-like, feather-shaped single crystals of t-POM of an ECC-type through heterogeneous cationic polymerization of trioxane at 50°C. The needle-like crystals thus obtained were identified as polymer whisker having an extremely high crystalline perfection. Recently we obtained rod-like crystals of t-POM also of an ECC-type through the same polymerization procedure but carried out at 55°C.[8] Most of commercial POM samples are obtained as a trigonal modification (t-POM) between the above mentioned two extreme cases of the ECC and FCC types, depending on thermal- and mechanical processing conditions.

The orthorhombic modification (o-POM) was prepared first by Mortillario et al.[9] in a fine powder form, although details of the preparation conditions were not reported. Previous vibrational spectroscopic studies on o-POM were performed without polarization data.[10-13] Thus the results were ambiguous because this metastable form (o-POM) readily transforms to a stable trigonal form (t-POM), for example, just by drawing or rolling o-POM specimens to induce molecular orientation. Iguchi et al.[14]

obtained micron-size single crystals of o-POM in two different forms: Moth-shaped plate-like single crystals having a characteristic shape like "moth" and rod-like single crystals.

Vibrational spectroscopic studies of crystalline polymers reported so far were made mostly on unoriented or uniaxially oriented partially crystalline samples. Polarization measurements on one piece of single crystals were never undertaken, presumably because the preparation of single crystals with the size large enough for infrared (IR) and/or Raman measurements was extremely difficult.

However, due to the recent development of micro-probe techniques in IR and Raman spectroscopies, it became possible to measure polarized spectra of a small specimen with the width of as small as a few μm. Although the crystallite size of most crystalline polymers is still one order of magnitude smaller than the above mentioned size limit, fortunately we were able to use micron-size single crystals of both t-POM and o-POM suitable for the microprobe IR and Raman measurements. This, in turn, enabaled us to measure micro-IR and micro-Raman spectra of both t-POM and o-POM, which could be full interpreted including the assignment of the E_2 modes of t-POM unobservable in other ordinary POM samples. Moreover, we could follow the process of solid-state phase transitions of POM by simultaneous measurements of the spectral changes combined with optical microscopic observation on a single specimen, and obtain new information on the molecular mechanism of the phase transitions.

The important subject of this thesis is to elucidate the molecular mechanisms of the thermodynamic stability of the two crystal modifications of POM and of the o-POM → t-POM thermal and

the t-POM → o-POM pressure-induced solid state transitions occurring between the two crystal phases (refer Fig. 4.1), which little have been known in detail so far. A very new point is that the spectral measurements have been conducted on micron-size single crystals. To this end, we have to develop new techniques for the microprobe IR and Raman measurements, and have to solve some fundamental problems concerning the optics involved in these new methods.

This thesis consists of the following five chapters and two appendices.

Chapter 2 deals with analyses of molecular vibrations of o-POM based on the spectral data taken on single crystalline specimens of the μm size. So far no polarized spectral data were available on o-POM, because this modification was metastable and easily transformed into a stable trigonal modification through the application of mechanical stress to produce oriented samples suitable for spectral measurements.

In this Chapter 2 we thus are concerned with polarized Raman spectra taken on single crystals of o-POM by means of Raman *microprobe* technique.[16-18] Polarized micro-IR spectra were also obtained on the same single crystalline specimens. The vibrational assignments were established on the basis of these newly obtained spectral data with the aid of the normal modes calculation. The determination of the crystallographic axes in the moth-shaped single crystal of o-POM was an another subject. In an ordinary case this can be done by X-ray or electron diffraction methods. Unfortunately the specimen was too small to be subjected to the X-ray diffraction, and the electron

diffraction was also unapplicable because POM was easily degraded by electron beam. Then to do this we had to get over these difficulties through other routes.

We will describe in Chapter 2 the details of these procedures and results.

On the other hand, Chapter 3 deals with the vibrational analyses of t-POM crystal based on spectral data taken on a single crystal and a well-oriented bulk specimen of t-POM. We obtained moth-shaped t-POM single crystals, through thermal phase transition of o-POM single crystals to t-POM single crystals which have optical clearness and large size suitable for the micro-Raman measurements.

Again polarized Raman spectra were taken on t-POM single crystals by means of Raman microprobe technique, and the vibrational assignments were investigated on the basis of the polarization characteristics of these bands. Then assignment of the E_2 modes (see Table 3.1) of t-POM is one of the main subjects, since the modes were little known about them so far. To do this, we performed ordinary right-angle polarized Raman measurements on well-oriented and transparent pressurized superdrawn filaments of t-POM. We will investigate the vibrational assignments of t-POM on the basis of the polarization data.

Chapter 4 deals with the thermal phase transition from the orthorhombic to the trigonal modification. It is quite evident that metastable o-POM transforms irreversibly to stable t-POM by heating or by applying mechanical stress. However, details of thermodynamic behavior and structural features of the phase transition, even DSC thermogram, have not been clarified so far.

Using rod-like single crystals of o-POM as the starting sample, we succeeded to measure the DSC thermogram (on heating) with small but distinct endothermic peak due to the o-POM → t-POM phase transition, from which we were able to evaluate the enthalpy and entropy of the phase transition.

We considered also role of crystal morphology of the starting sample in the phase transition. The crystal morphology before and after the transition is investigated by a new spectroscopic method based on the morphology dependent frequency shifts of the parallel infrared bands.[19,20] Orientational changes of the POM lattice on the phase transition are investigated by polarized Raman microprobe technique on one single-crystal specimen.

Chapter 5 deals with the effect of the morphological structure in the pressure-induced phase transitions from t-POM with 1.49 density to o-POM with 1.54 density, by using needle-like single crystals (ECC) and solution grown lamella crystals (FCC) of t-POM as the starting material. One aim is to know how the phase transition behavior is influenced by the crystal morphology (ECC or FCC) of the starting t-POM sample. The amounts of the orthorhombic phase generated from the two starting t-POM samples under various conditions were evaluated, and the results were compared with each other. Another important subject is to confirm whether the crystal morphology of the starting sample is remained or changed on the phase transition. The morphology dependent frequency shifts of the parallel IR bands are used as a key for solving this problem. The stress tensor elements that induce the phase transition is discussed.

Chapter 6 summarizes the main results and conclusions

derived from the present work.

REFERENCES

1 W. J. Barnes and F. P. Price, Polymer, 5, 283 (1964)

2 D. C. Bassett, F. R. Dammont and R. Salovey, Polymer, 5, 579 (1964)

3 H. Staudinger, R. Singer, H. Johner, M. Lülty, W. Kern, D. Russidis and O. Schweitzer, Z. Krist., 70, 193 (1929)

4 H. Staudinger, R. Singer, H. Johner, M. Lülty, W. Kern, D. Russidis and O. Schweitzer, Ann. Chem., **474**, 145 (1929)

5 M. Baccaredda, E. Butta, P. Guisti and F. Morelli, J. Polymer Sci., **C4**, 953 (1963)

6 M. Iguchi, Br. Polym. J., **5**, 195 (1973)

7 M. Iguchi and I. Murase, J. Crystal Growth, **24/25**, 596 (1974)

8 H. Morishita, M. Kobayashi, H. Kuwahara, M. Shimomura and M. Iguchi, Sci. Bull. Fac. Educ., Nagasaki Univ., No. 41, 13 (1989)

9 L. Mortillario, G. Galliazzo and S. Bessi, Chem. Ind. (Milan), **46**, 139 (1964)

10 V. Zamboni and G. Zerbi, J. Polym. Sci., **C7**, 153 (1966)

11 G. Zerbi and G. Masetti, J. Mol. Spectrosc., 22 284 (1967)

12 G. Zerbi and P. J. Hendra, J. Mol. Spectrosc., 27, 17 (1968)

13 F. J. Boerio and D. D. Cornell, J. Chem. Phys., 56, 1516 (1972)

14 M. Iguchi, Polymer, **24**, 915 (1983)

15 M. Kobayashi, Y. Itoh, H. Tadokoro, M. Shimonura and M. Iguchi, Polym. Commun., **24**, 38 (1983)

16 M. Kobayashi, H. Morishita, T. Ishioka, M. Iguchi,

M. Shimomura and T. Ikeda, J. Mol. Struct., **146**, 155 (1986)

17 H. Morishita, M. Kobayashi, M. Shimomura and M. Iguchi, Sci. Bull. Fac. Nagasaki Univ., **39**. 47 (1988)

18 H. Morishita and M. Kobayashi, Rep. Prog. Polym. Phy, Jpn., **30**, 139 (1987)

19 M. Shimomura and M. Iguchi, Polymer,**23**, 509 (1982)

20 M. Shimomura, M. Iguchi and M. Kobayashi, Polymer, **29**, 351 (1988)

Chapter 2.

Structure and Vibrational Spectra of Single Crystals of
Orthorhombic Poly(oxymethylene)

2.1. Introduction

Poly(oxymethylene), $(CH_2O)_n$, is usually obtained in a
trigonal crystal modification (t-POM, the stable phase) that
consists of 9/5 (or 29/16) helical molecules.[1-3] Three decades
ago, another modification which belongs to an orthorhombic system
(o-POM) consisting of 2/1 helical molecules, was first obtained
as a powder form by Mortillario et al. through polymerization of
formaldehyde at a very slow rate in alkaline aqueous solution.[4]
Thereafter, the crystal structure and the molecular conformation
of this modification have been investigated by means of X-ray
diffraction[5] and vibrational spectroscopy.[6-9]

However, all the previous studies of o-POM have been
performed on powder samples, because the modification is a
metastable phase which transforms immediately to the stable
trigonal modification when the specimens are heated above 69°C[10]
or subjected to mechanical deformation (drawing and/or
rolling)[6,11] for generating molecular orientation. Therefore, no
polarization data of infrared and Raman spectra of o-POM have
been obtained. Determination of infrared and Raman polarizations
is of essential importance for detailed vibrational analyses.

Recently, Iguchi found that in certain POM samples prepared
by a heterogeneous cationic polymerization of trioxane which was
originally designed to prepare needle-like single crystals of t-

POM[12-15] small amount of o-POM crystals was contained.[16]   In the optical microscopic viewfield, the o-POM crystals were seen as micron-sized thin plates having a specific shape like "moth" (Fig. 2.1).   They showed clear optical birefringence, characteristic of a single crystal, and were identified as the orthorhombic modification of POM by means of the Raman microprobe technique by Kobayashi et al.[17]   They were recognized as single crystals of o-POM obtained for the first time.

Besides the moth-shaped single crystals, crystalline particles of o-POM having a different habit were generated as a by-product in the course of a heterogeneous cationic polymerization of trioxane for preparing t-POM crystals.   X-ray analysis has revealed that the particles consist of many rod-like single crystals of o-POM gathering in a sphere.[16]

Although previous workers[6-9] have made vibrational assignments of o-POM on the basis of unpolarized infrared and Raman data taken on powder samples, with the aids of normal mode calculations, there are still uncertainties because of the lack of polarization data.   Therefore, measurements of the infrared and Raman polarization are required for the establishment of vibrational assignments.

In this chapter vibrational assignments of o-POM are discussed on the basis of polarized IR and Raman spectra taken on moth-shaped and rod-like single crystals.

2.2. Experimental

2.2.1. Samples

Two kinds of o-POM samples were supplied from the Research Institute for Polymers and Textiles of International and Industry

in Japan.   One was a fine powder consisting of needle-like t-POM single crystals containing ca. 10% of moth-shaped o-POM single crystals (Sample I).   The other was films bearing a number of o-POM particles on the surface of t-POM thin films.   The o-POM particles separated from the t-POM films[16] were used as a pure o-POM sample (Sample II).

The source of moth-shaped o-POM crystals has been described in refs. 16 and 17.   Moth-shaped single crystals of o-POM were mixed in the needle-like t-POM single crystals (marked with arrow in Fig. 2.1) obtained in a special bach which had originally been designed to prepare needle-like single crystals of t-POM by a heterogeneous cationic polymerization of trioxane.[16]   As shown in Fig. 2.1 in a microscopic viewfield, there is observed a moth-shaped crystal having a twin habit and a clear crystal edge with dimensions of about 50 μm width and 2 μm thickness or less. Parallel striations running on the plate face of the crystal are observed.

Moth-shaped o-POM single crystals to be subjected to the micro-Raman measurement were separated from the major components of t-POM needle-like crystals by dispersing a small amount of powder sample in a water/methanol mixture put on a slide glass plate.   After evaporation of the solvent, well-separated moth-shaped crystals were searched under optical microscope and moved on another slide glass plate.

Sample II consists of spherical particles with diameters of 0.5 mm or less, each particle comprising a number of rod-like single crystals (having about 20 μm in length) packed at random. From Sample II, we could pick out one piece of rod-like single crystal whose long axis was parallel to the c axis, judging from
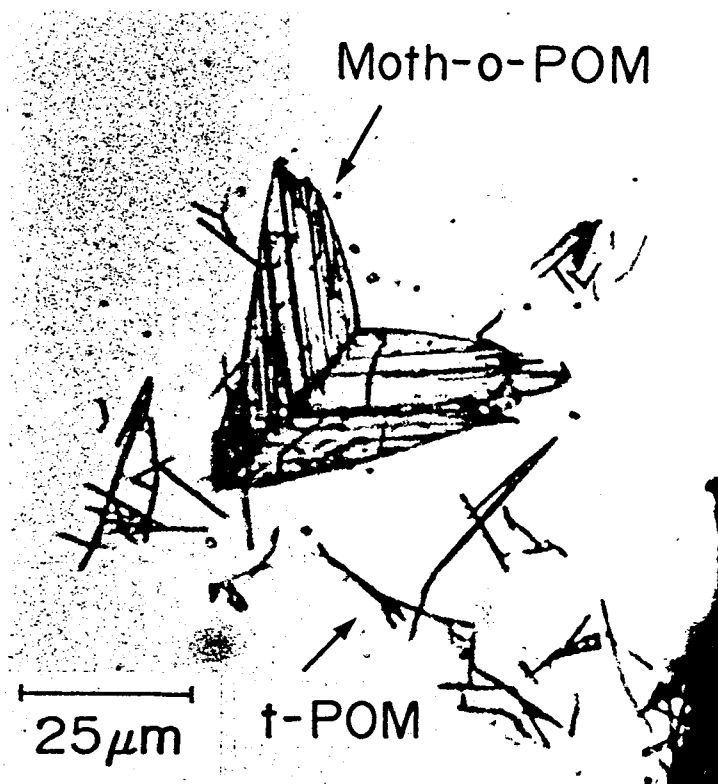
Fig. 2.1.   Photomicrograph of moth-shaped o-POM single crystal.

the morphology and the optical birefringence of the crystal.

These o-POM single crystals must be handled carefully, because o-POM samples transforms easily to the stable t-POM phase by crushing the particles with an agate mortar or by rolling. These treatments were made under cooling with liq. N_2 in order to avoid as much as possible the transition to the trigonal form.

2.2.2. Raman Spectral Measurements

Ordinary unpolarized right-angle Raman spectra were taken on Sample II with a JASCO R-500 double monochromator using the 514.5 or 488.0 nm line (Ar^+ laser) as the excitation source. The entrance and exit slit widths of the monochromator were fixed at 100 μm corresponding to the spectral resolution about 2.5 cm^{-1}. For the measurements at low temperatures an Oxford continuous flow cryostat was used. A part of Sample II enclosed in a thin-walled glass capillary was mounted on the cold finger of the cryostat. For the measurement of very weak Raman bands at high magnification, a naked o-POM particle fixed at the top of a steel needle was used. The slits were fixed at 80 μm (about 1.5 cm^{-1} of resolution). In order to remove fluorescence background, the sample was laser-quenched for 10 h before the measurement.

2.2.3. Micro-focus Raman Measurements on Single Crystals

Micro-Raman spectrum was taken on the micron-sized moth-shaped o-POM single crystal with a JASCO NR-1000 double monochromator using the 514.5 nm line excitation source.[16] The instrument consists of an epi-illumination optical microscope (Olympus HB-2), a detector system, and a data-processing system. The optical system for irradiating the sample by the incident

laser beam and that for collecting the scattered light in the
micro-Raman instrument are illustrated in Fig. 2.2.   The
incident beam polarized in a particular direction (adjusted by a
half-wave length plate) is focused at a selected position of the
sample on the microscope stage through an objective selected from
the objectives Olympus Neo Spla x10, x20, x50 and x100, whose
optical constants are given in Table 2.1.   The incident laser
beam can be focused until 1 μm diameter by using a x100 objective
(with the numerical aperture N.A. = 0.90), the theoretical
spatial resolution limit was calculated as about 1 μm.   The
backward scattered light is collected by the same objective lens,
passes through a beam splitter, and enters the monochromator
through a telemeter lens (Olympus A 70-210 F4).   Before the
entrance slit of the monochromator there are an analyzer and a
polarization scrambler, as in the case of the ordinary Raman
polarization measurement.

The use of a sharp focusing objective causes spurious
polarizations having components that parallel to the depth

Table 2.1.   The optical constants of the objectives

Magnification	N.A.	θm	f	F.L./mm
x10	0.30	17.5°	1.66	18.0
x20	0.46	27.4°	1.09	9.0
x50	0.80	53.1°	0.63	3.6
x100	0.90	64.2°	0.56	1.8

N.A.(Numerical Aperture) = $\sin \theta_m$

θ_m; the opening angle to an aperture

$f = \dfrac{1}{2\sin \theta_m}$
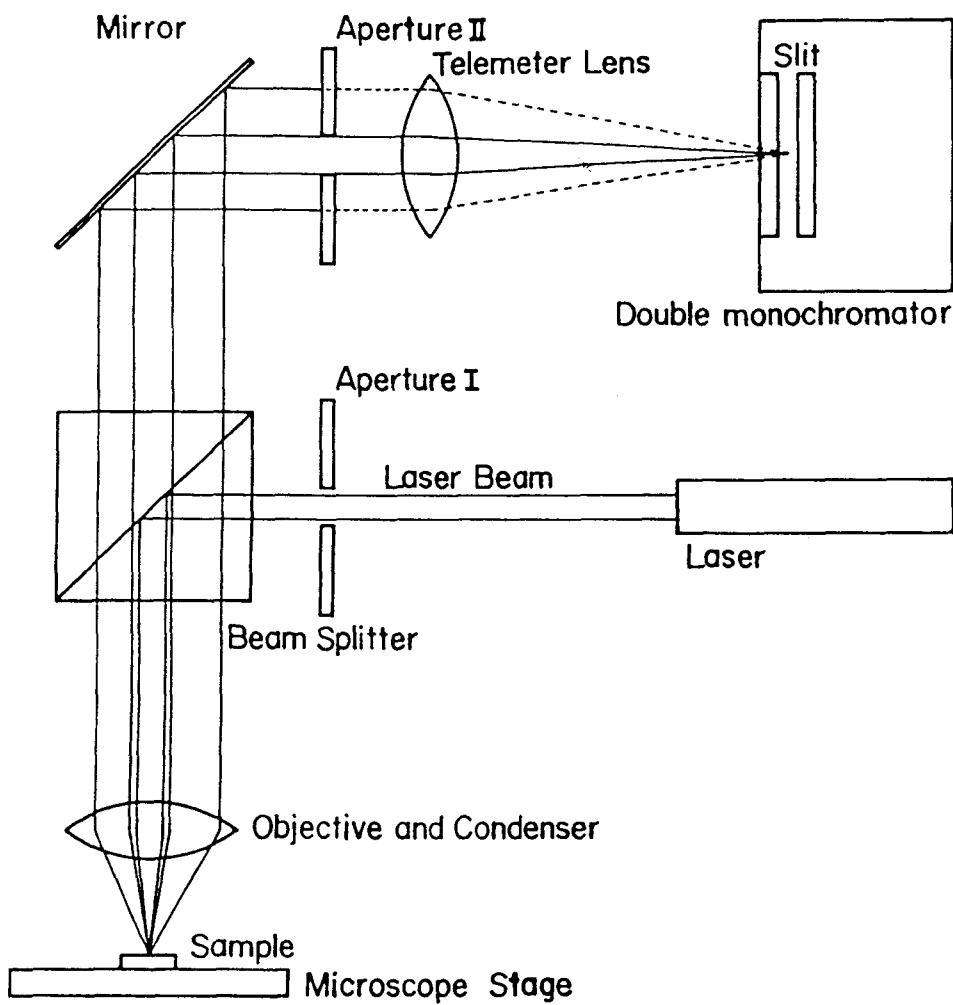
Fig. 2.2. Schematic diagram of optical system for Raman microprobe.

direction in both the incident and scattered lights passing
through the peripheral area of the objective, arising
polarization scrambling. Especially, the degree of polarization
scrambling increases when a high magnification objective (say
x100) is used. For the purpose to minimize the effect, use of a
low magnification of objective or insertion of apertures into the
collimation system is needed. For quantitative estimation of the
polarization scrambling, the spectral change with change in
aperture size was measured using the same objective. By this way
we are able to compare the light intensities scattered from the
same area of the sample. The aperture I with diameters of 1 mm
and/or the aperture II with 2 mm are inserted in order to reduce
the polarization scrambling of the incident and scattered lights,
respectively.

Polarized micro-Raman spectra of rod-like and moth-shaped
single crystals of o-POM were taken with different scattering
geometries under various optical conditions. We defined the
sample-fixed Cartesian coordinates; for the moth-shaped crystal,
X is parallel to the striation on the plate face of the crystal,
Y perpendicular to X within the plate surface, and Z normal to
the plate surface. For the rod-like single-crystal, X is
parallel to the long-axis (namely, parallel to the
crystallographic c axis), and Y and Z normal to it.

2.2.4. Infrared Spectral Measurements

The mid-infrared spectrum of Sample II was obtained by Nujol
mull method with a JASCO A-3 spectrometer. The spectral slit-
width at 1600 cm^{-1} was 2.6 cm^{-1}. Polarized infrared spectra were
obtained on oriented films prepared from Sample II by rolling at

low temperature. Polarized far-infrared spectra of the same film were taken with a Hitachi FIS-3 grating spectrometer.

Microfocus infrared spectrum was measured on a plane-oriented film of moth o-POM single crystals using a infrared microscope attached to a JASCO DS-402G spectrometer. The plane-oriented sample was prepared as follows; about two hundreds pieces of micron-sized crystals were picked up, and aligned as close as possible to fill a selected area of 1 x 3 mm^2 on the surface of a KBr window. The plate faces of the most crystals were located parallel to the window surface but the X directions were randomly distributed, forming a plane orientation. With a small amount of liquid paraffin (in order to remove scattering of the infrared radiation), they were covered by another KBr window. The spectrum was compared with that of Sample II (powder).

Polarized micro-focus FT-IR spectra taken on one moth-shaped o-POM single-crystal were measured with a JASCO JANSSEN with a DTGS detector adopting ATOS (aperture through optical system). For the measurement, a piece of single-crystal having a suitable size and thickness was selected, and put on a KCl window placed on the sample stage of the microscope. Thereafter, the polarized micro-focus FT-IR spectra by the transmission method were obtained with the spectral resolution of 2 cm^{-1} using the aperture that selected the available area 40 x 25 μm^2 of the crystal.

2.3. Crystal Structure of o-POM and Molecular Vibrations

As shown in Fig.2.3, two 2/1 helical molecules pass through the unit cell of the o-POM lattice,[5,6] with the lattice constants a = 4.77 Å, b = 7.65 Å, c = 3.56 Å, and the space group $P2_12_12_1$-
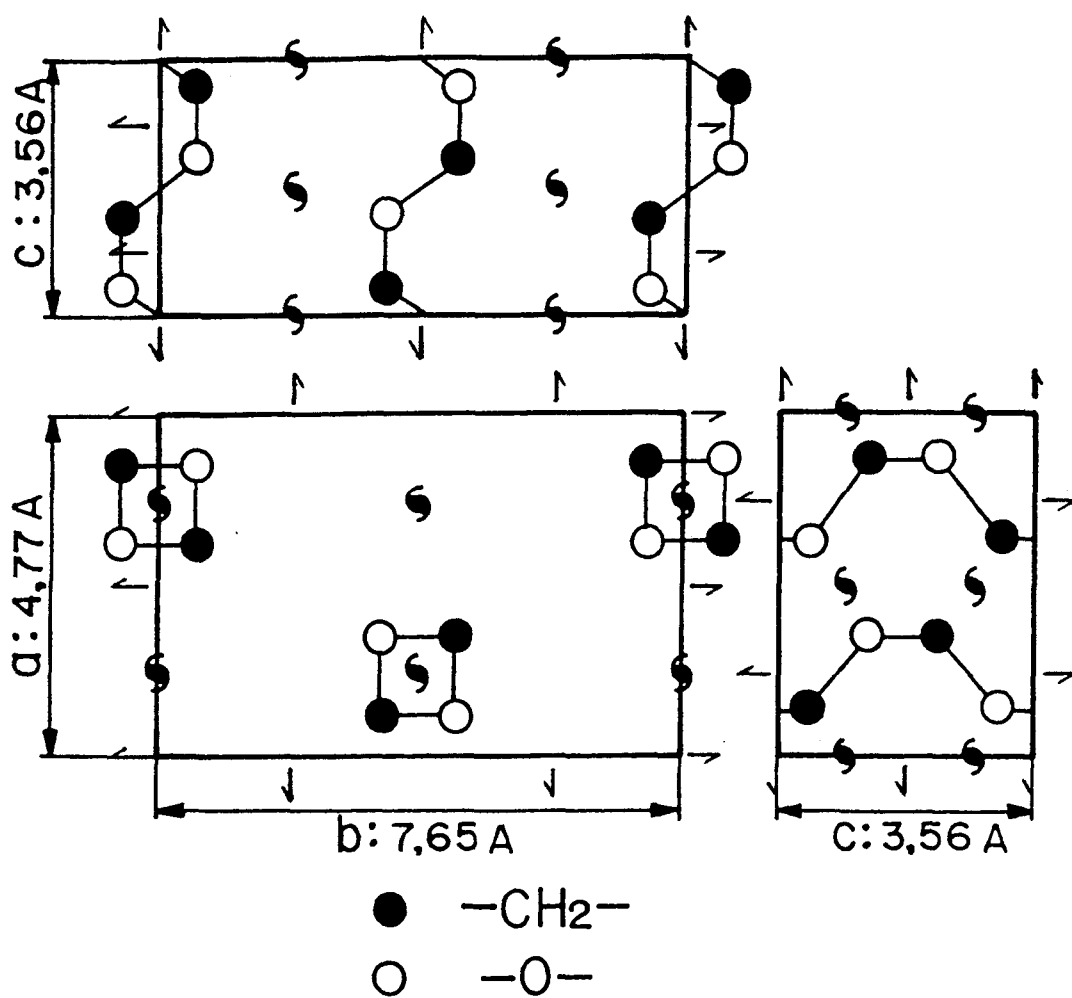
Fig. 2.3. Crystal structure of o-POM. (redrown after Carrazzolo
and Mammi, ref. 5)

$D_2{}^4$. The optically active vibrational modes are treated by the factor group isomorphous to the point group D_2. The number of the optically active normal modes and the infrared and Raman polarizations of each symmetry species are summarized in Table 2.2. The line group for one 2/1 helical molecule also belongs to D_2. The site group is isomorphous to the C_2. The correlation of the symmetry species among the line group, site group and space group is given in Table 2.3. The zone-center internal modes in o-POM crystal are classified into the four symmetry species: $10A + 10B_1 + 10B_2 + 10B_3$.

As typical examples of the vibrational modes of o-POM, the CH_2 symmetric stretching modes of the A, B_1, B_2 and B_3 species are shown in Fig. 2.4. Since two chains pass through the unit cell, each molecular mode of the 2/1 helix splits into doublet by the intermolecular interactions (Davydov splitting); the A-B_1 and B_2-B_3 split pairs. As given in Table 2.2, the IR and Raman polarizations of the B_2-B_3 split components are the key for determining the orientation of the crystallographic axes in the moth-shaped o-POM single crystal.

Fig. 2.5 shows five zone-center external modes (lattice vibrations).

2.4. Results and Discussion
2.4.1. Vibrational Spectra of o-POM
2.4.1.1. Infrared Spectra of o-POM

The mid-infrared and far-infrared spectra for the powder sample (Sample II) were essentially the same as those reported by Zerbi et al.[5-7] Three split pairs observed at 1220 and 1237, 434 and 428, and 89 and 83 cm^{-1} have been assigned, respectively, to

Table 2.2. Factor group analysis of crystalline o-POM

Species	No. molecular modes	No. lattice modes	Polarization	
			IR	Raman
A	10	$2(R_c{}',T_c{}')$	Forbidden	$\alpha_{aa,bb,cc}$
B_1	10	$1(R_c{}')$	μ_c	α_{ab}
B_2	10	$1(T_a{}')$	μ_b	α_{ac}
B_3	10	$1(T_b{}')$	μ_a	α_{bc}

Table 2.3. Correlation diagram for factor group modes of orthorhombic poly(oxymethylene)

Line group D_2	Site group C_2	Space group D_2
A	$A(T_c)$	A (R)
B_1		$B_1(R,IR)$
B_2	$B(T_a,T_b)$	$B_2(R,IR)$
B_3		$B_3(R,IR)$
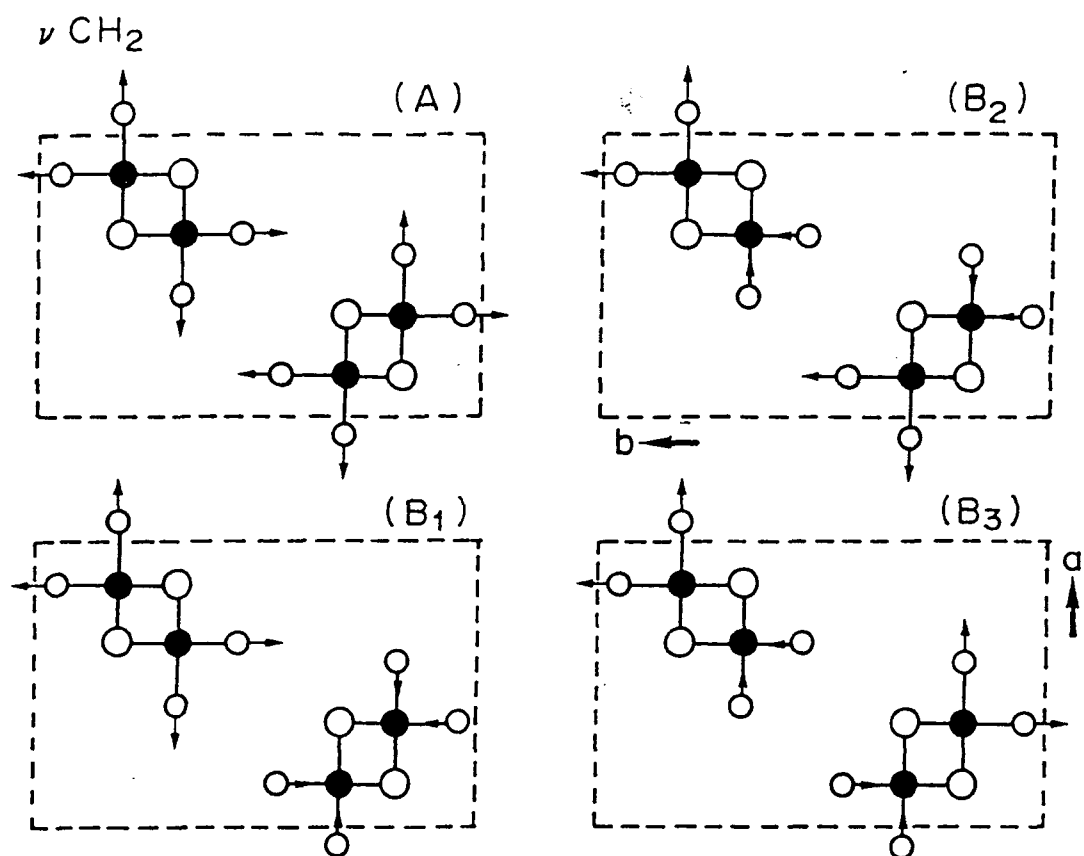
Fig. 2.4. CH$_2$ symmetric streching modes of o-POM crystal.
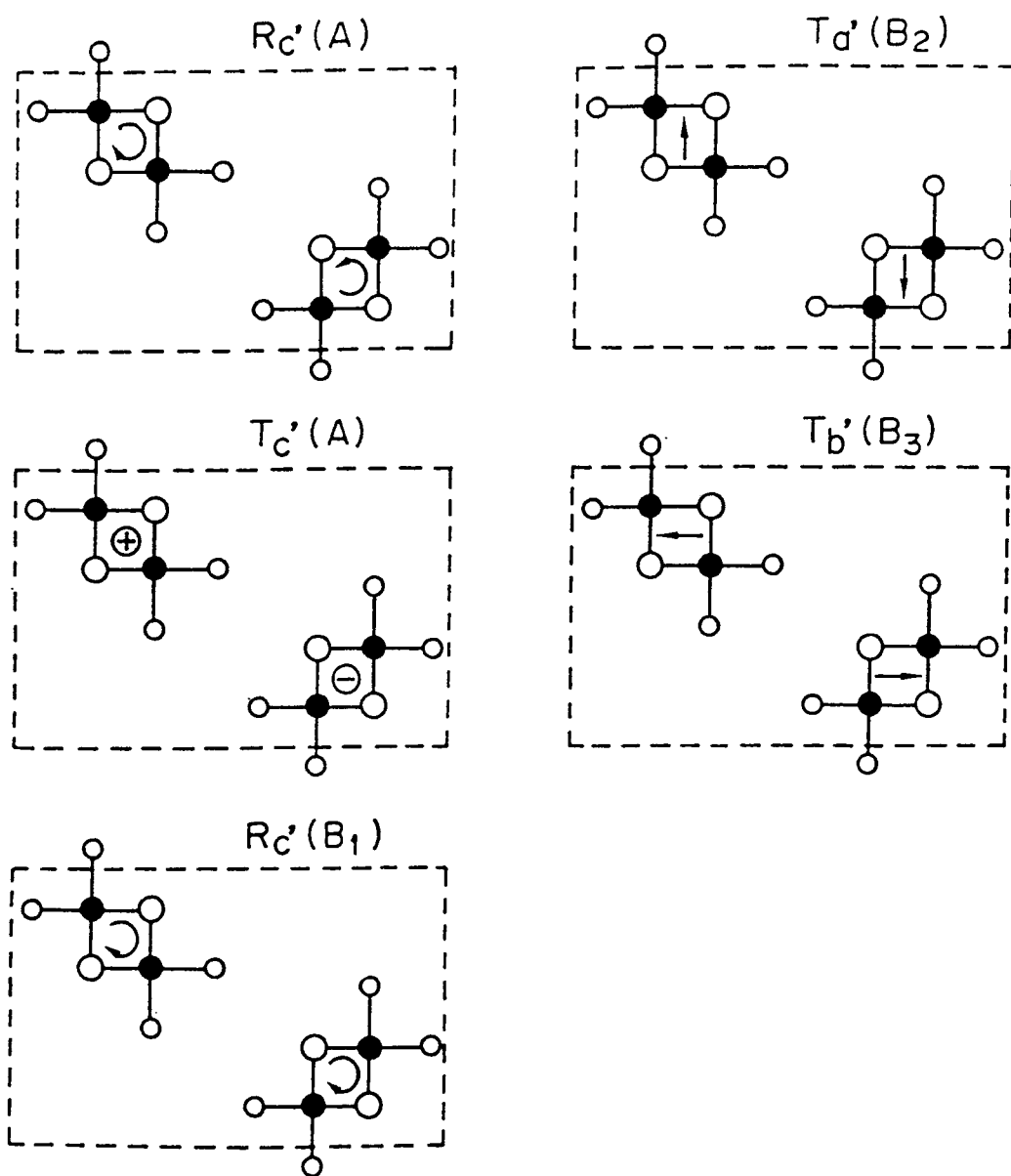
Fig. 2.5. Lattice vibrations of o-POM crystal

the 7th, 10th and T_a'-T_b' pairs of the B_2-B_3
splitting.[6,7,9,18-20]

Polarized infrared spectra taken on the oriented o-POM films
(see 2.2.4.) in the regions of 1600-300 and 400-80 cm^{-1} are shown
in Figs. 2.6 and 2.7, respectively. These spectra contain many
bands due to the t-POM phase (marked with arrows) generated on
the rolling process (see 2.2.1.). The infrared bands at 1488,
1430, 1290, 1220, 594, 428, 297 and 130 cm^{-1} were assigned to the
o-POM fundamentals.[6-9,20,21] Infrared polarizations of some o-
POM bands were determined for the first time from the spectra
although the extent of the molecular orientation is rather poor.
For example, the 297 and 130 cm^{-1} bands are c-polarized and
assigned to the B_1 species (see Table 2.2). On the other hand,
the bands at 1488, 1430, 1290, 1220, 594, and 428 cm^{-1} show
perpendicular polarization and are assigned to the B_2 or B_3
modes, although we are unable to distinguish the two species from
each other based on the present data alone.

2.4.1.2. Raman Spectra of o-POM

A few experimental data[8,17] on the Raman-active vibrations
of o-POM have been reported so far.[8,17] Doubling of the Raman
bands due to Davydov split has never been detected. Fig. 2.8
shows Raman spectrum of powder o-POM (Sample II) taken at liq. He
temperature. Although the spectrum is essentially the same as
that (at *room temperature*) reported by Zerbi et al,[8] many bands
associated with o-POM are newly detected at 1393, 1328, 1136,
952, 922, 915 and 897 cm^{-1}. The appearance of these weak bands
originates from sharpening of the bands on cooling and also from
high crystal perfection of the sample used. In the figure the
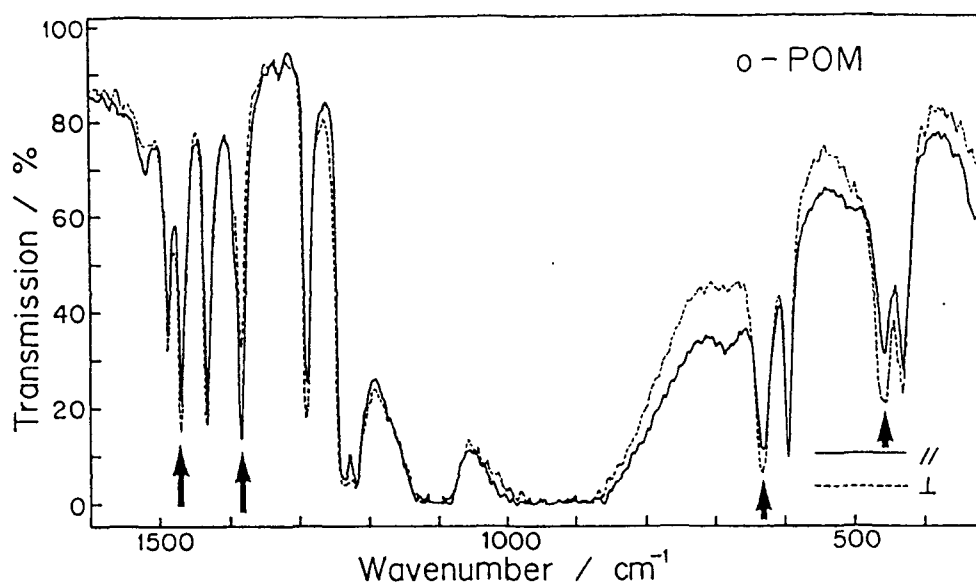
Fig. 2.6. Polarized mid-infrared spectra of oriented o-POM films
prepared by rolling Sample II; ——————— //c,

– – – – – ⊥c.
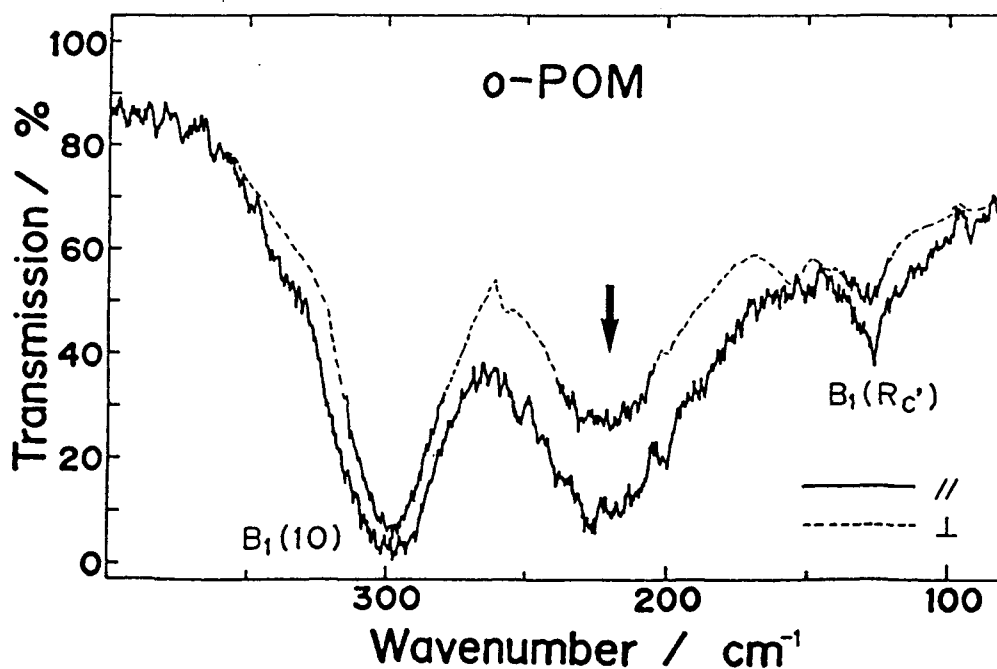
Fig. 2.7. Polarized far-infrared spectra of oriented o-POM films
prepared by rolling Sample II; ——————— //c

– – – – – ⊥c
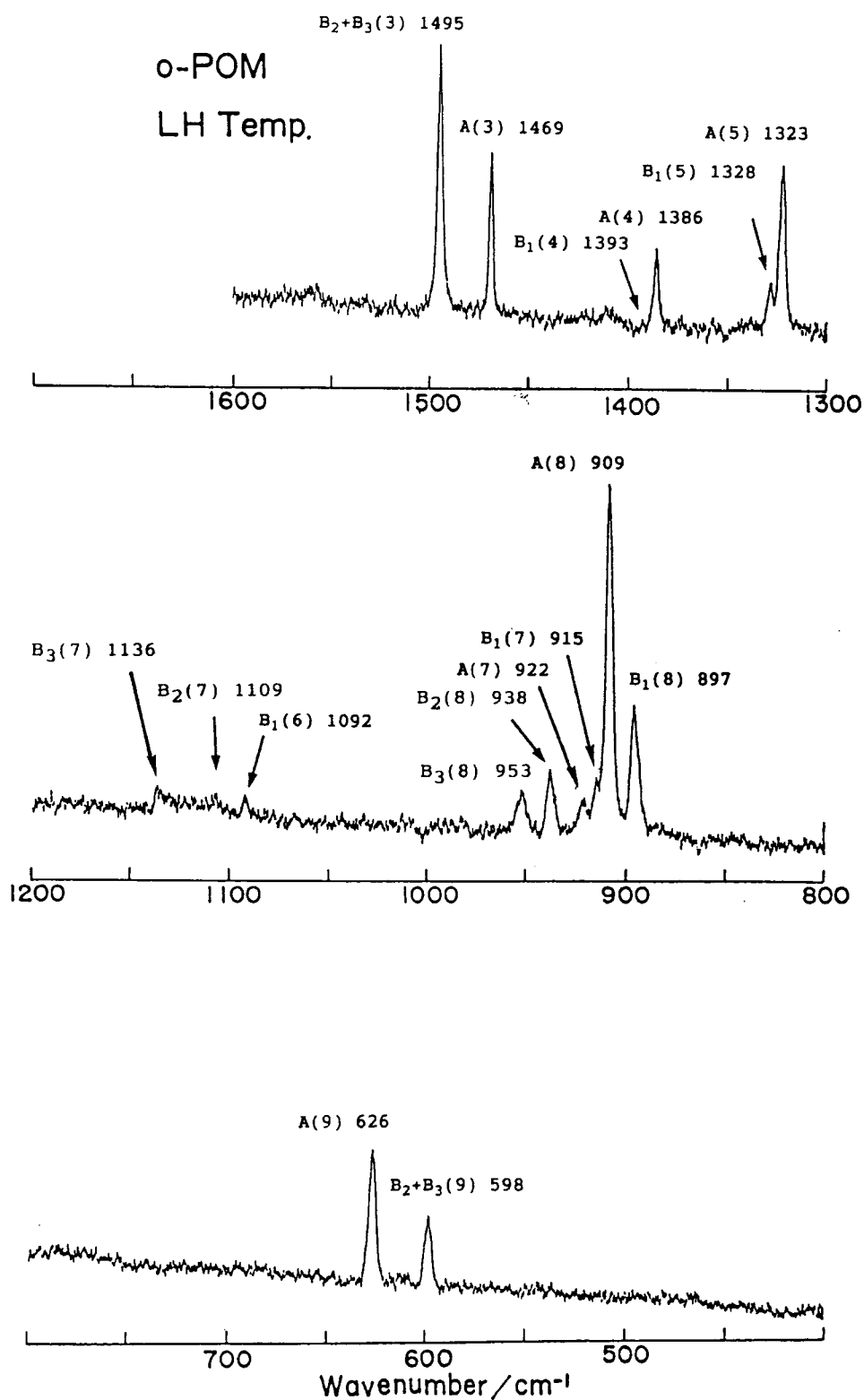
Fig. 2.8. Raman spectra of o-POM taken on a powder sample cooled at liquid He temperature.

assignments of the bands are described, which were decided in the present work based on the polarization measurement as will be discussed below.

In order to detect very weak bands and small band-splits, we tried to measure Raman spectrum on a naked o-POM particle (Sample II) with a high amplification with a narrow slit. The results (at room temperature) are shown in Figs. 2.9, 2.10 and 2.11. Several Raman bands due to o-POM were newly detected at 1429, 1290, 1286, 1243, 1221, 1112, 592.5, 434, 428, 294 and 82.5 cm^{-1} (marked with arrows), including Davydov split pairs of 1290-1286 cm^{-1} and 434-428 cm^{-1}.

Low-frequency Raman spectra of Sample II measured at various temperatures are shown in Fig. 2.12. The $T_c'(A)$ and $T_b'(B_3)$ lattice modes are observed at 38 and 80 cm^{-1}, respectively, at room temperature as reported by Cornell.[9] As shown in Fig. 2.13, these bands are shifted towards the high-frequency side with lowering temperature. Such a significant frequency shift is characteristic of lattice vibrations. The symmetry species of the lattice modes will be discussed in relation to their Raman polarization.

2.4.2. Polarized Micro-Raman Spectra of o-POM Single Crystals

In general, Raman polarization data give us important information for determining the assignments as well as the crystal orientation. Polarized micro-Raman spectra taken on a moth-shaped single crystal (Sample I) in the region 1500-500 cm^{-1} using an objective lens with x40 magnification are shown in Fig. 2.14, and in the 130-25 cm^{-1} region with x100 in Fig. 2.15. The strongest band at 909 cm^{-1} in the (XX) spectrum is assigned to
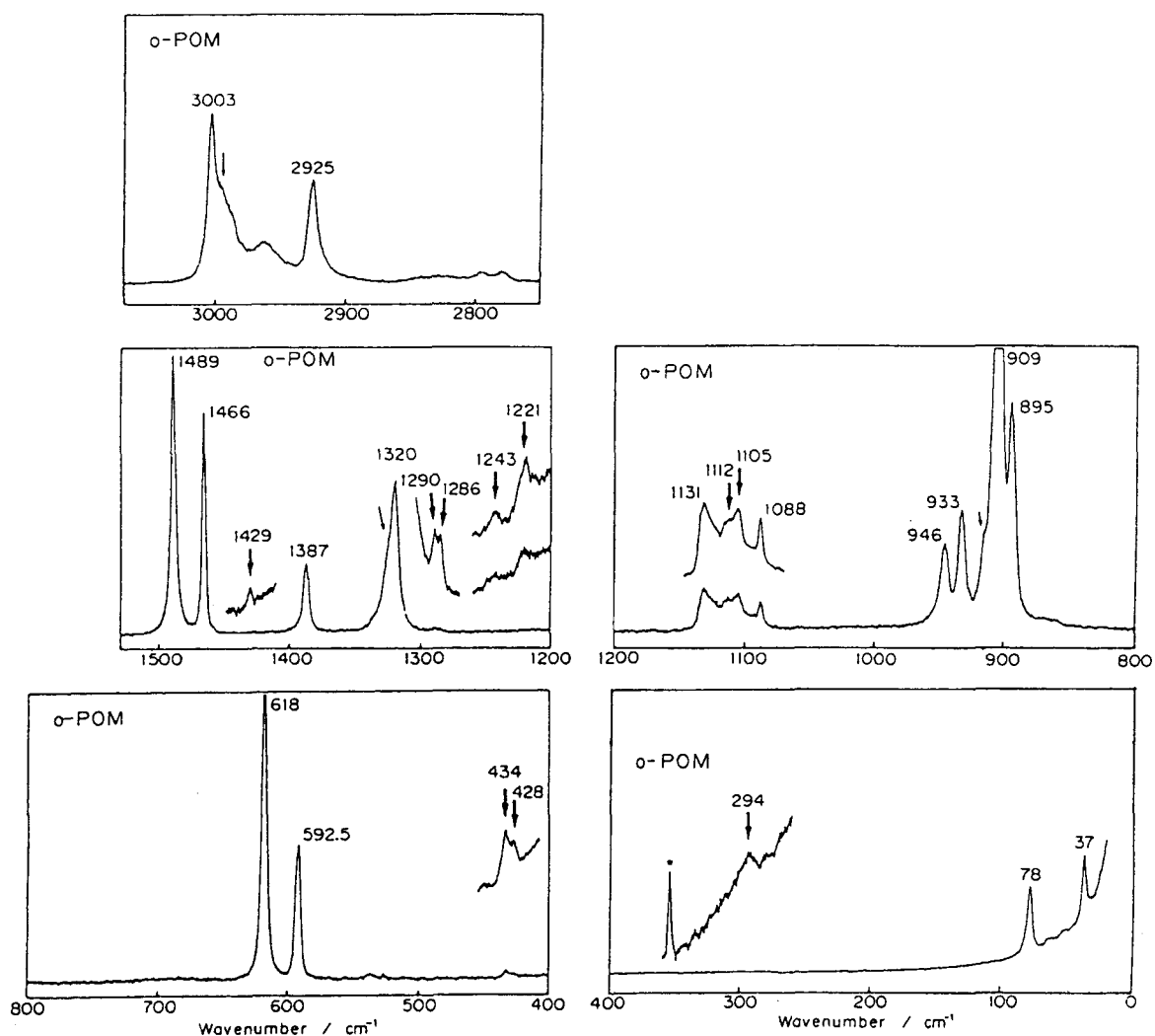
Fig. 2.9. Raman spectra taken on a Sample II at room temperature. The bands marked with fat arrows are newly detected bands. The line with asterisks are due to the natural emission from the Ar⁺ laser.
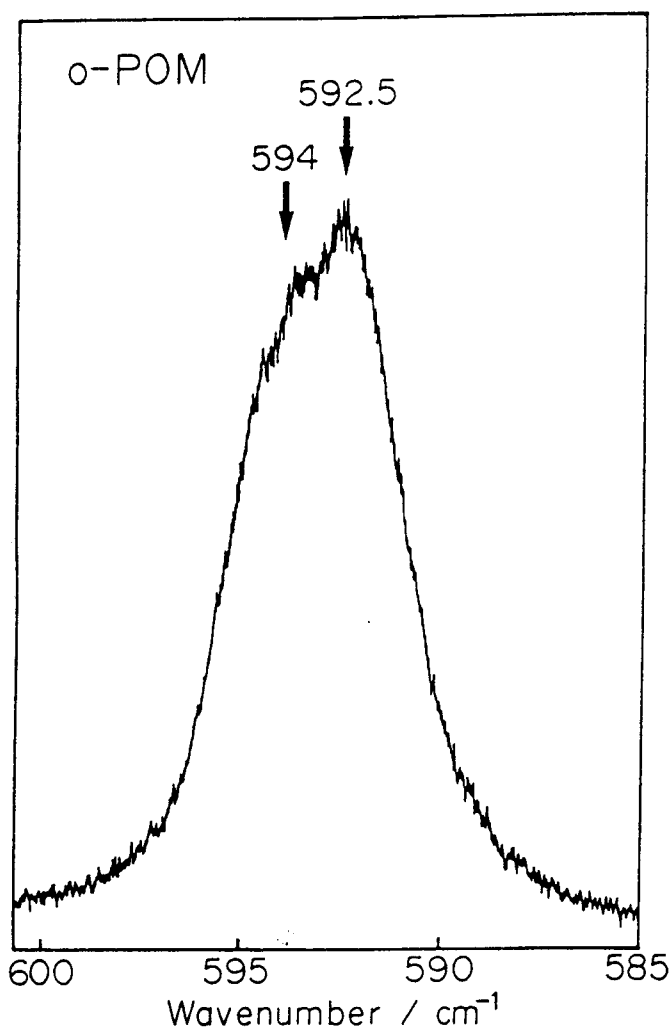
Fig. 2.10. Raman spectra in the B_2-B_3(9) region of o-POM taken on one of the o-POM particle sample.
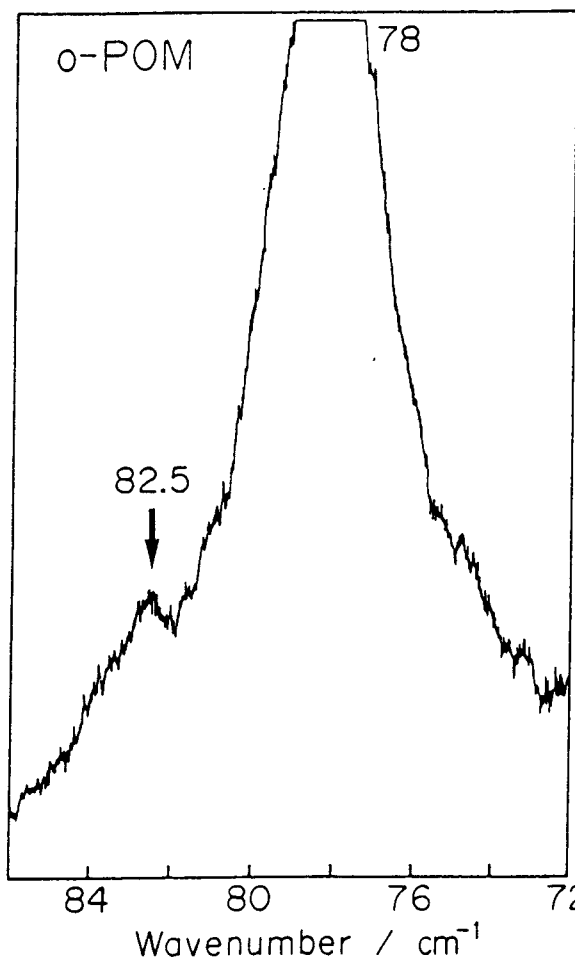
Fig. 2.11. Raman spectra in the $B_3(T_b')$-$B_2(T_a')$ region of o-POM taken on one of the o-POM particle sample.
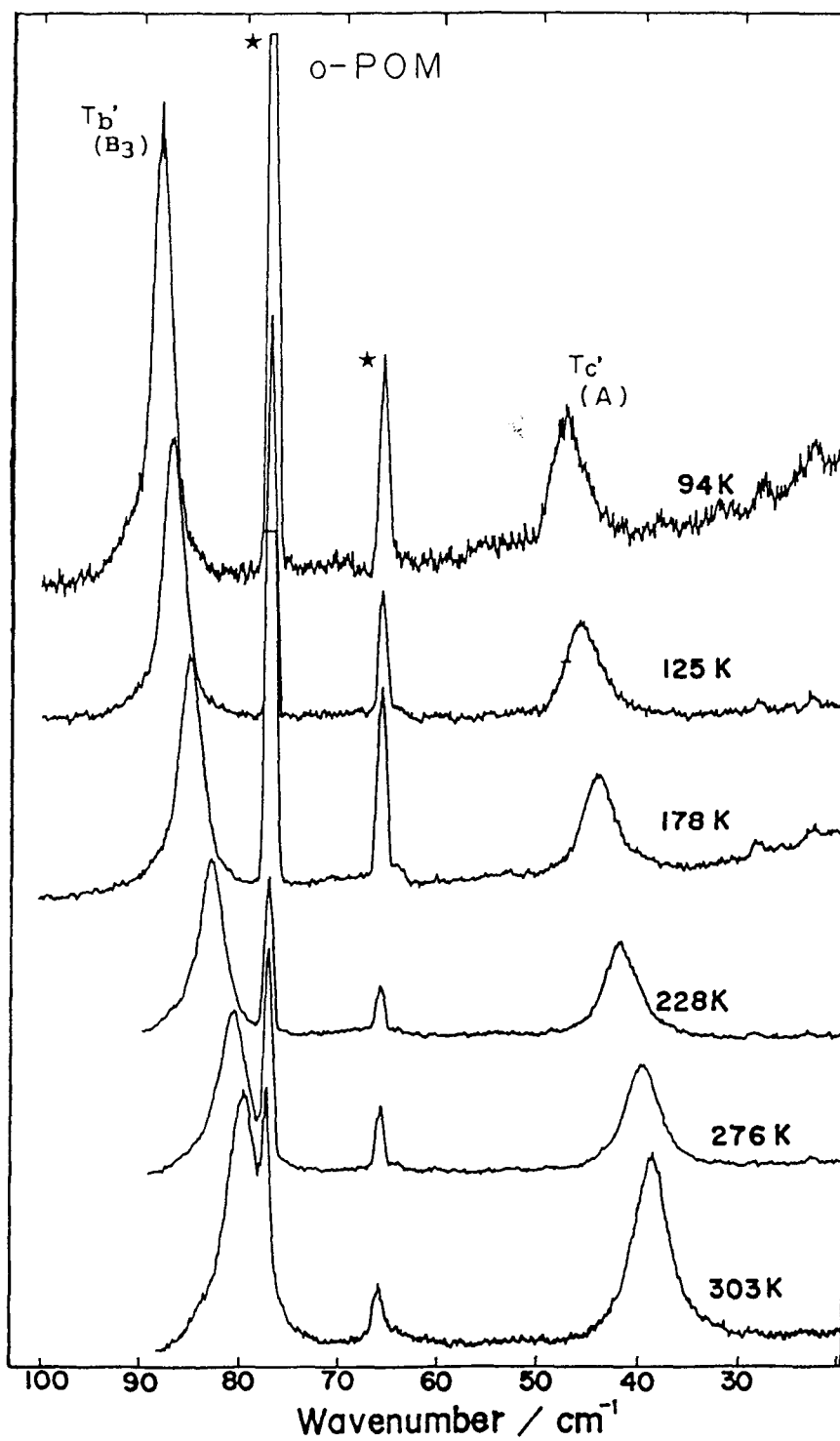
Fig. 2.12. Raman spectra of o-POM in the low-frequency region taken on a powder sample at various temperatures. The bands with asterisks are due to the natural emission from the Ar$^+$ laser.
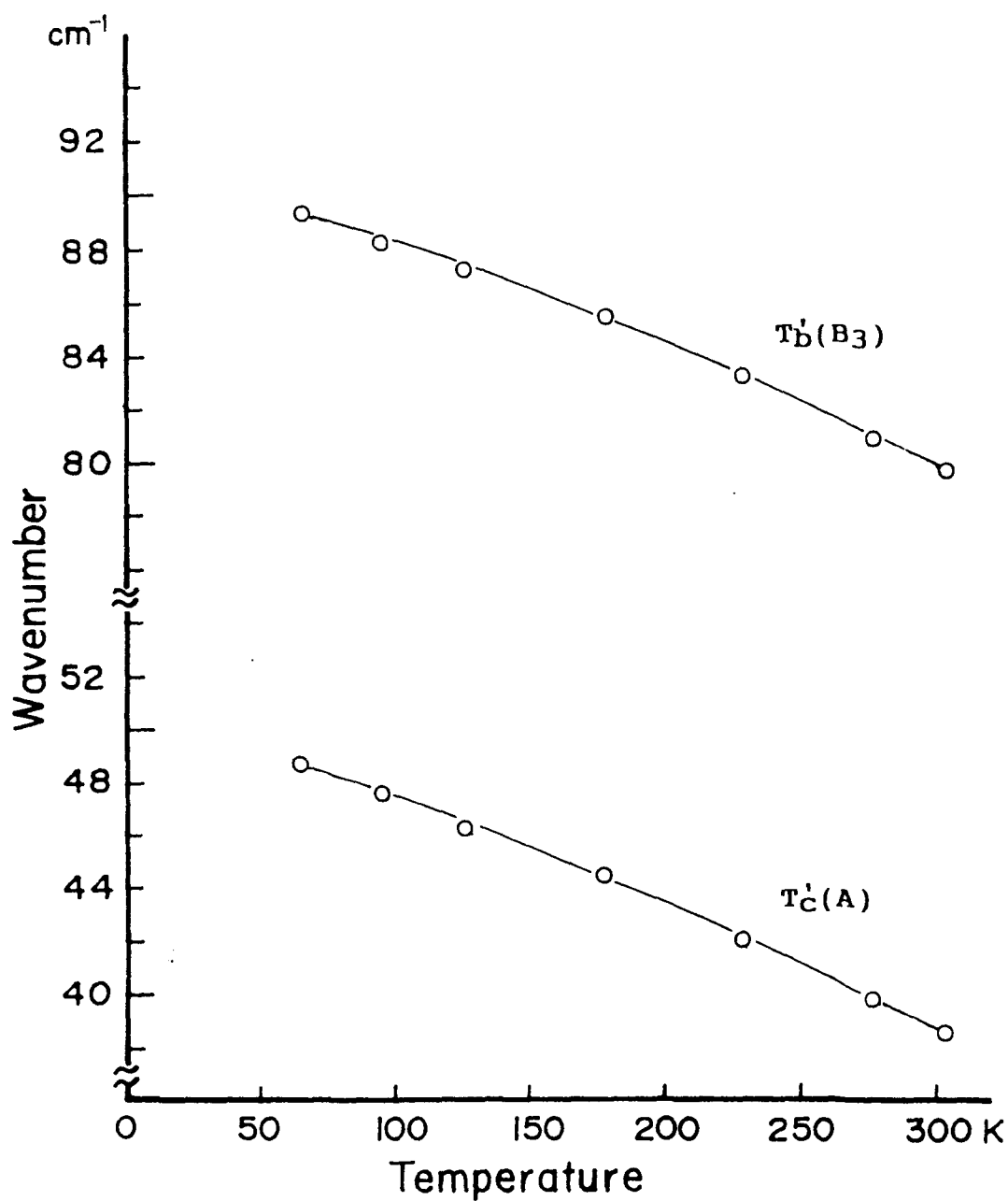
Fig. 2.13. Temperature dependence of $T_b'(B_3)$ and $T_c'(A)$ modes.

the symmetric OCO stretch mode $\nu_s(OCO)$ belonging to the totally symmetric A species by the analogy to the case of t-POM. The Raman tensor of this particular mode has an extremely large α'_{cc} component compared with the other components. Therefore, the X direction should be parallel to the c axis. Consequently every sharp band in the (XX) [i.e., (cc)] spectrum (at 1476, 1323, 909, 622 and 38 cm^{-1}) is assignable undoubtedly to the A species (see Table 2.2). The (cc) spectrum of the rod-like o-POM crystal is compared with the (XX) spectrum of the moth-shaped crystal in Fig. 2.16, these spectra are very close to each other, indicating that X direction of moth-shaped single crystal is parallel to c.

The 1490 cm^{-1} band observed, which was assigned to A(3) mode by previous authors,[8] does not appear in the (XX), but in the (YX), and should be assigned to the B_2 or B_3 species. As for the lattice modes (see 2.4.1.2), the 38 cm^{-1} band appearing in the (XX) is undoubtedly assigned to the A species, and the 80 cm^{-1} band in the (YX) is assigned to the B_2 or B_3 species.

2.4.3. Polarization Scrambling in the Raman Microprobe

The doublets around 1110 and 950 cm^{-1} in the (YX) spectrum should be assigned to the B_2-B_3 split pairs of the 7th and 8th perpendicular molecular modes, respectively. Fig. 2.17 shows the (YX) micro-Raman spectra in the region 1180-880 cm^{-1} of a moth-shaped o-POM single-crystal taken with various objectives with different magnification (x100, x50, x20). In ordinary Raman spectrum taken on a powder sample (see Fig. 2.8), the split components of both pairs are similar in intensity. On the contrary, in the micro-Raman spectra, the low-frequency components are much weaker than the high-frequency ones, and
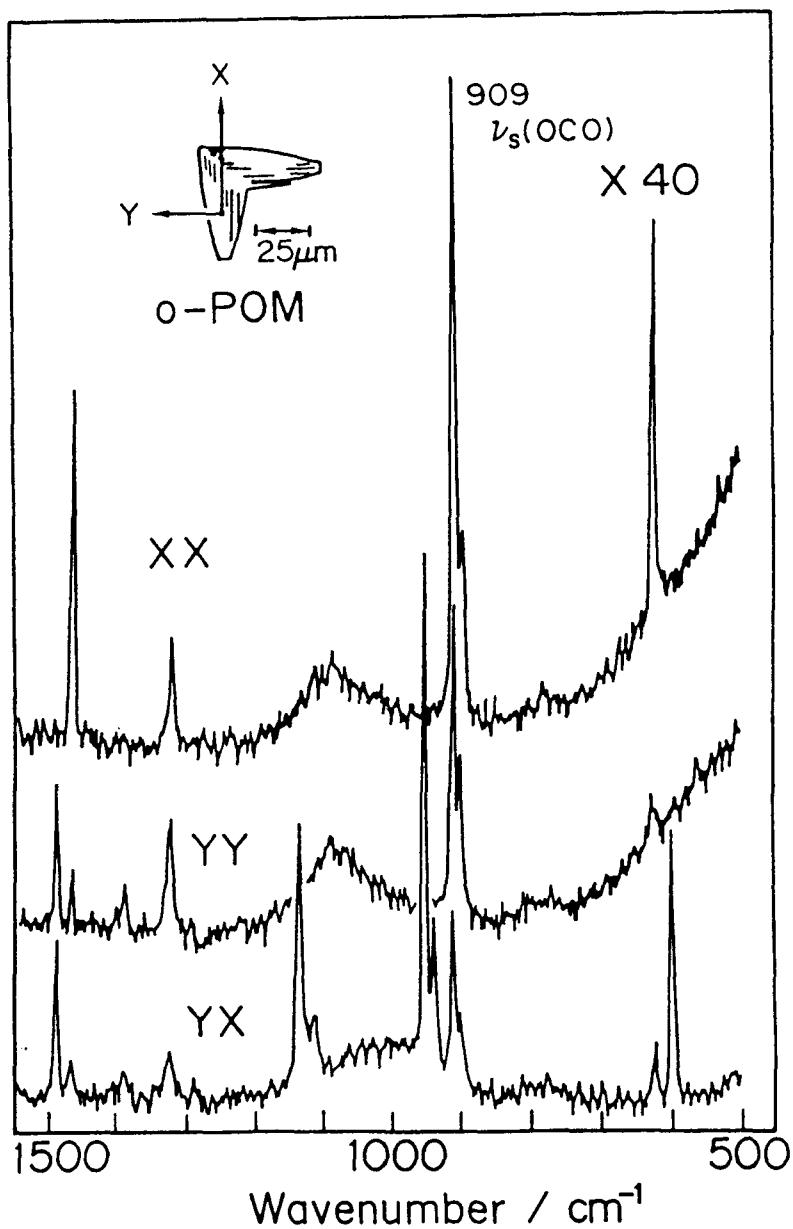
Fig. 2.14. Polarized microfocus Raman spectra of o-POM taken on a moth-shaped single-crystal using an objective lens with x40 magnification.
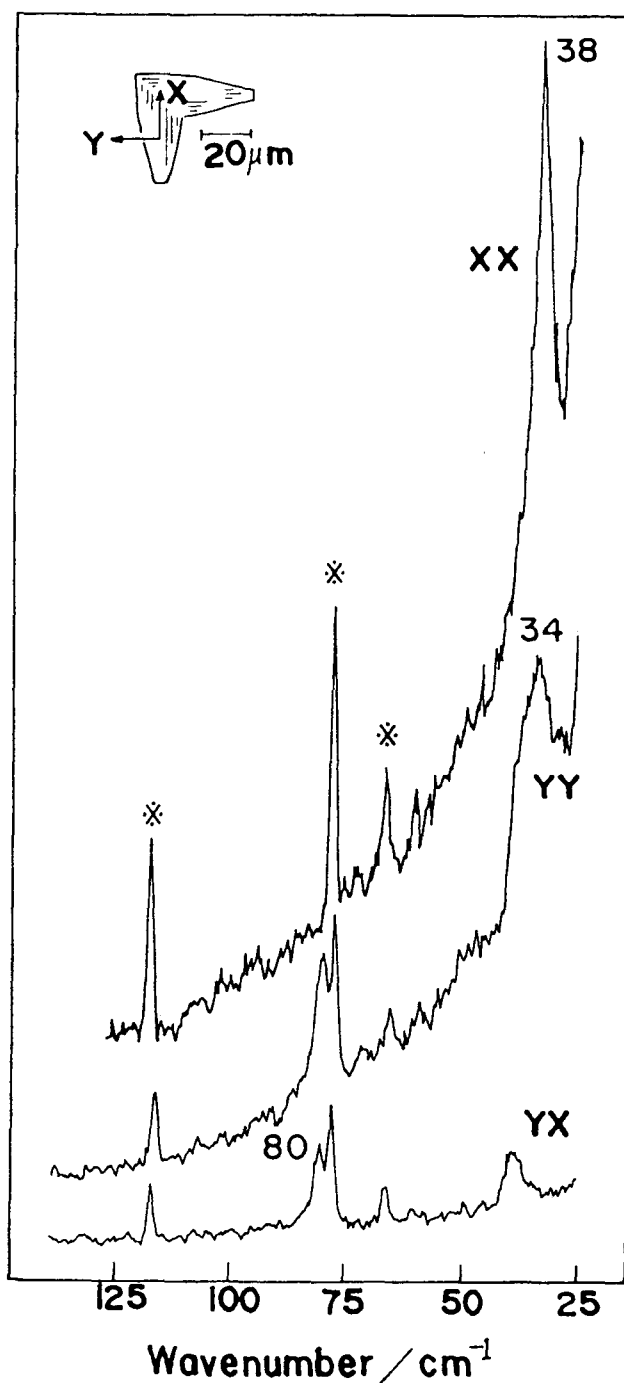
Fig. 2.15. Polarized microfocus Raman spectra of o-POM in the low-frequency region taken on a moth-shaped single-crystal using an objective lens x100. The lines marked with asterisks are due to the natural emission from the Ar^+ laser.
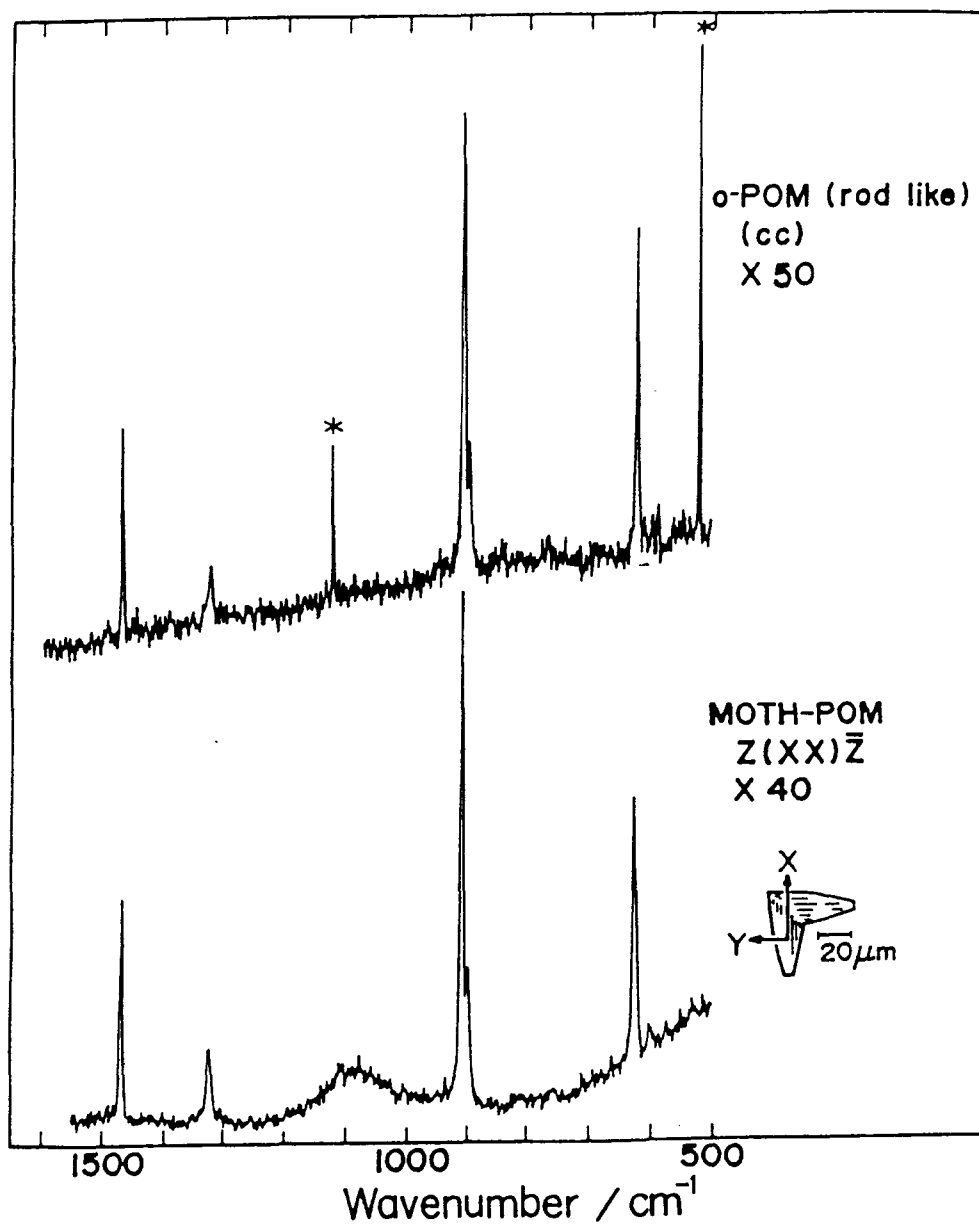
Fig. 2.16. Polarized microfocus Raman spectra of rod-like and moth-shaped single-crystals of o-POM. Line marked with asterisks are due to the natural emissions from the Ar$^+$ laser.
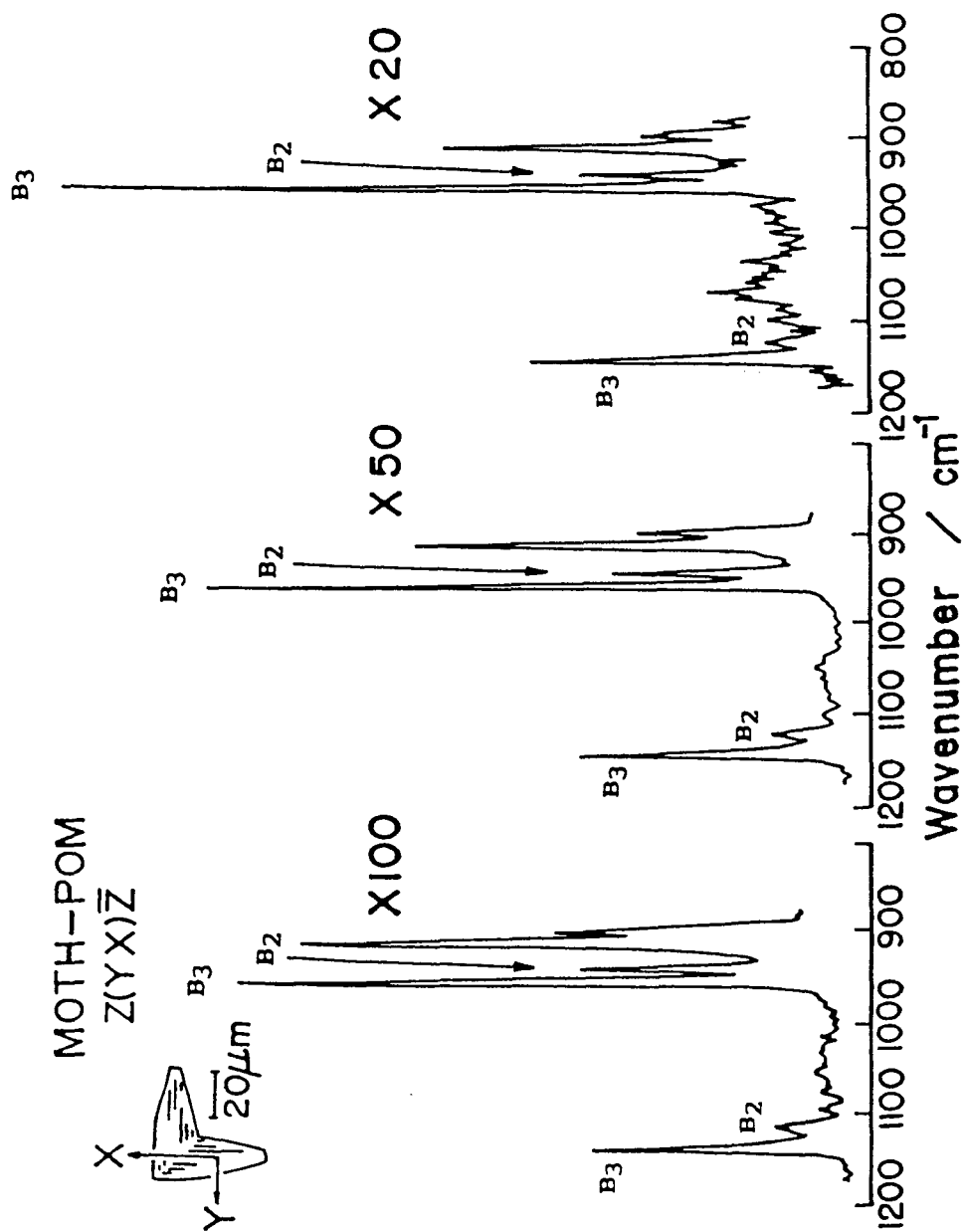
Fig. 2.17. Dependence of the intensity ratios of the B₂-B₃ Davydov split pairs on the magnification of the objective lens.

decrease in intensity with lowering magnification of the objective. Moreover, the (YX) micro-Raman spectra shown in Fig. 2.18 were taken using the x100 objective with (bottom) and without (upper) insertion of aperture II (see Fig. 2.2). The low-frequency components (marked with arrows) of the B_2-B_3 pairs as well as the A(8) band tended to disappear by the insertion of the aperture. The spectral changes indicate that the appearance of the low-frequency components and the A(8) band in the (YX) spectrum originates from the polarization scrambling caused by high-magnification objective (see 2.2.3), and that the crystallographic a (or b) is parallel to the Y, but not inclined to the Y.

As illustrated in Fig. 2.19, the electric vector component polarized parallel to the depth direction (h) in both the incident and scattered lights passing through the peripheral area of the objective is mixed into the perpendicular components, in particular when a high-magnification objective is used (b). The extent of the scrambling can be controlled by changing magnification (or the N.A. value), of the objective or by insertion of the aperture. The latter method has an advantage that we are able to measure the same focussing point in the sample with different optical conditions. We can use these polarization scrambling technique for the vibrational assignments of the Raman-active modes of o-POM.

2.4.4. Infrared Spectra of o-POM Single Crystals

Two B_2-B_3 split pairs (marked with arrows) are observed at 1237-1219 and 439-433 cm^{-1} in unpolarized transmission spectra taken on plane-oriented moth-shaped single crystals (upper of
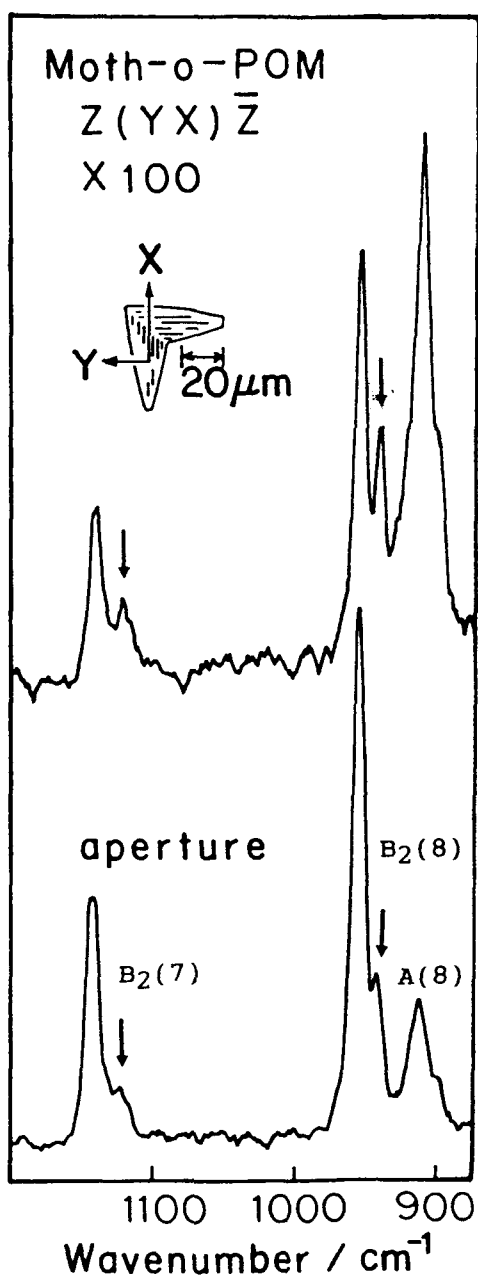
Fig. 2.18. Dependence of the intensity ratios of the B_2-B_3 Davydov split pairs by the insertion of an aperture for moth-shaped single-crystal of o-POM using an objective lens with x100 magnification: (upper) without an aperture, (lower) with an aperture.
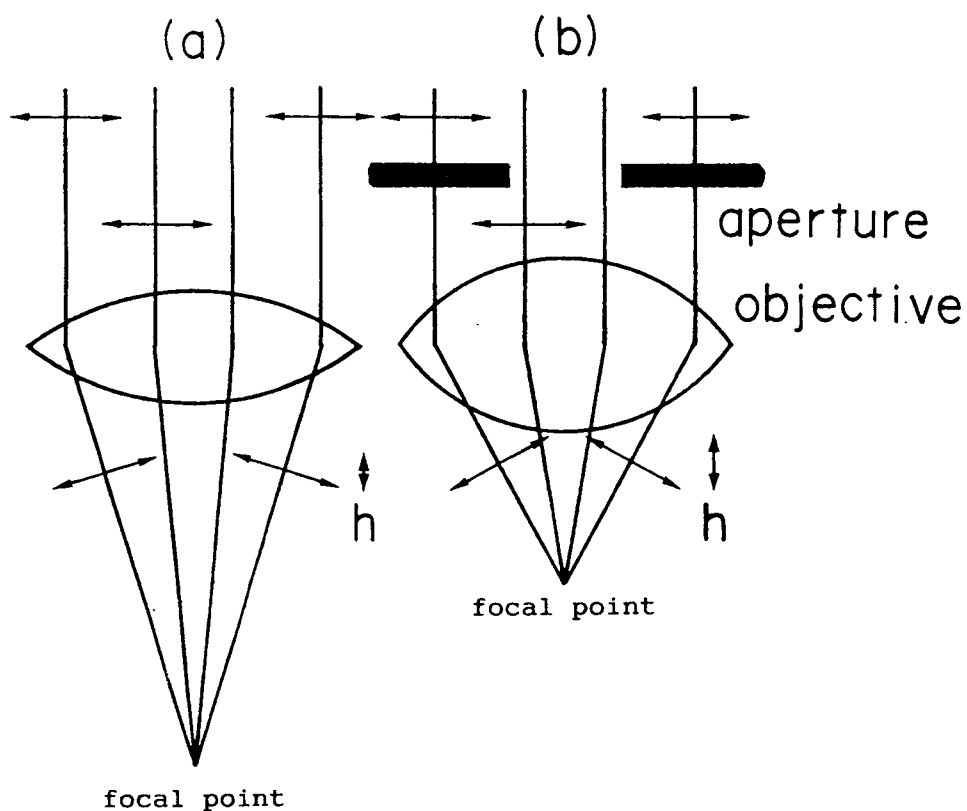
Fig. 2.19. Polarization scrambling by an objective. The double directions arrow of the h shows the quantity of the polarization components. (a) in the case of a low-magnification. (b) insertion of an aperture in the case of the high-magnification, the h components on the peripheral area of the objective are cut off by the aperture.

Fig. 2.20) and powder sample (Sample II) (bottom). Relative intensity of the components in one split pair for the two samples is different from each other; the 1219 and 439 cm^{-1} bands in the plane-oriented sample get stronger than those in the powder sample, indicating that the transition dipole of these components is parallel to the plate face of the moth-shaped single crystal. The reverse is the case for the other components at 1237 and 433 cm^{-1}, indicating that their transition dipole is normal to the plate face. Thus, the infrared polarization of these bands are determined as follows: 1237 cm^{-1} band is (μ_Z), 1219 (μ_Y), 439 (μ_Y) and 433 (μ_Z),

2.4.5. Polarized Micro FT-Infrared Spectra of the Moth-shaped o-POM Single-Crystal

Quite recently, the crystal structure of deca(oxymethylene) diacetate was determined by X-ray diffraction.[23] In order to confirm vibrational assignments of o-POM, polarized Raman and infrared spectra of this single crystal have been measured and analyzed in comparison with those of o-POM single crystal.[24] On the basis of the orientation of the o-POM sublattice in this crystal, polarizations and symmetry species of the infrared and Raman bands due to the zone-center modes of the o-POM lattice were decided. With these results the orientation of the crystal axes of the moth-shaped single crystal has been decided as follows; the X and Y directions are parallel to the c and b axes, respectively.

Polarized infrared spectra of one single crystal of o-POM were tried to measure by using recently developed micro-focus FT-IR spectrometer. The measuring area of 40 x 25 μm^2 on a moth-
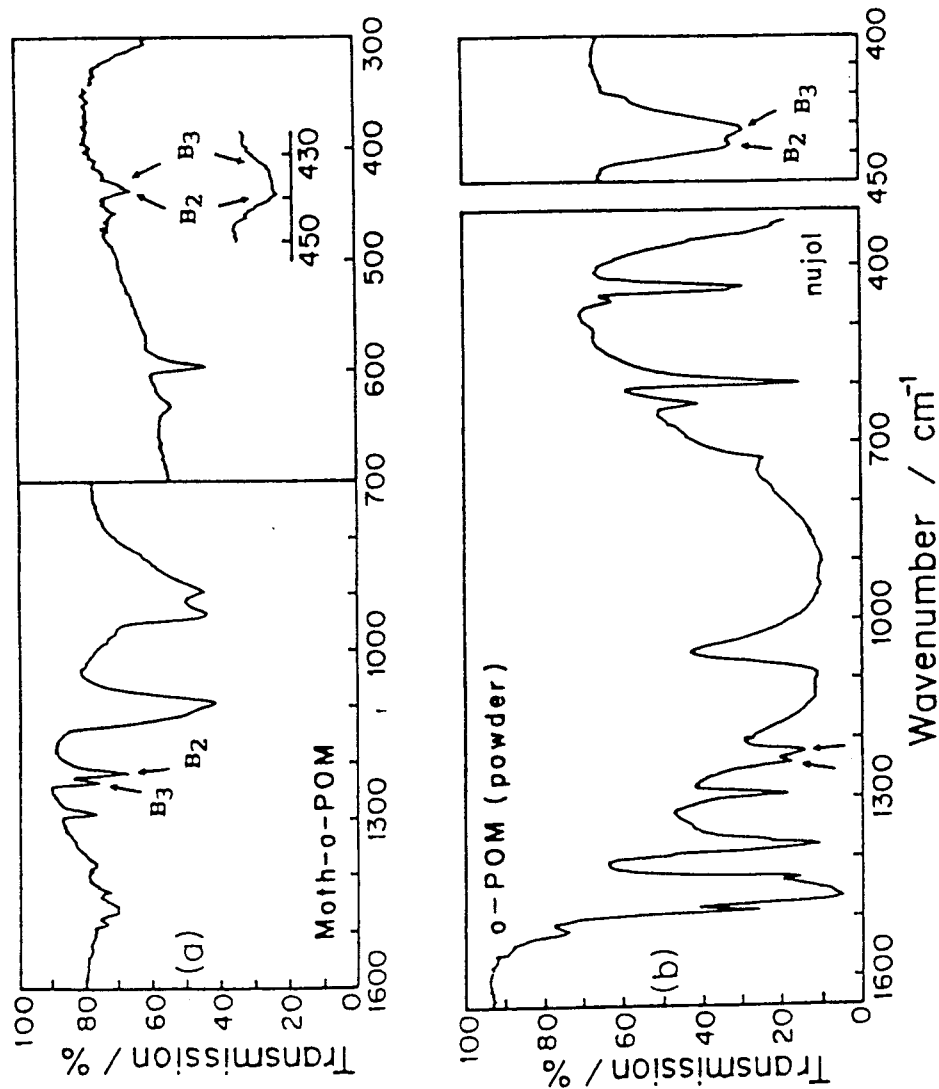
Fig. 2.20 Infrared spectra of o-POM.
Upper: plane-oriented sample consisting of moth-shaped single
crystals
Lower: unoriented sample consisting of o-POM particles.

shaped single crystal (Sample I) was selected by controlling the
aperture size (Fig. 2.21), and polarized micro-focus FT-IR was
measured (Fig. 2.22). The polarized spectra were obtained with
the electric vector perpendicular (the Y//b direction) and
parallel (the X//c direction) to the striations. The sharp bands
in the b-polarized spectrum are assigned to the B_2 modes, whereas
the B_3 bands were almost vanish. As for the split pair of $B_2(6)$-
$B_3(6)$, in the b spectrum, the 1222 cm^{-1} $B_2(6)$ band (marked with
bold arrow) exhibits a strong absorption, while the 1240 cm^{-1}
$B_3(6)$ band (marked with small arrow) is very weak. In the
spectrum of powder sample (Sample II), they appear with almost the
same intensity (see Fig. 2.20). The B_1 modes having μ_c dipole
moment ought to appear in the X parallel spectrum; the 2969 and
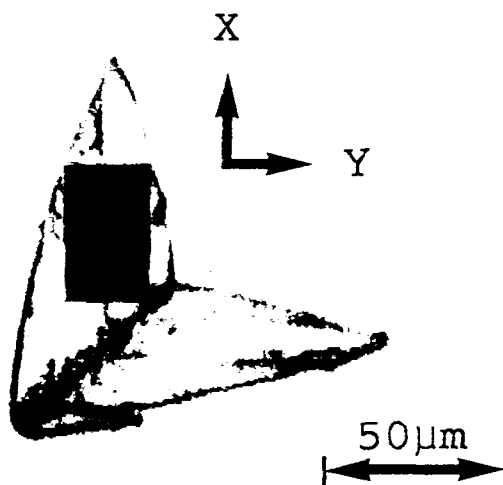
Fig. 2.21. Measuring area and geometry of moth-shaped o-POM
single-crystal for the micro-infrared spectrometry.
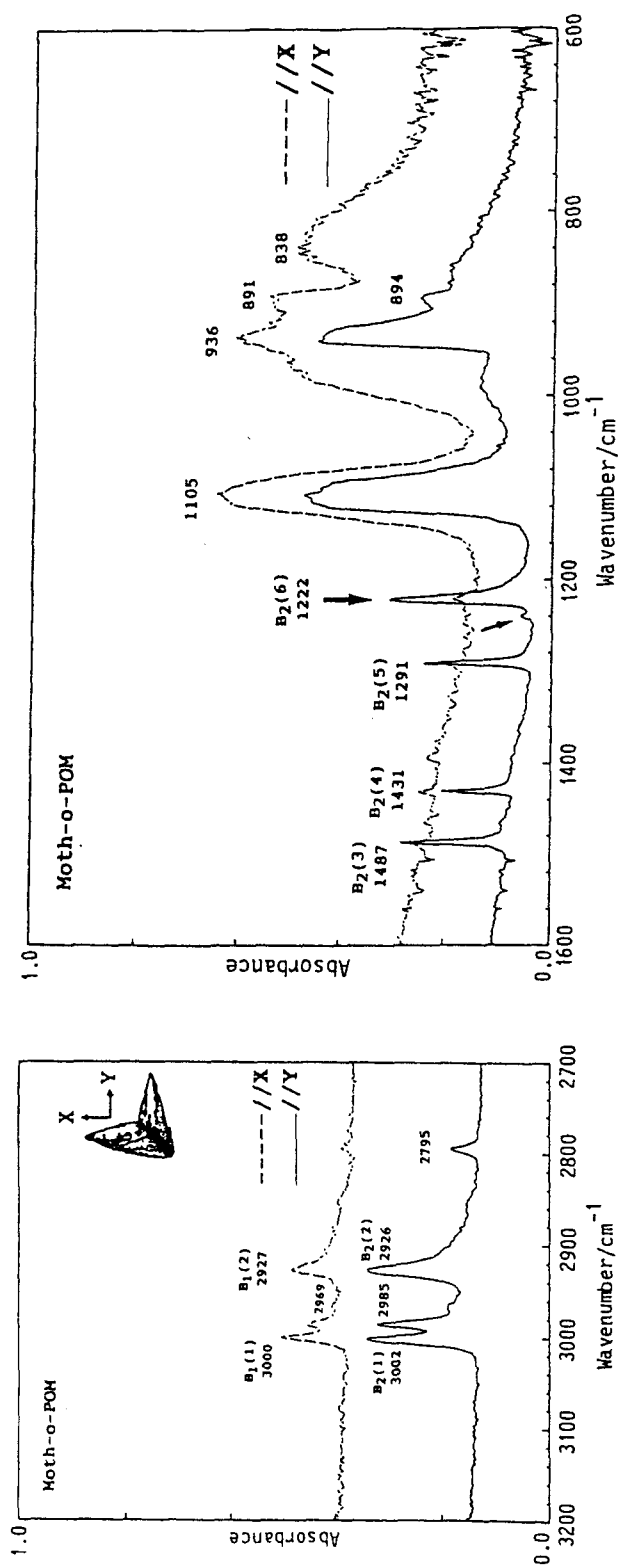
Fig. 2.22. Polarized microfocus infrared spectra of moth-shaped single crystal of o-POM. Bands marked with an arrow are assigned to $B_2(6)$(fat arrow) and $B_3(6)$

2927 cm^{-1} bands are assigned to the $B_1(1)$ and $B_1(2)$, respectively. In the 1150-800 cm^{-1} region strong absorptions are observed. However, the spectra are disturbed remarkably by some sources due to optical situation of the sample. Scattering of the infrared light at the rough surface of the crystal may be one of the origins. We have faced to similar phenomenon for samples having very strong absorptions like POM.

In Table 2.4, the final vibrational assignments of o-POM, determined through various kinds of IR and Raman data obtained for various o-POM samples, are summarized.

2.4.6. Normal Mode Analysis of o-POM Crystal

The normal mode analysis of o-POM was first carried out by Zerbi and Hendra[8] for single chain, and subsequently by Boerio and Cornell for a full model of the crystal of orthorhombic system.[9] Boerio and Cornell[9] mentioned the lattice modes and the dispersion relations, but did not report the details of the molecular modes. A part of the calculated results in ref. 8 is in consistent with our polarization data, as mentioned in the preceding section, but the number of the frequency data used is too small to compare with the theoretically expected number of the zone-center modes. Therefore, we re-calculated the normal frequencies of the optically active modes, including the lattice vibrations, of the o-POM crystal using a complete model. The molecular geometry in the lattice was transferred from ref. 5. The intramolecular force constants of a modified VFF type were transferred first from those of t-POM[25] and trioxane[26,27] and then adjusted by a least-squares method so as to reproduce the measured frequencies. The values of the final set are listed in

Table 2.4. Vibrational spectra of crystalline o-POM

	Frequencies (cm^{-1})				
	Observed				Calculated
Species	Raman		IR		
	Particle sample	Moth-shaped single crystal	powder[a]	Moth-shaped crystal	
A (1)	3003 s[b]	3010 m XX,YY,YX↓[d]			3000
B$_3$(1)	~2980 m	2990 m XX,YX[c]	3000 s[b]		3008
B$_2$(1)			2980 s	3002 ⊥[c]	3007
B$_1$(1)			2965 m	3000 //	3001
A+B$_1$(2)	2925 s	2930 m XX,YY,XY↓[d]			2899
			2920 s	2927 //	2898
B$_2$(2)				2926 ⊥	2899
B$_3$(2)					2898
B$_2$+B$_3$(3)	1489 s	1490 m YY↓,YX	1488 m	1487 ⊥	1470
					1481
A (3)	1466 s	1476 s XX,YY,YX↓			1476
B$_1$(3)			1466 m		1487
B$_2$+B$_3$(4)	1429 vw		1430 m	1431 ⊥	1397
					1399
B$_1$(4)	1393 vw		1392 m		1410
A (4)	1387 m	1387 w YY,YX↓			1410
B$_1$(5)	1328 vw				1323
A (5)	1320 s	1323 m XX,YY,YX↓			1320
B$_3$(5)	1286 vw				1266
B$_2$(5)	1290 vw		1290 m	1291 ⊥	1267
B$_3$(6)	1243 vw		1237 m	(1237μ$_Z$)[e]	1217
B$_2$(6)	1221 vw		1220 s	1222 ⊥	1212
B$_3$(7)	1131 vw	1135 s YX	1120 sh		1107
B$_2$(7)	1112 vw	1110 vw YX↓ (XX)	1110 s		1110
A (6)	1105 vw				1152
B$_1$(6)	1088 vw		1092 s	(1092)[e]	1151
B$_3$(8)	946 w	950 s YX			937
B$_2$(8)	933 w	937 w YX↓ (XX)	937 vs	(938)[e]	934
A (7)	922 vw				939
B$_1$(7)	915 vw				935
A (8)	909 vs	909 vs XX,YY,YX↓			911
B$_1$(8)	895 m	898 m XX,YY,YX↓	895 vs	(895)[e]	913
B$_1$(9)			636 vw		640
A (9)	618 m	622 s XX,YY,YX↓			631
B$_3$(9)	592.5 m				595

(Continue)

$B_2(9)$	594 w	596 m	YX,YY↓	594 s	(594)[e]	594
$B_2(10)$	434 vw			434 s	(439 ⊥)[e]	444
$B_3(10)$	428 vw			428 s	(433μ_Z)[e]	441
$A+B_1(10)$	294 vw					305
				304 m		301
$B_1(R_c')$				130 m		95
$B_2(T_a')$	82.5 vw			89 w		96
$B_3(T_b')$	78 s	80 w		83 w		87
$A (R_c')$						85
$A (T_c')$	37 m	38 s	XX			43

[a] Refer to ref. 7.
[b] Relative intensity, vs;very strong, s;strong, m;medium, vw;very weak, w;weak, sh;shoulder.
[c] polarization
[d] ↓; indicate a decrease of Raman intensities in the polarization by insertion of an aperture.
[e] data for the Moth-shaped single crystals data

Table 2.5. The intermolecular force constants were derived from the interatomic potential functions of the form

$$V_{jk}(r_{jk}) = Ar_{jk}^{-6} + B\, exp(-Cr_{jk}) + Dr_{jk}^{-12}$$

where r_{jk} denotes the distance between nonbonded atoms j and k. The values of the four parameters A, B, C, and D for the various atomic pairs are listed in Table 2.6. The values for the H···H, H···C, and C···C pairs were those used in the calculation of the polyethylene crystals[28,29] and those for the H···O, C···O and O···O pairs were transferred from ref. 30. The first and second derivatives of V_{jk} with respect to r_{jk}

$$f'_{jk} = (\partial V_{jk}/\partial r_{jk})_0 / r_{jk}^0$$

and

$$f''_{jk} = (\partial^2 V_{jk}/\partial r_{jk}^2)_0$$

were used as the force constants for the $j-k$ atom pairs.[29] The calculated frequencies are given in Table 2.4. The calculated values themselves agree well (with the deviations less than 3%) with the observed one, except for the $B_1(6)$ and $B_1(R_c')$ modes. However, for the B_2-B_3 Davydov splitting mentioned in the preceding section, the calculated band gaps are very small (0-3 cm^{-1}) compared with those observed (up to ~25 cm^{-1}). This discrepancy may originate from disregard of electrostatic interactions which probably play important roles in the system of polar molecules such as POM. Nevertheless, present result is a

Table 2.5. Intramolecular force constants for o-POM

No.	Force constant	Coordinates involved	Common atoms	Values
1	K_r	C—H		4.7142
2	K_D	C—O		6.1122
3	H_γ	∠HCO		0.6513
4	H_δ	∠HCH		0.7341
5	H_ω	∠OCO		1.4319
6	H_ω'	∠COC		1.5120
7	T	Torsion		0.1159
8	F_r	C—H, C—H	C	−0.0460
9	F_D	C—O, C—O	C	0.1010
10	F_D'	C—O, C—O	O	−0.0261
11	F_{Dr}	C—H, C—O	C	0
12	$F_{r\gamma}$	C—H, ∠HCO	C, H	0
13	$F_{r\delta}$	C—H, ∠HCH	C, H	0
14	$F_{D\gamma}$	C—O, ∠HCO	C, O	0.4055
15	$F_{D\gamma}'$	C—O, ∠HCO	C	0.0140
16	$F_{D\omega}$	C—O, ∠OCO	C, O	0.6697
17	$F_{D\omega}'$	C—O, ∠COC	C, O	−0.1545
18	F_γ	∠HCO, ∠HCO	C, O	−0.0050
19	F_γ'	∠HCO, ∠HCO	C, H	0.0120
20	$F_{\gamma\gamma}'$	∠HCO, ∠HCO	C	−0.0604
21	$F_{\gamma\delta}$	∠HCO, ∠HCH	C, H	0.0939
22	$F_{\gamma\omega}$	∠HCO, ∠OCO	C, O	0.0602
23	$f_{\gamma\omega'}^{g}$	∠HCO, ∠COC	C, O	0.0040
24	$f_{\gamma\omega'}^{t}$	∠HCO, ∠COC	C, O	−0.1120
25	$f_{\gamma\omega'}^{'g}$	∠HCO, ∠COC	C	−0.1035
26	$f_{\gamma\omega'}^{'t}$	∠HCO, ∠COC	C	0.0827
27	$f_{\omega\omega'}^{g}$	∠COC, ∠OCO	C, O	0.0110
28	h_γ^{e}	∠HCO, ∠HCO	O	0
29	h_γ^{a}	∠HCO, ∠HCO	O	0
30	h_γ^{ae}	∠HCO, ∠HCO	O	0

Stretch constants have unit of mdyn A^{-1}, the stretch—bend interactions have unit of mdyn rad^{-1} and the bending constants have unit of mdyn A rad^{-2}.

Table 2.6. Intermolecular potential parameters for o-POM

Atomic pair	A (kJ nm^6 mol^{-1})	B (kJ mol^{-1})	C (nm^{-1})	D (kJ nm^{12} mol^{-1})
H···H	7.16×10^{-5}	4.60×10^{3}	35.6	0
C···H	5.23×10^{-4}	4.00×10^{4}	36.7	0
C···C	2.38×10^{-3}	3.50×10^{5}	36.0	0
O···H	5.19×10^{-4}	0	0	1.05×10^{-7}
O···C	1.54×10^{-3}	0	0	5.00×10^{-7}
O···O	1.54×10^{-3}	0	0	6.00×10^{-7}

convincing criterion for determining the assigning of the split components. For the $B_2(8)$-$B_3(8)$ Davydov split pair around 945 cm^{-1} the calculated result suggests that the B_3 species with α_{bc} Raman tensor element appear at the high-frequency side, so the b axis is parallel to the Y direction. This is also consistent with the appearance of the observed 6th, 10th, and T_a'-T_b' (Transitional lattice modes) B_2-B_3 Davydov split pairs, although on the 7th B_2-B_3 split pair around 1120 cm^{-1} the reverse conclusion is derived. In the table 2.4 and Figs. 2.8 and 2.9, the assignment based on this calculated result was adopted. Thus, we could conclude that the crystallographic a, b and c axes of the moth-shaped o-POM single crystal were located parallel to Z, Y and X, respectively.

REFERENCES

1 H. Tadokoro, T. Yasumoto, S. Murahashi and I. Nitta, J. Polym. Sci., **44**, 266 (1960)

2 T. Uchida and H. Tadokoro, J. Polym. Sci., **Part A-2**, 5, 63 (1967)

3 G. Carazzolo, J. Polym. Sci., **Part A**, 1, 1573 (1963)

4 L. Mortillario, G. Galliazzo and S. Bessi, Chem. Ind. (Milan), **46**, 139, 144 (1964)

5 G. Carazzolo and M. Mammi, J. Polym. Sci., **Part A**, 1, 965 (1963)

6 V. Zamboni and G. Zerbi, J. Polym. Sci., **Part C**, 7, 153 (1966)

7 G. Zerbi and G. Masetti, J. Mol. Spectros., **22**, 284 (1967)

8 G. Zerbi and P. J. Hendra, J. Mol. Spectros., **27**, 17 (1968)

9   F. J. Boerio and D. D. Cornell, J. Chem. Phys., 56, 1516
    (1972)

10 M. Kobayashi, H. Morishita, M. Shimomura and M. Iguchi,
    Macromolecules, 20, 2453 (1987)

11 H. Morishita, M. Kobayashi, M. Shimomura, M. Iguchi and
    H. Kuwahara, Sci. Bull. Fac. Educ., Nagasaki Univ., 41, 1
    (1989)

12 M. Iguchi, H. Kanetsuna and T. Kawai, Makromol. Chem., 128,
    63 (1969)

13 M. Iguchi, Brit. Polym. J., 5, 195 (1973)

14 M. Iguchi and I. Murase, J. Crystal Growth, 24/25, 596 (1974)

15 M. Iguchi, I. Murase and K. Watanabe, Brit. Polym. J., 6, 61
    (1974)

16 M. Iguchi, Polymer, 24, 915 (1983)

17 M. Kobayashi, Y. Itoh, H. Tadokoro, M. Shimomura and
    M. Iguchi, Polym. Commun., 24, 38 (1983)

18 M. Kobayashi, H. Morishita, T. Ishioka, M. Iguchi,
    M. Shimomura and T. Ikeda, J. Mol. Struct., 146, 155 (1986)

19 H. Morishita, M. Kobayashi, M. Shimomura and M. Iguchi, Sci.
    Bull. Fac. Educ. Nagasaki Univ., 39, 47 (1988)

20 H. Morishita and M. Kobayashi, Rep. Prog. Polym. Phy, Jpn.,
    30, 139 (1987)

21 H. Sugeta and T. Miyazawa, J. Chem. Phys., 47, 2034 (1967)

22 H. Sugeta, Doctoral Thesis, Osaka University, 1969

23 T. Takahashi, N. Miyatake, K. Ute and K. Hatada, polym.
    preprins, Jpn., 41, 1357 (1992)

24 M. Kobayashi, T. Adachi, Y. Matsumoto, H. Morishita, T.
    Takahashi, K. Ute and K. Hatada, J. Raman Spectrosc.,
    24, 533 (1993)

25 H. Tadokoro, M. Kobayashi, Y. Kawaguchi, A. Kobayashi and
    S. Murahashi, J. Chem. Phys., **38**, 703 (1963)

26 M. Kobayashi, R. Iwamoto and H. Tadokoro, J. Chem. Phys., **44**,
    922 (1966)

27 M. Kobayashi, J. Chem. Phys, **66**, 32 (1977)

28 M. Kobayashi and H. Tadokoro, J. Chem. Phys., **66**, 1258 (1977)

29 M. Kobayashi, J. Chem. Phys., **70**, 4797 (1979)

30 T. Ooi, R. A. Scott, G. Vanderkooi and H. A. Scheraga, J.
    Chem. Phys., **46**, 4410 (1967)

Chapter 3.

Vibrational Spectroscopic Study on Trigonal Poly(oxymethylene) Consisting of the Extended Chain Morphology

3.1. Introduction

Trigonal poly(oxymethylene)[1-3] is obtained exclusively through the ordinary crystallization process from the melt or dilute solutions of POM resins. Staudinger et al.[4] obtained hexagon prism-like crystals of β-poly(oxymethylene) from aqueous solution of formaldehyde in the presence of sulfuric acid. They reported that the obtained samples consisted of extended chain molecules. On the contrary, Fischer[5] pointed out that there was no evidence that extended chain crystals were formed through such process. Several studies were done on structural investigations and on syntheses of extended chain crystals of t-POM.[2,6]

Two decades ago, Iguchi et al. obtained feather-shaped[7,8] and needle-like single crystals[9,10] of t-POM consisting of the fully extended chains (ECC). They were generated in a heterogeneous cationic polymerization system of trioxane in cyclohexane solution using boron trifluoride and water as catalyst. The polymerization method for preparing t-POM single crystals of different habits was basically the same.

Typical folded chain crystals (FCC) of t-POM have been obtained as solution-grown single crystals.[11-13] These crystals precipitated from dilute solutions, say from a bromobenzene solution, have a hexagon plate-like shape with a lamellar thickness (corresponds to the stem length of regularly folded

molecules) of about 10 nm. Infrared and Raman spectra of normal and deuterated poly(oxymethylene) (t-POM-d_2) have been investigated by many workers from structural and analytical viewpoints.[14-19] For the normal mode analysis of molecular vibrations and study of molecular orientation, polarized spectral data are of essential importance. Polarized infrared spectra of oriented films of t-POM and t-POM-d_2 have been measured, and vibrational assignments of the zone-center fundamentals have fully been established by the normal mode analysis based on the polarization data.[15]

On the contrary, polarization measurement of Raman spectra of t-POM has been extremely difficult, because drawn fibers of commercially available t-POM samples and superdrawn fibers of t-POM produced by microwave heating method[16] were opaque and therefore polarizations of the incident and scattered lights were strongly scrambled. Thus, all the Raman spectra of t-POM reported so far were of unpolarized. The infrared-inactive and Raman-active E_2 modes were not observed, except for $E_2(4)$, $E_2(7)$ and $E_2(12)$ bands at 1387, 949 and 64 cm^{-1} of t-POM, respectively, and $E_2(12)$ at 58 cm^{-1} of t-POM-d_2.[17-19]

Recently, we found that on heating above 69°C, single crystals of o-POM transformed to the trigonal phase, keeping the original crystal habit and the molecular orientation unaltered as those of the starting o-POM crystals[20,21] (see the next chapter). Thus, we obtained moth-shaped single crystals of t-POM having size and optical clearness suitable for the polarized micro-Raman measurement.[22]

Another method for obtaining well-oriented and highly crystalline transparent samples of t-POM has been developed by

Komatsu et al.[23,24] They succeeded to produce superdrawn
filaments containing little amount of voids by stretching POM
resin under high pressure. With such samples we are able to
measure polarized Raman spectra by the ordinary right-angle
scattering.[25]

Another unsolved problem of t-POM is concerned with the
handedness of the helical molecules in the lattice.
Crystallographically, the most reliable space group of t-POM
lattice is $P3_1$-C_3^2 or $P3_2$-C_3^3 with the unit cell containing one
molecule of right-handed or left-handed helix. Therefore, the
unit cell should be non-centrosymmetric (or chiral). However,
there is still uncertainty in the chirality and the value of
azimuthal angle of the molecule with respect to the *a* axis,
because of difficulty in determining the respective positions of
the C and O atoms caused by the isoelectronic nature of O atom
and CH_2 group. In fact, the precise value of the azimuthal angle
with respect to the *a* axis has not be determined yet.

Absence or presence of the inversion center in the space
group is detectable spectroscopically by observing the phenomenon
of the LO(longitudinal optic)-TO (transverse optic) splitting of
the E_1 Raman bands which belong to the polar (infrared-active)
phonons.

In this chapter, polarized Raman spectra of t-POM were
measured on the various types of highly-oriented sample mentioned
above. Our main interests were focused on (1) to perform
assignment of Raman-active E_2 mode of t-POM and t-POM-d_2 on which
little have been known so far, and (2) to confirm the non-
centrosymmetric unit cell of the t-POM lattice by testing whether
the LO-TO splitting is observed for E_1 bands (Raman-active polar

phonon) or not.

3.2. Experimental

3.2.1. Samples

Needle-like single crystals[26-30] (consisting of polymer whiskers) of t-POM and t-POM-d_2 were supplied from Research Institute for Polymers and Textiles. These crystals were of hexagon-shape with dimensions as large as about 2 μm in diameter and 100 μm in length or less.

Moth-shaped[22] single crystals and particle sample consisting of many rod-like single crystals of t-POM[25] were obtained by the thermally induced solid-state phase transition of o-POM crystals having the same habits[20,21] (cf. Chapter 2). The resultant single crystals showed clearly optical birefringence. As for the scattering geometry of micro-Raman experiment, we defined the sample-fixed Cartesian coordinates for the moth-shaped single crystal as follows; X is parallel to the striations seen on the crystal face, Y perpendicular to it within the plate surface, and Z normal to the plate surface.

Pressurized superdrawn filaments (with the elongation ratio λ = 19) were produced in Asahi Chemical Co. Ltd. We used a rectangular filament with 2 mm width and 0.8 mm thickness for the polarization Raman measurements. The filament was cut into 10 mm length, and the cut surface was polished with fine carborundum until the surface become clear. The sample-fixed Cartesian coordinates of this filament were defined as follows; X is parallel to the elongated direction (the c axis), Y perpendicular to it within the wide surface, and Z normal to the XY plane.

3.2.2. Vibrational Spectral Measurements

Ordinary right-angle Raman spectra of t-POM samples were taken with a JASCO R-500 monochromator using the 514.5 or 488.0 nm (Ar$^+$) excitation laser beam. For the Raman measurement at low temperature, an Oxford continuous flow-type cryostat was used. A powder sample of needle-like single crystals was enclosed in thin-walled glass capillary and mounted on the cold finger of the cryostat with qurtz windows.

For the detection of LO-TO splitting angular dispersion of the LO components of $E_1(7)$ and $E_1(8)$ modes was measured on superdrawn filament with the following geometry. The X axis of the sample was placed parallel to the scattering plane constructed with the incident q_i and scattered photon q_s propagation vectors ($q_i \perp q_s$), and the angle θ between the X axis and the phonon propagation vector $q = q_i - q_s$ was set at 0°, 45°, and 90° by rotating the sample around the Y axis set perpendicularly to the scattering plane. The Y-polarized incident beam was used and the scattered light polarized parallel to q_i was collected [cf. Fig. 3.8 (a)].

Micro-Raman spectra of one t-POM single crystal were taken with a JASCO NR-1000 double monochromator of 100 cm focal length using the 514.5 nm exitation source. Optical system of the micro-Raman instrument is illustrated in Fig. 2.2. Focused laser-spot size depends on the magnification of the objective lens used; 1 μm diameter for x100 magnification.

3.3. Results and Discussion

3.3.1. Polarized Vibrational Spectra of t-POM

The t-POM unit cell belongs to the space group $P3_1$-C_3^2 (or

$P3_2$-C_3^3) and contains one 9/5 helical molecule having the D($10\pi/9$) line group symmetry which is isomorphous to the D_9 point group. The zone-center normal modes of the 9/5 helical molecule of t-POM are classified into six symmetry species. The number of the normal modes and the infrared and Raman polarizations for each symmetry species are summarized in Table 3.1. In the table, c and a denote the crystal axes of the trigonal lattice, and a^* is the axis perpendicular to the ac plane. In what follows, the optically active fundamentals are designated as $A_1(m)$ (m=1-5), $A_2(m)$ (m=1-5), $E_1(m)$ (m=1-11), and $E_2(m)$ (m=1-12), the numbering m being mode in the order of higher to lower frequency.

Fig. 3.1 shows polarized micro-Raman spectra of a moth-shaped t-POM single crystal. All the sharp bands appearing in the (XX) spectrum are assigned to the A_1 species on reference to the previous results of t-POM.[15] Especially, the strongest 921 cm^{-1} band is assigned to the $A_1(4)$, the OCO symmetric stretch ν_s(OCO), which has large α_{cc} Raman tensor element compared with those of the other vibrational modes. This shows that the X direction is parallel to the crystallographic c axis.[21]

The bands appearing in the (YX) [i.e., the (ac) and (a^*c)] spectrum should be assigned to the E_1 modes; the bands around 1100, 940 and 640 cm^{-1} are assigned to $E_1(7)$, $E_1(8)$ and $E_1(9)$, respectively. E_2 modes including α_{aa}, α_{a^*a} and $\alpha_{a^*a^*}$ elements (see Table 3.1) are expected to appear in (YY) spectrum, but not in (XX) and (YX). The 1387 cm^{-1} band observed in the (YY) was assigned to the $E_2(4)$ as suggested by previous workers.[18,19]

Recently, we succeeded to obtain the polarized micro-Raman spectra of one needle-like t-POM single-crystal (Fig. 3.2). The strongest band at 921 cm^{-1} in the (XX) is assigned to the $A_1(4)$,
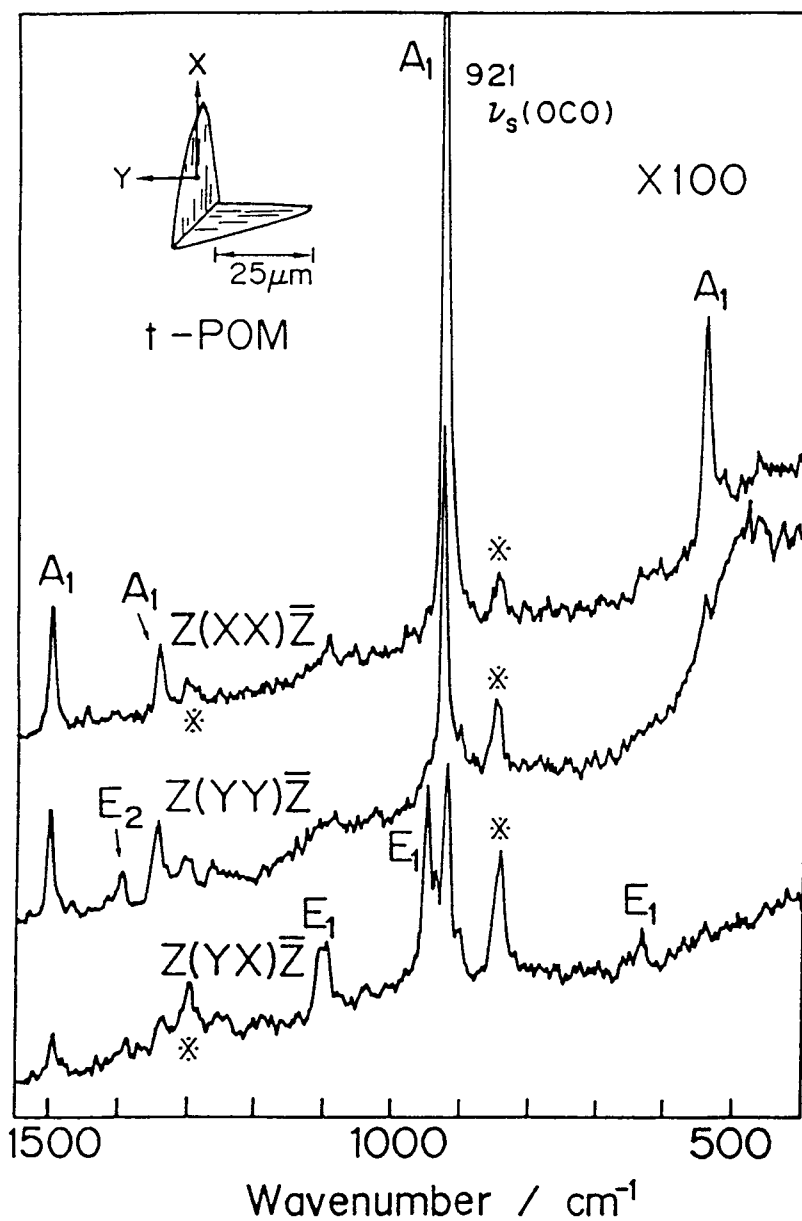
Fig. 3.1. Polarized micro-Raman spectra for the moth-shaped single crystal of t-POM generated from the thermal induced solid-phase transition of the same shaped o-POM single crystal. Bands marked with asterisks are spoiled bands by the objective itself.
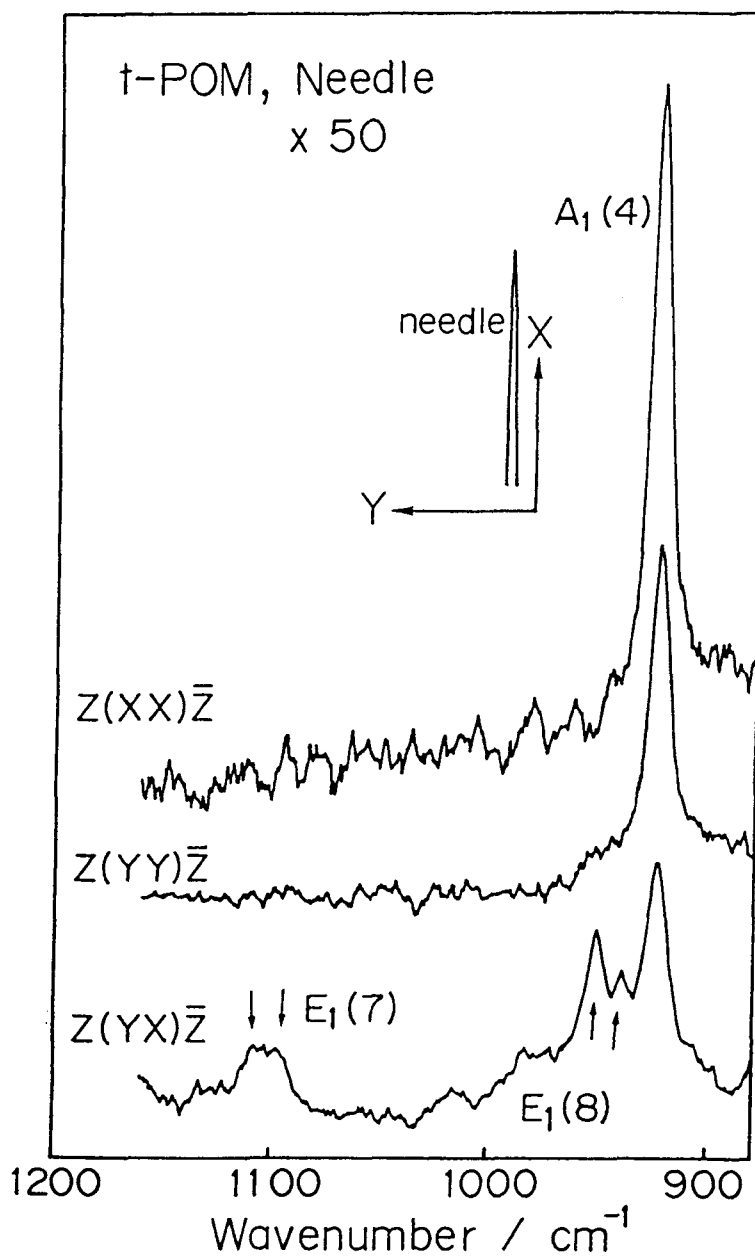
Fig. 3.2. Polarized micro-Raman spectra of needle-like single crystal of ECC t-POM.

$\nu_s(OCO)$. This long axis (X direction) has been determined to be parallel to the *c* axis. From the results of the polarized Raman spectra of these single crystals, it becomes clear that the direction of the needle axis of the needle-like single crystal and that of the striation of the moth-shaped single crystal are parallel to the crystallographic *c* axis.

Figs. 3.3 and 3.4 show ordinary right-angle polarized Raman spectra of molecular and lattice modes of the pressurized superdrawn filament. All the sharp bands appearing in the (XX) spectrum should be assigned to the A_1 species. The bands observed in the (YX) spectrum, except for the $E_1(11)$ band at 40 cm^{-1}, appear at the same frequencies as the infrared perpendicular bands, so that they are assigned undoubtedly to the E_1 species.

As for the E_2 modes, in which the neighboring structural units in an n/m uniform helix (with n≥5) move with the phase difference of $4m\pi/n$, is potentially Raman active. However, in most helical polymers, the E_2 modes are too weak to be detected. From the group theoretical consideration the E_2 modes are observed in the (YY) and/or (YZ) spectra, and not observed in the (XX). Thus, the 1388 cm^{-1} band, which had been assigned to $A_2(2)$ by Zerbi et al.,[18] and the 65 cm^{-1} bands were confirmed to be assigned to the $E_2(4)$, and $E_2(12)$, respectively. Very weak bands were detected by measuring with higher amplification as shown in Fig. 3.5. The polarized Raman spectral data obtained for the superdrawn filament are summarized Table 3.2.

3.3.2. E_2 Modes of t-POM and t-POM-d_2

In general, scattering power of E_2 modes are weak compared

t-POM
pressurized
superdrawn filament

Z(XX)Y

A₁(2) 1491
A₁(3) 1339
A₁(1) 2923
E₂(1)

X(YY)Z
A₁(2)
A₁(1)
E₂(5)
E₂(2) 2957
E₂(1) 2997

Z(YZ)Y
E₂(4) 1388
E₂(6)
E₂(7) 948
E₂(5) 1334
E₂(6) 1021

A₁(5) 539
A₁(4) 919
A₁(4)
E₂(9) 552

Z(YX)Y
E₁(1) 3005
E₁(2) 2925
E₁(4) 1436
E₁(5) 1294
E₁(7)
1106 1095
E₁(8)
949 937
E₁(9) 639

Wavenumber / cm⁻¹

3000   2800   1400   1200   1000   800   600
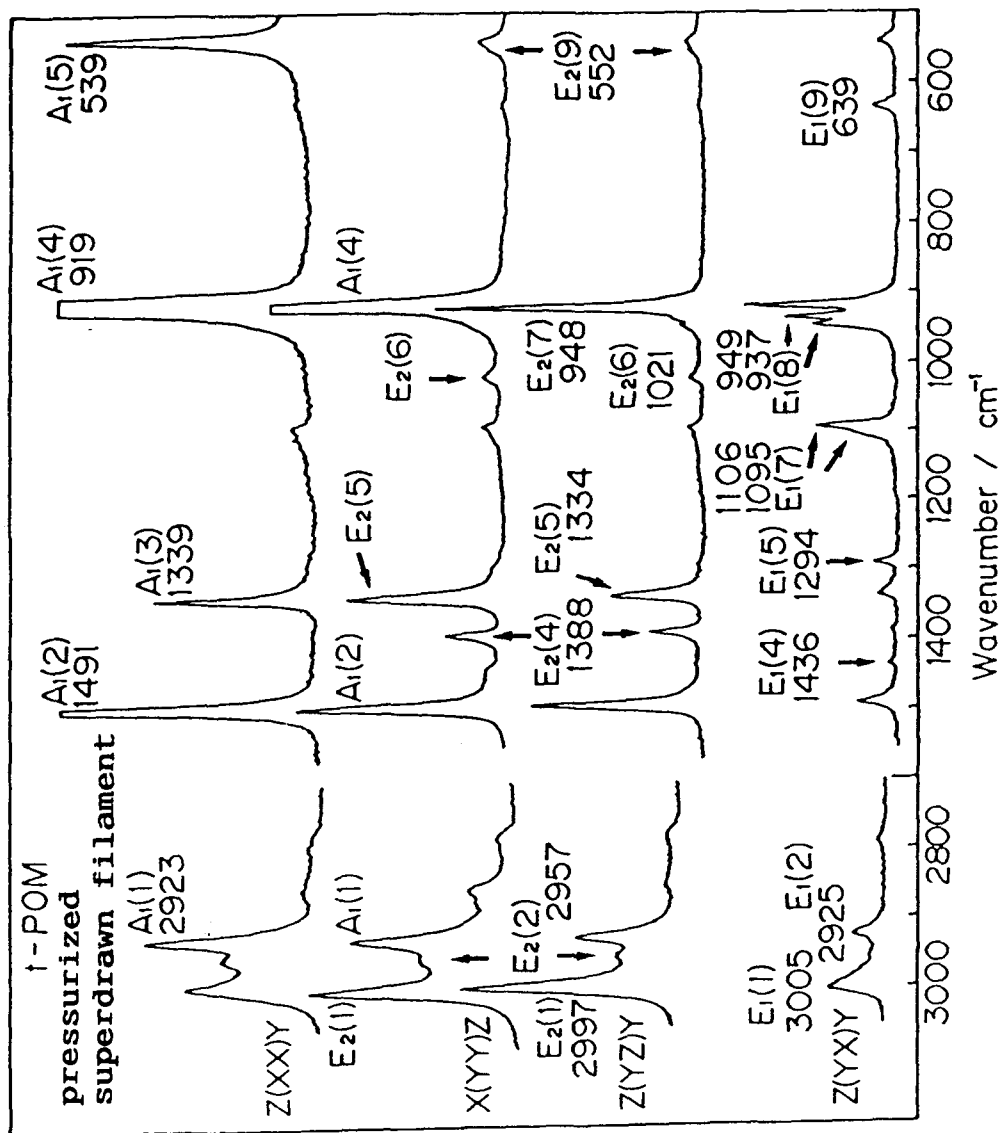
Fig. 3.3. Polarized Raman spectra of pressurized superdrawn sample of t-POM.
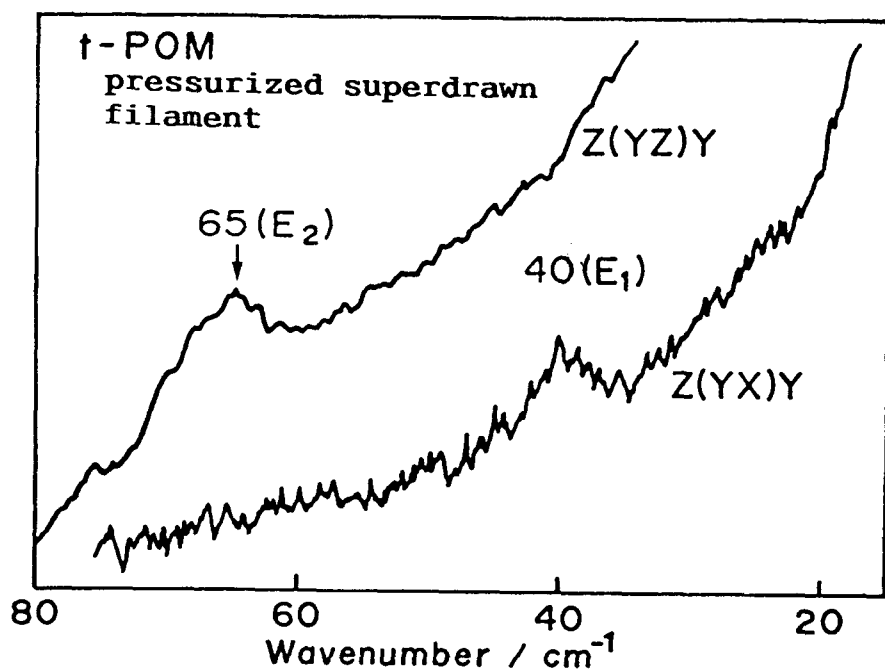
Fig. 3.4. Polarized Raman spectra of pressurized superdrawn
sample of t-POM.

Table 3.1. Factor group analysis of t-POM crystal

Phase angle	Species	No. normal modes	Polarization	
			IR	Raman
0	A_1	5	forbidden	$(\alpha_{aa}+\alpha_{a*a*})$, α_{cc}
0	A_2	5	μ_c	forbidden
$10\pi/9$	E_1	11 x 2	(μ_a, μ_{a*})	$(\alpha_{ac}, \alpha_{a*c})$
$20\pi/9$	E_2	12 x 2	forbidden	$(\alpha_{aa}-\alpha_{a*a*}, \alpha_{a*a})$
$30\pi/9$	E_3	12 x 2	forbidden	forbidden
$40\pi/9$	E_4	12 x 2	forbidden	forbidden

a*: The perpendicular direction to the ac plane
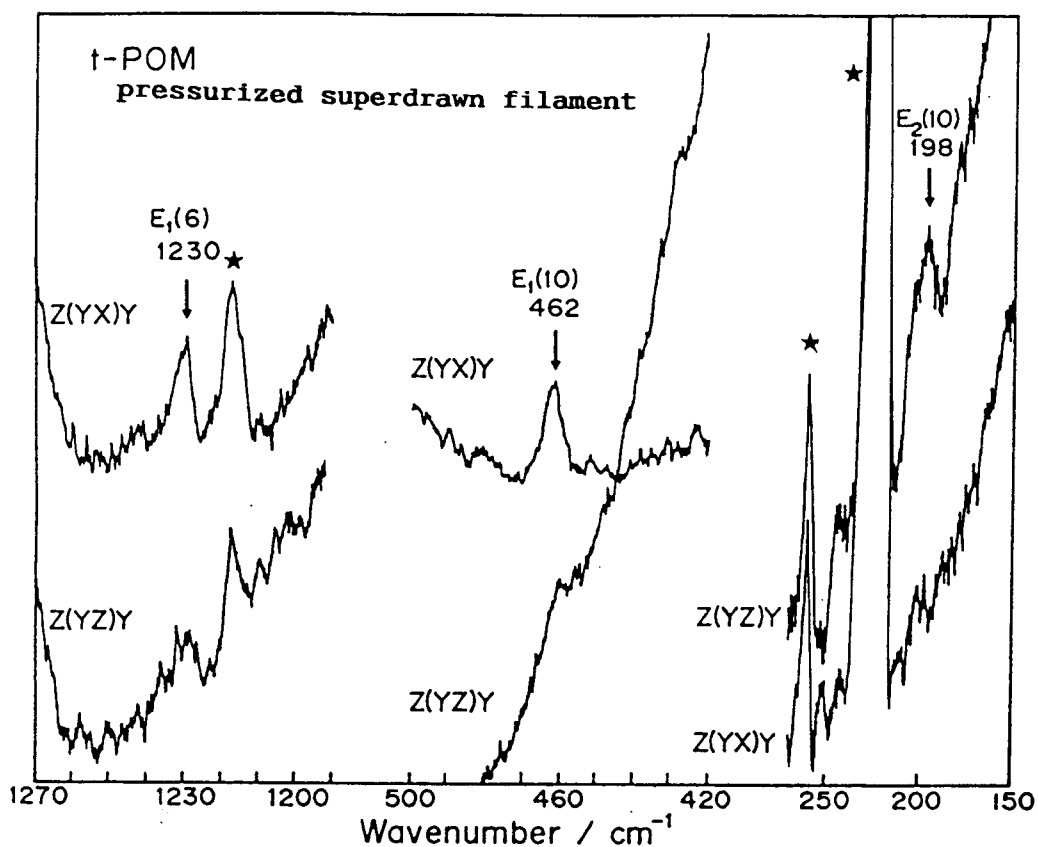
Fig. 3.5. Raman spectra of the pressurized superdrawn sample of t-POM measured with high amplification. Bands marked with asterisks are due to the natural emittion from the Ar^+ laser.

with those of A_1 and E_1 modes. We consider that this mode is very sensitive to the structural orderliness in the crystalline part.[21] In order to measure the weak E_2 bands more definitely, Raman spectrum was measured with high amplification on the powder sample of needle-like single crystals cooled at liq. He temperature (Fig. 3.6). The bands at 1482 and 907 cm^{-1} were newly detected and assigned to $E_2(3)$ and $E_2(8)$, respectively. On the figure, the bands marked with arrows were assigned to the E_2 on referring to the Raman polarization data of the superdrawn filament. The assignments and frequencies of the bands are described on the figure.

As for the vibrational assignments of t-POM-d_2, infrared-active A_2 and E_1 modes have already been established,[15] and distinct Raman bands have been assigned to A_1 or E_1 modes,[15] except for a weak band at 1049 cm^{-1}. Little has been known about the E_2 modes of t-POM-d_2 except for the 57 cm^{-1} band due to the $E_2(12)$ band.[18]

Since the needle-like single crystal of t-POM-d_2[27] has the highest crystal perfection, appearance of the E_2 band in Raman spectrum is expected. Fig. 3.7 shows Raman spectra of the powder sample of needle-like t-POM-d_2 single-crystal.[26] The 2267 and 1049 cm^{-1} bands which are assigned to the $E_2(1)$ and $E_2(4)$ modes, respectively. There are observed three very weak E_2 Raman bands as marked in Fig. 3.7.

3.3.3. LO-TO Splitting of the E_1 Bands of t-POM

In Figs. 3.1, 3.2 and 3.3, there are observed doublets around 1100 and 940 cm^{-1} in the (XY) spectrum. The low-frequency components of the doublets at 1095 and 937 cm^{-1} are assigned to

Table 3.2. The Raman and infrared vibrational spectra of t-POM

Modes	Frequencies (cm^{-1})		Calculated
	Observed		
	Raman	IR	
$A_1(1)$	2923 XX m[a]	ia	2924[b]
$A_1(2)$	1491 XX vs		1508
$A_1(3)$	1339 XX s		1330
$A_1(4)$	919 XX vs		916
$A_1(5)$	539 XX s		587
$A_2(1)$	ia	2985[c]	2977
$A_2(2)$		1358	1425
$A_2(3)$		1093	1118
$A_2(4)$		895	922
$A_2(5)$		220	237
$E_1(1)$	3005 YX m	2999	2982
$E_1(2)$	2925 YX m	2928	2926
$E_1(3)$	1468[d]	1470	1506
$E_1(4)$	1436 YX w	1435	1407
$E_1(5)$	1294 YX m	1292[e]	1318
$E_1(6)$	1230 YX vw	1240	1169
$E_1(7)$	1106 YX vw		
	1095 YX m	1093	1072
$E_1(8)$	949 YX w		
	937 YX	938	930
$E_1(9)$	639 YX m	633	634
$E_1(10)$	462 YX vw	457	483
$E_1(11)$	40 YX m	--	22
$E_2(1)$	2997 YZ s	ia	2978[f]
$E_2(2)$	2957 YZ m		2897
$E_2(3)$	1482[d]		1498
$E_2(4)$	1388 YZ m		1393
$E_2(5)$	1334 YZ sh		1334
$E_2(6)$	1021 YZ w		1133
$E_2(7)$	948 YZ vw		938
$E_2(8)$	907[d]		912
$E_2(9)$	552 YZ vw		555
$E_2(10)$	198 YZ vw		189
$E_2(11)$	---		176
$E_2(12)$	65 YZ m		56

a Relative intensity: vs;very strong, s;strong

  m;medium, w;weak, vw;very weak, sh;shoulder.

b Refer to Ref. 15, c Refer to Ref. 27

d Needle crystal's data (at liq. He temp.)

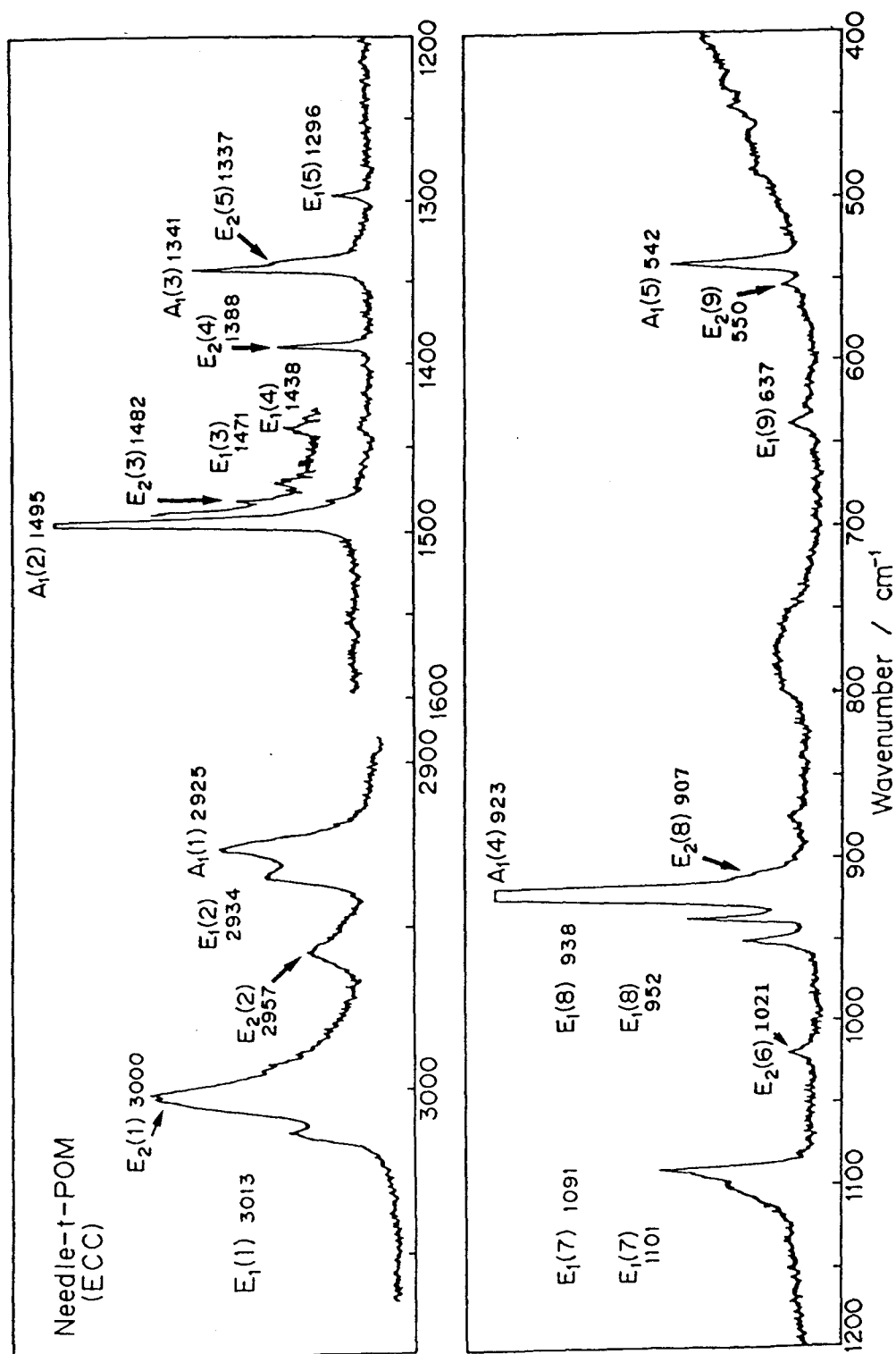e pressurized superdrawn filament's data

f Refer to Ref. 19

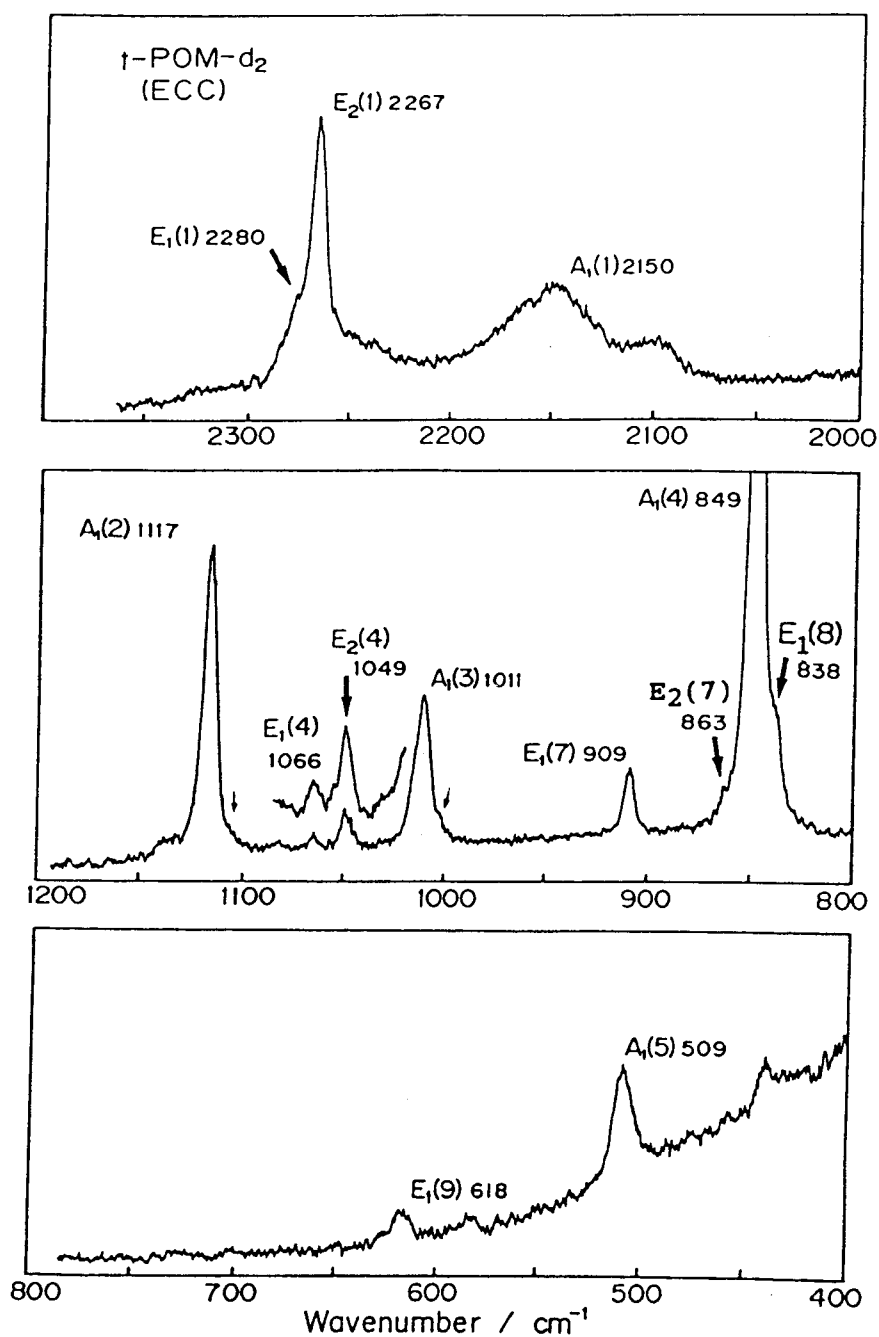Fig. 3.6. Raman spectra of needle-like single crystals of ECC t-POM at liquid He temperature.

Fig. 3.7. Raman spectra of needle-like single crystals of ECC t-POM-d$_2$ at room temperature.

Table 3.3. The Raman and infrared
vibrational spectra of t-POM-d_2

Modes	Frequencies(cm^{-1})		
	Observed		Calculated
	Raman	IR	
$A_1(1)$	2150	ia	2121[a]
$A_1(2)$	1117		1126
$A_1(3)$	1011		1013
$A_1(4)$	849		828
$A_1(5)$	509		557
$A_2(1)$	ia		2193
$A_2(2)$		1048[b]	1154
$A_2(3)$		958	1026
$A_2(4)$		830	769
$A_2(5)$		199	212
$E_1(1)$	2280		2207
$E_1(2)$	~2100		2121
$E_1(3)$	----	1159	1178
$E_1(4)$	1130	1127	1145
$E_1(5)$	1080	1083	1047
$E_1(6)$	1066	1065	1044
$E_1(7)$	909	908	916
$E_1(8)$	838	840	810
$E_1(9)$	618	617	618
$E_1(10)$	---	365	372
$E_1(11)$	--	--	21
$E_2(1)$	2267	ia	2227[c]
$E_2(2)$	----		2122
$E_2(3)$	1108		1112
$E_2(4)$	1049		1057
$E_2(5)$	1002		1014
$E_2(6)$	---		994
$E_2(7)$	863		842
$E_2(8)$	---		830
$E_2(9)$	---		518
$E_2(10)$	---		183
$E_2(11)$	---		158
$E_2(12)$	58[d]		51

[a] Refer to Ref. 15, [b] Refer to Ref. 25,
[c] Refer to Ref. 19, [d] Refer to Ref. 18.

the TO bands of the $E_1(7)$ and $E_1(8)$ modes, since the frequencies

are the same as the corresponding infrared perpendicular bands.

The high-frequency components of the doublets observed at 1106

and 949 cm^{-1} seems to be produced from lowering in symmetry for

uniform helix structure. However, the doublets never obseved

except for the E_1 bands and the high-frequency bands did not

appear in Raman spectrum of the solution-grown t-POM crystals,

which gave the same X-ray diffraction pattern with that of the

needle-like crystals. Thus, we consider that the high-frequency

components at 1106 and 949 cm^{-1} should be assigned to the LO

bands of the respective E_1 modes. Crystallographically, the t-

POM lattice belongs to a non-centrosymmetric space group,

containing one molecule passing through the unit cell.

Therefore, in theory, one crystallite should be chiral consisting

of only left-handed or right-handed molecules. However, in

actual samples the chirality is possibly diminished by structural

defects and molecular motions. The appearance of the LO bands

suggests that chirality of the lattice is held at least within

each crystal domain. In order to confirm further the fact that

the doubling of the E_1 Raman bands is caused by the LO-TO

splitting, we tried to observe the angular dispersion of the LO

bands. For the doubly degenerated E_1 modes, position of the

high-frequency component moves from the LO- to the TO-frequency,

as the angle θ between the phonon propagation vector q and the c

axis varies, while the low-frequency component remains unshifted

at the TO frequency (see Fig. 3.8). At $\theta = 90°$, the high-

frequency component appears at the highest frequency

corresponding to the LO-frequency, at $\theta = 45°$ it moves to a

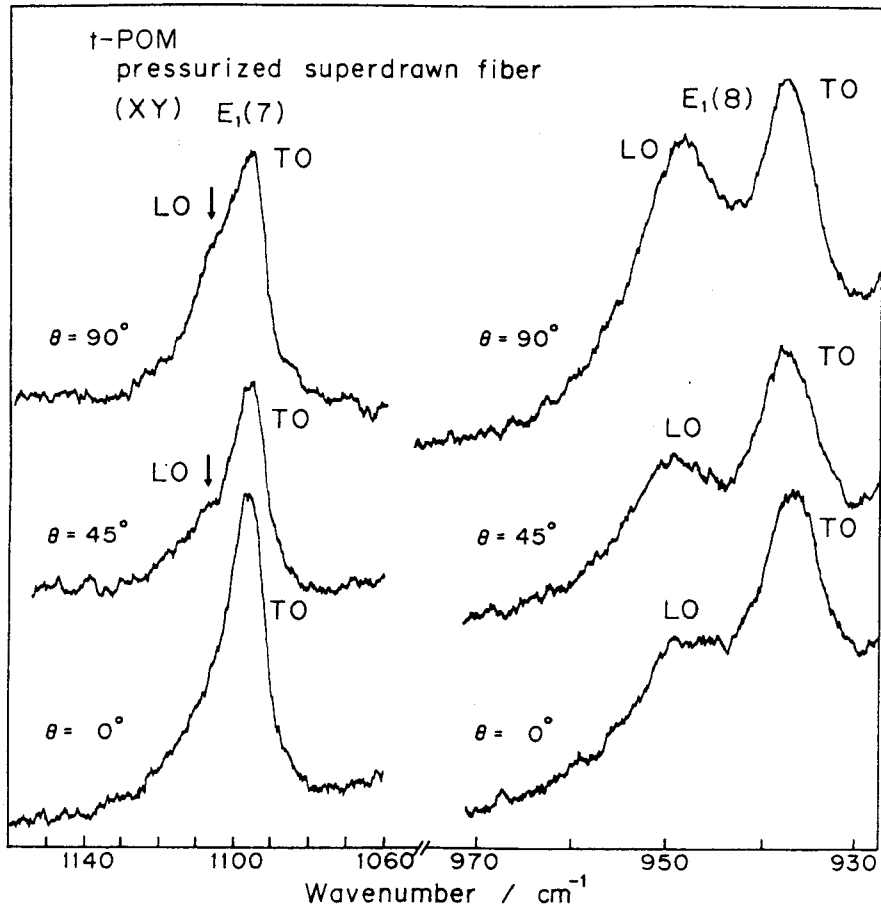position in-between the LO- and TO frequencies (the oblique

a)
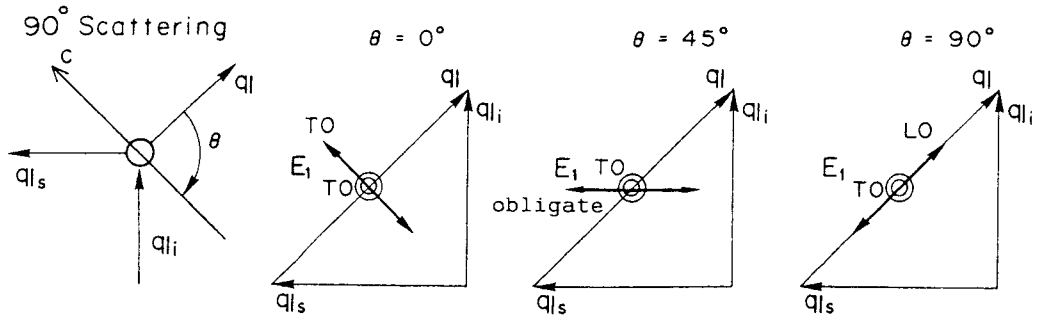
b)

Fig. 3.8. Raman scattering geometries for 90° scattering and angular dispersion of $E_1(7)$ and $E_1(8)$ Raman bands of t-POM. The incident and scattered photon propagation vectors are donoted by q_i and q_s, respectively, and the phonon propagation vector by $q = q_i - q_s$.

phonon), and at $\theta = 0°$ only the low-frequency component appears.

The experimental result is shown in Fig. 3.8 (b). Although the expected frequency shift of the high-frequency conponent did not occur so clearly for the two E_1 modes, their intensities decreased as θ moves from 90° to 0°. This suggests that the main part of the high-frequency component moves as the theory predicts, but some part remains unshifted. The latter part may be due to the opaqueness of the sample that causes scrambling in the directions of the q_i as well as q_S vectors.

Consequently, the angular dispersion of the E_1 modes certainly occurs, supporting the non-centrosymmetric lattice of t-POM.

In the case of the backward scattering, as illustrated in Fig. 3.9, when the c axis is located perpendicular to the phonon wavenumber vector $q = q_i - q_S$ (see 3.2.2), both the LO and TO components of the doubly degenerate E_1 species are observed independently of the scattering angle. In Figs. 3.1 and 3.2, the $E_1(7)$ mode appears at 1108 (LO) and 1098 (TO) cm^{-1} (with the band gap of $\Delta\nu = 10 \ cm^{-1}$) and the $E_1(8)$ mode at 952 (LO) and 940 (TO) cm^{-1} ($\Delta\nu = 12cm^{-1}$).

The magnitude of the LO-TO splitting should be approximately proportional to the infrared intensity and inversely proportional to the mode frequency.[32-34] The $E_1(7)$ and $E_1(8)$ modes for which distinct LO-TO splittings are observed give rise to very strong infrared intensities. For the $E_1(9)$ mode showing a medium-intense absorption, we expected to detect similar LO-TO splitting, but the observed Raman profile has only one peak at 636 cm^{-1}.

The Raman LO-TO splitting characteristic of polar crystals

Polar E_1 Phonon in t-POM
Back Scattering
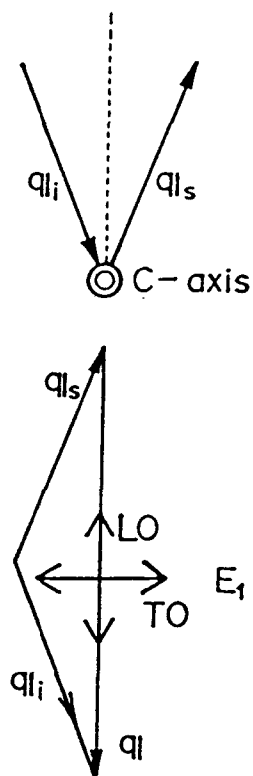
$$E : \omega_L^{\perp} + \omega_T^{\perp}$$

Fig. 3.9. Raman scattering geometries and the LO and TO modes to be measurerd for the doubly degenerate E_1 species. The incident and scattered photon propagation vectors are denoted by q_i and q_s, respectively, and the phonon propagation vector by $q = q_i - q_s$.

has been studied extensively in some ionic crystals such as quartz,[35,36] $BaTiO_3$,[37] etc. On the other hand, only limited examples are known for molecular solids. In previous papers [32,38,39] Kobayashi and his co-workers studied the angular and the polariton dispersion of the polar crystal of trioxane. The magnitudes of LO-TO splitting of the E_1 modes, corresponding to the $E_1(7)$ and $E_1(8)$ modes of t-POM, are 19.9 and 9.2 cm^{-1}, respectively. As for crystalline polymers, LO-TO splitting of 1~6 cm^{-1} has been observed for the Raman bands of Poly(vinylidene fluoride) form I (piezoelectric phase).[40]

REFERENCES

1   H. Tadokoro, S. Yasumoto, S. Murahashi and I. Nitta, J. Polym. Sci., **44**, 266(1960)

2   T. Uchida and H. Tadokoro, J. Polym. Sci., (A-2), 5, 63 (1967)

3   G. Carazzolo, J. Polym. Sci., (A), 1, 1573 (1963)

4   H. Staudinger and R. Singer, Z. Krist., **70**, 193 (1929)

5   E.W. Fischer, Ann. N. Y. Acad. Sci., **89**, 620 (1961)

6   M. Baccaredda, E. Butta, P. Guisti and F. Morelli, J. Polym. Sci., (C), **4**, 953 (1963)

7   M. Iguchi, H. Kanetsuna and T. Kawai, Makromol. Chem., **128**, 63 (1969)

8   M. Iguchi and I. Murase, Makromol. Chem., **176**, 2113 (1975)

9   M. Iguchi, Br. Polym. J., 5, 195 (1973)

10 M. Iguchi and I. Murase, J. Crystal Growth, 24/25, 596 (1974)

11 D.H. Reneker and P.H. Geil, J. Appl. Phys., 31, 1916 (1960)

12 W.J. Barnes and F.P. Price, Polymer, 5, 283 (1964)

13 D.C. Bassett, F.R. Dammont and R. Salovey, Polymer, 5, 579

(1964)

14 D.R. Carter and E.J. Baer, J. Appl. Phys., **37**, 4060 (1966)

15 H. Tadokoro, M. Kobayashi, Y. Kawaguchi, A. Kobayashi and
    S. Murahashi, J. Chem. Phys., **38**, 703 (1963)

16 K. Nakagawa, J. Polym. Lett. Edn., **21**, 933 (1983)

17 G. Zerbi and P.J. Hendra, J. Mol. Spectrosc., **27**, 17 (1968)

18 H. Sugeta, T. Miyazawa and T. Kajiwara, Polymer Lett., **7**, 251
    (1969)

19 H. Sugeta, Doctral Thesis, Osaka Univ.,Jpn., 1968

20 M. Kobayashi, Y. Itoh, H. Tadokoro, M. Shimomura and
    M. Iguchi, Polym. Commum., **24**, 38 (1983)

21 M. Kobayashi, H. Morishita, T. Ishioka, M. Iguchi,
    M. Shimomura and T. Ikeda, J. Mol. Struct., **146**, 155 (1986)

22 M. Kobayashi, H. Morishita, M. Shimomura and M. Iguchi,
    Macromolecules, **20**, 2453 (1987)

23 T. Komatsu, S. Enoki and A. Aoshima, Polym. Preprint, Jpn.,
    35, 3712 (1986)

24 S. Enoki, T. Komatsu and A. Aoshima, Polym. Preprint, Jpn.,
    35, 3716 (1986)

25 H. Morishita, M. Kobayashi and T. Komatsu, Rep. Prog. Polym.,
    Jpn., **30**, 131 (1987)

26 M. Iguchi, Polymer, **24**, 915 (1983)

27 M. Shimomura, M. Iguchi and M. Kobayashi, Polymer, **29**, 351
    (1988)

28 M. Iguchi I. Murase and K. Watanabe, Br. Polym. J., **6**, 61
    (1974)

29 M. Iguchi, Makromol. Chem., **177**, 549 (1976)

30 T. Mashimoto, T. Sakai and M. Iguchi, J. Phys., (D), **12**, 1567
    (1979)

31 H. Morishita, M. Kobayashi, M. Shimomura M. Iguchi and
    H. Kuwahara, Sci. Bull. Fac. Educ., Nagasaki Univ., No. 41, 1
    (1989)

32 M. Kobayashi, J. Chem. Phys., 76, 1187 (1982)

33 M. Born and K. Huang, *Dynamical Theory of Crystal Lattices;*
    Clarendon: Oxford, (1954)

34 W. Hayes and R. Loudon, *Scattering of Light by Crystals;*
    Wiley: New York, (1978)

35 S. M. Shapiro and J. D. Axe, Phys. Rev. B, 6, 2420 (1972)

36 M. M. Elcombe, Phys. Sci., 91, 947 (1976)

37 M. Jr. DiDomenico, S. H. Wempel and S. P. S. Porto, Phys.
    Rev., 174 , 522 (1968)

38 M. Kobayashi and K. Furumi, J. Chem. Phys., 76, 4725 (1982)

39 M. Kobayashi, K.Tashiro and N. Yagi, Jpn. J. Appl. Phys., 24,
    Suppl. 24-2, 500 (1985)

40 K. Tashiro, Y. Itoh, M. Kobayashi and H. Tadokoro,
    Macromolecules, 18, 2600 (1985)

Solid-State Phase Transition of Poly(oxymethylene) Single
Crystals from the Orthorhombic to the Trigonal Phase

4.1. Introduction

As discussed in the preceding two chapters, we accomplished
full vibrational assignments of t-POM and o-POM crystals on the
basis of polarized infrared and Raman spectra.[1-6] These spectra
were obtained on single-crystal samples with different habits[7-12]
and highly oriented filaments.[13,14]

As is known, the orthorhombic modification transforms
immediately to the stable trigonal phase when the o-POM sample is
heated[1,15,16] or subjected to mechanical deformation (by
stretching, rolling, or compression).[4] The solid-state phase
transition from o-POM to t-POM is accompanied by changes in
molecular conformation (from the 2/1 to the 9/5 helix) as well as
in molecular packing (from the orthorhombic unit cell to the
hexagonal unit cell) (Fig. 4.1). To understand thermodynamic
stabilities of the two crystal modifications of POM, elucidation
of the molecular mechanism of the phase transition is of
fundamental importance. However, details of its thermodynamic
and structural features, even the DSC thermogram,[12] remain
unclarified.

Recently, Kobayashi et al. found o-POM produced in a micron-
sized single-crystal form having a specific shape resembling a
"moth".[11] Iguchi succeeded in preparing high-purity particle
samples of o-POM comprising a number of rod-like single

crystals.[12] Using those o-POM samples, the thermal behavior (by DSC measurements) and changes in morphology and orientation (by polarized microscope and polarized infrared and Raman spectroscopies) during the solid-state phase transition have been investigated in this chapter. Origin of the thermodynamic stability of the trigonal phase is considered from the spectroscopic viewpoint. Another aim of this chapter is to clarify the crystal morphology of the t-POM phase generated from the o-POM single crystals through the thermal phase transition.

4.2. Experimental
4.2.1. Samples

The moth-shaped single crystals of o-POM (Sample I) were found in a special batch which had originally been designed to prepare needle-like single crystals of t-POM.[12] The sample-fixed Cartesian coordinates of this single crystal were defined as described in **Chapter 2**. One piece of the moth-shaped o-POM crystal was put on a slide glass. The slide glass wrapped with aluminium foil was put in a beaker and heated at 100°C for one hour in an oil bath, the o-POM crystal being transformed to the t-POM crystal having the same habit. The resultant crystal showed clear optical birefringence, characteristic of single crystal. The sample-fixed Cartesian coordinates of the resultant t-POM crystal were defined as those of the starting o-POM crystal.

The highly pure o-POM sample (Sample II) was supplied from Dr. Iguchi[12] and used for the starting material of thermal phase transition to the trigonal phase.

4.2.2. Microfocus Raman Measurements

Polarized Raman spectra of the micron-sized moth-shaped t-POM single crystal, which was obtained by the thermal phase transition of o-POM single crystal, were measured by means of the microprobe technique. Details of the instrument used were described in **Chapter 2**. The laser beam polarized in the X or Y direction was focused at a selected position on the face of the single crystal. The backward scattered light was collected by the same objective and guided into the monochromator through an analyzer for the polarization measurement. With three scattering geometries, $Z(XX)\bar{Z}$, $Z(YY)\bar{Z}$, and $Z(XY)\bar{Z}$ polarized Raman spectra of the single crystal of t-POM were recorded.

4.3. Results and Discussion

4.3.1. Thermal Behavior of Phase Transition from the Orthorhombic to the Trigonal Form

Fig. 4.1 shows the unit cells of o-POM[17] (left side) and t-POM[18] (right side). The orthorhombic modification is metastable phase at ambient temperature. On heating, o-POM transforms
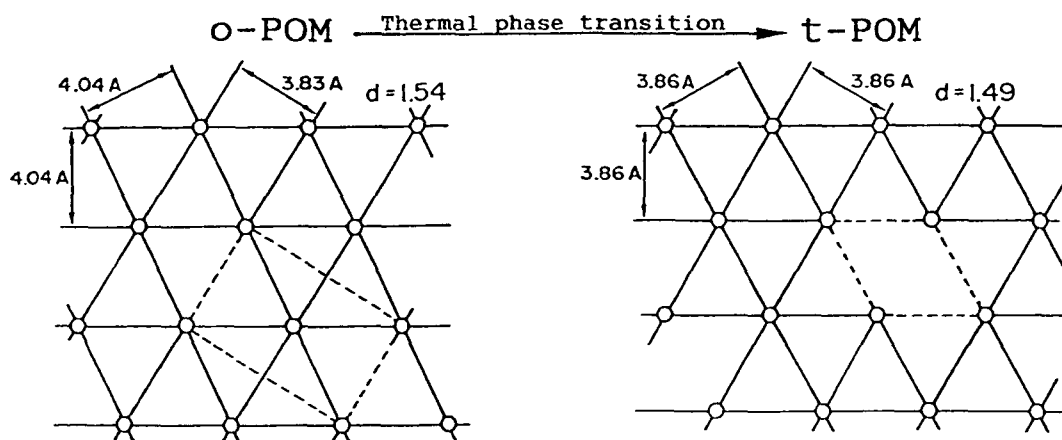

Fig. 4.1. The unit cell of o-POM (left side, redrown from ref. 17) and t-POM (right side).

irreversibly to t-POM through a monotropic transition.[15]

In the DSC thermogram (on heating process) of Sample II reported in ref. 12 [Fig. 4.2 (b)], there was no distinct sharp peak except for the strongest endothermic peak around 190°C due to the melting of the resultant trigonal phase. In the vicinity of the transition temperature, which was known to locate in the range of 75-80°C[15] from the change in the X-ray diffraction pattern, there appear diffuse multiple peaks. In our experiment done at an early stage, we obtained similar results. In that case, as usual, Sample II was put in a pan, pressed with a cover plate, and then subjected to the measurement. Considering that the appearance of diffuse multiple peaks could be caused by a partial transformation induced by a mechanical deformation that might take place during the pressing process, we prepared the DSC sample without pressing. Then, as shown in Fig. 4.2 (a), a sharp endothermic peak appeared at 69°C with $\Delta H = 0.6$ kJ/mol per CH_2O unit before the melting peak of the resultant t-POM at 187°C. The melting point of the resultant t-POM is similar to those of needle-like crystals and significantly higher than those of a typical melt-crystallized samples (ca. 175°C). The appearance of the endothermic peak of the o-POM $\rightarrow$ t-POM phase transition indicates that the instability of the orthorhombic phase is not responsible for the enthalpy term (ΔH), but for the entropy term (ΔS). This is consistent with the fact that the crystal density of o-POM ($\rho_c = 1.54$ g/cm^3) is 3% higher than that of t-POM ($\rho_c = 1.49$ g/cm^3). Therefore, o-POM crystal has higher cohesive energy, being energetically more stable, than t-POM. The higher entropy of t-POM seems to be caused by the rotational fluctuation around the chain axis of the 9/5 helix, which is cylindrically
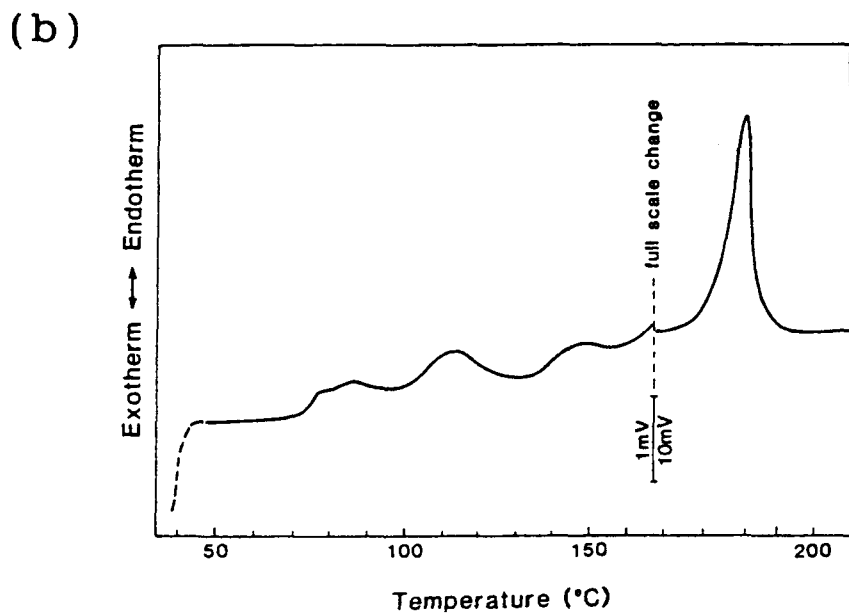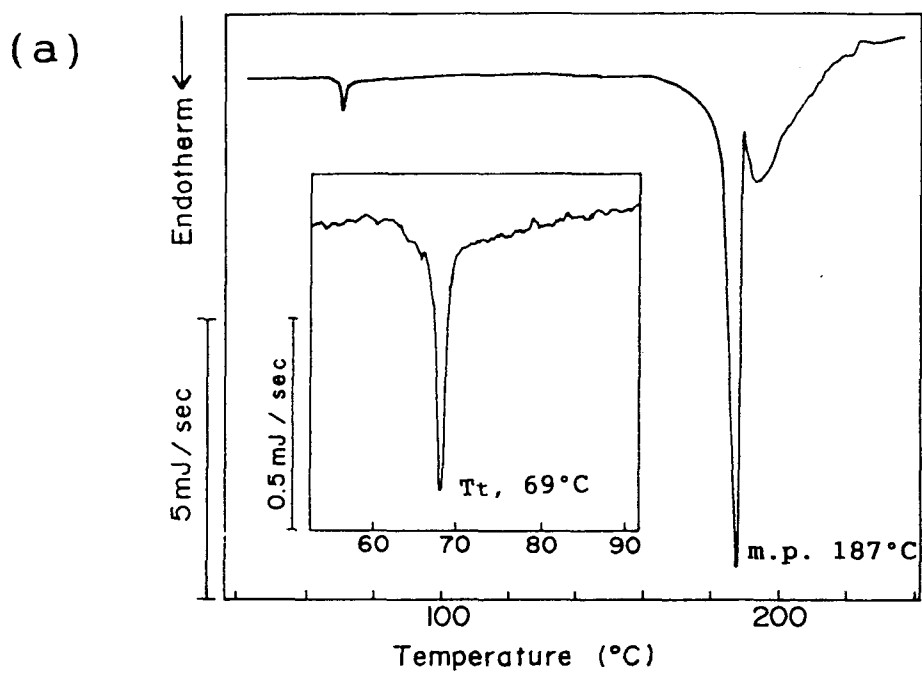
Fig. 4.2. Differential scanning calorimetry curve of particle
o-POM (a). (b); redrown from Fig.3 of ref. 12.

more symmetric and has smaller moment of inertia than the 2/1 helix of o-POM.

This is reflected in the far-infrared bands due to the lattice modes of the two crystalline phases, as shown in Fig. 4.3. In o-POM, the in-phase rotatory lattice mode $R_c(B_1)$ appears as a sharp band at 130 cm^{-1} at room temperature and shifts to 142 cm^{-1} at 93 K. On the other hand, the corresponding mode $R_c(A_2)$ of t-POM (taken on needle-like single crystals) appears at 101 cm^{-1} as a weak but distinct band at 102 K and almost smears into the background at room temperature. The smearing of the band in t-POM must be related to a dephasing of the lattice mode caused by the rotational fluctuation of the molecules.

4.3.2. Morphological Change on the Phase Transition of Poly(oxymethylene)

Changes in the morphological structure of the single crystals during the thermal and mechanically induced phase transitions from o-POM to t-POM were investigated by the polarized microscope and microfocus Raman and IR spectroscopies on both Sample I and Sample II.

It was found that the crystal habit, the crystal shape and the appearance of parallel striations on the crystal face of Sample I remained unchanged throughout the o→t thermal phase transition (by polarized microscope observation). Fig. 3.1 shows the polarized micro-Raman spectra of the moth-shaped t-POM crystal generated through the thermal phase transition. As described in **Chapter 3**, the polarized spectra are those characteristic of the t-POM single crystal. In addition, the moth-shaped t-POM crystal showed clear optical birefringence.
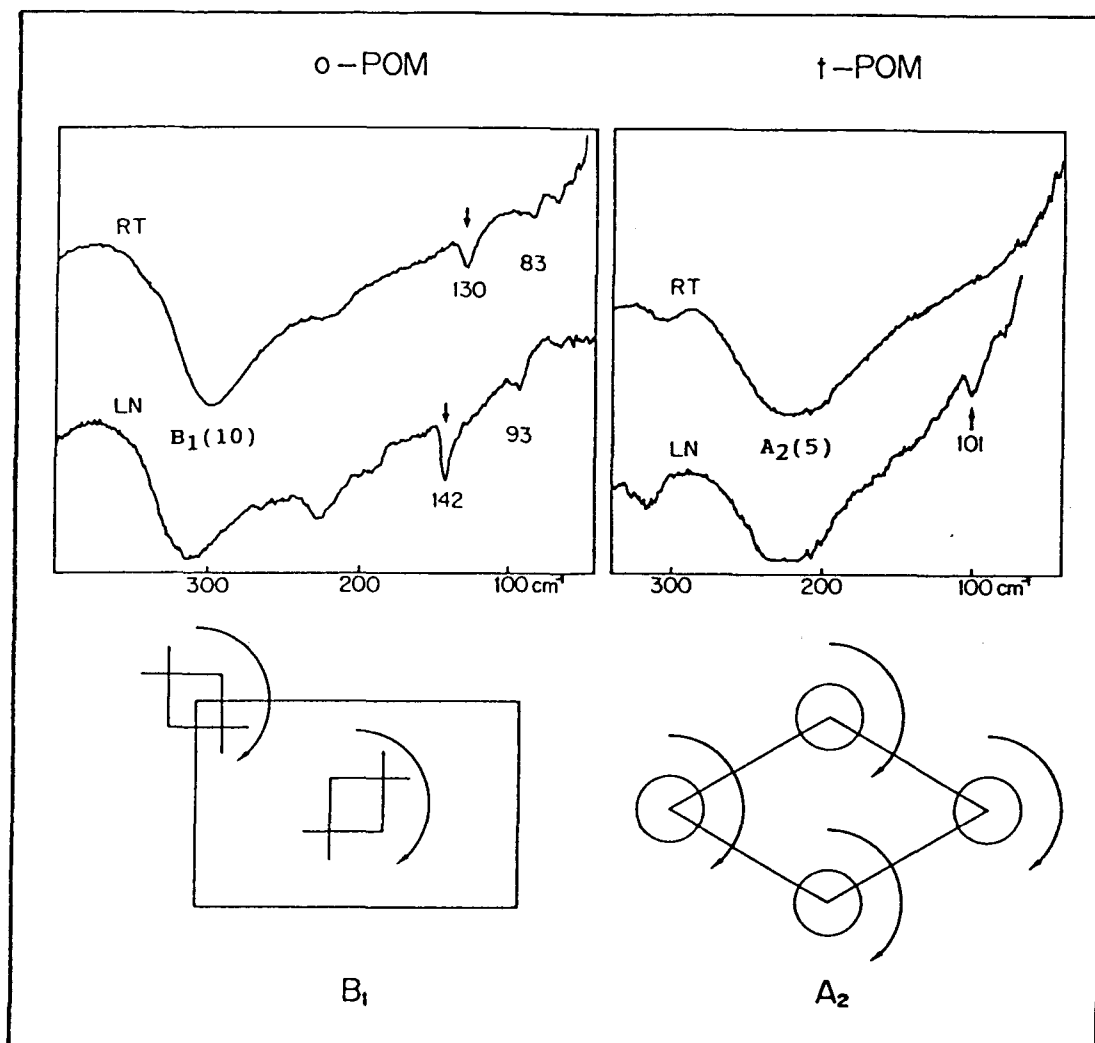
Rotatory Lattice Mode

Fig. 4.3. Far-infrared spectra of two modifications of POM measured at room and liquid N_2 temperatures; (left side) o-POM (rod-like single crystals, Sample Ⅱ), (right side) t-POM (needle-like single crystals).

Lower part; infrared-active rotatory modes $[R_c(B_1)]$ of o-POM (left side) and $[R_c(A_2)]$ of t-POM (right side).

These facts indicate that the o→t thermal phase transition of Sample I takes place with retention of the single-crystal form. The (XX) spectra in Figs. 2.14 (polarized micro-Raman spectra of the moth-shaped o-POM single crystal) and 3.1 show that the orientation of the fiber axis remains unchanged through the transition.

As shown in Fig. 4.4, the o→t thermal phase transition of Sample II (comprising a number of the rod-like single crystals) was followed by far-infrared spectrum. The intensity of the 297 cm^{-1} band due to the $B_1(10)$ mode of o-POM decreases with rising temperature and disappears at 363 K, while the 220 cm^{-1} band due to the $A_2(5)$ mode of t-POM gets stronger. Since the reverse spectral change did not occur on cooling, the thermal phase transition is monotropic.

The o→t phase transition is induced also by mechanical deformation. Fig. 4.5 shows mid-infrared spectra of POM samples obtained by heating (above 100°C) (upper spectrum) and by grinding (lower spectrum) Sample II. Fig. 4.6 shows far-infrared spectral change on the thermal (upper part) and the mechanical-induced phase transition (lower part) of Sample II. In the thermal transition, the bands of o-POM disappear perfectly and the resultant spectrum shows only the bands characteristic of t-POM.[22] In the mechanical transition, the o-POM bands remain more or less as marked with asterisks.

The infrared spectra of the t-POM transformed from an ECC sample of o-POM (Sample II) are very close to that of needle-like single crystals (ECC) of t-POM. Shimomura et al. have reported[19-21] that the infrared spectrum of t-POM is strongly affected by the crystal morphology of the samples. The bands due
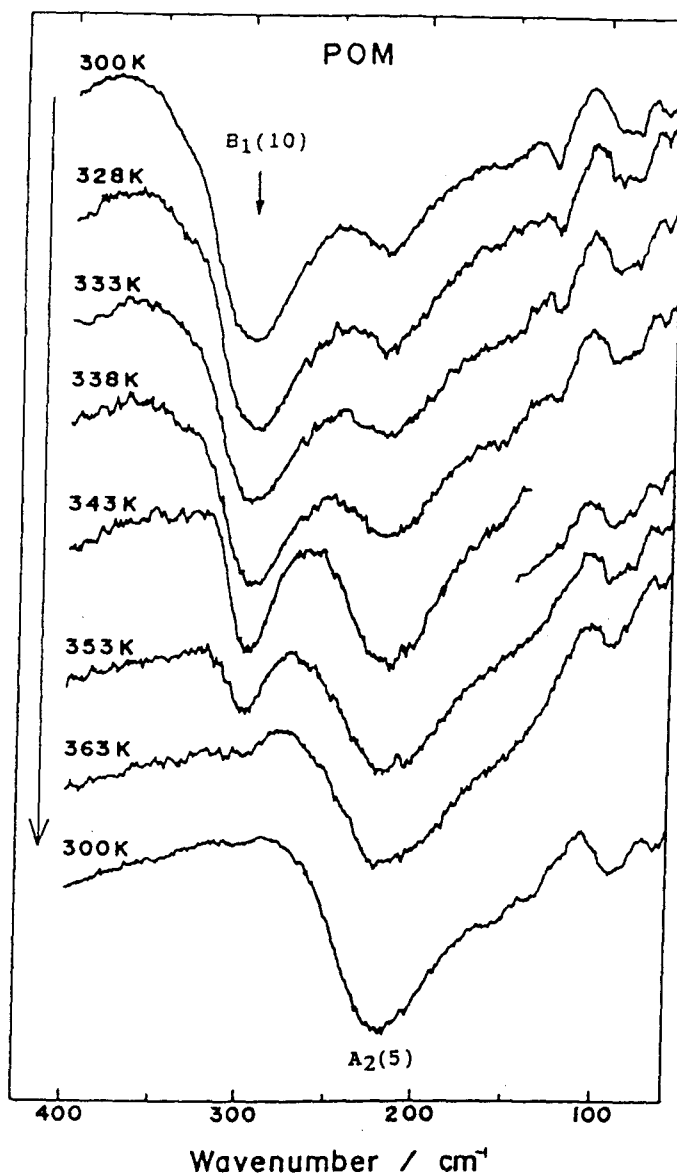
Fig. 4.4. Far infrared spectral change on the thermal transition from the particle o-POM crystals to trigonal phase.
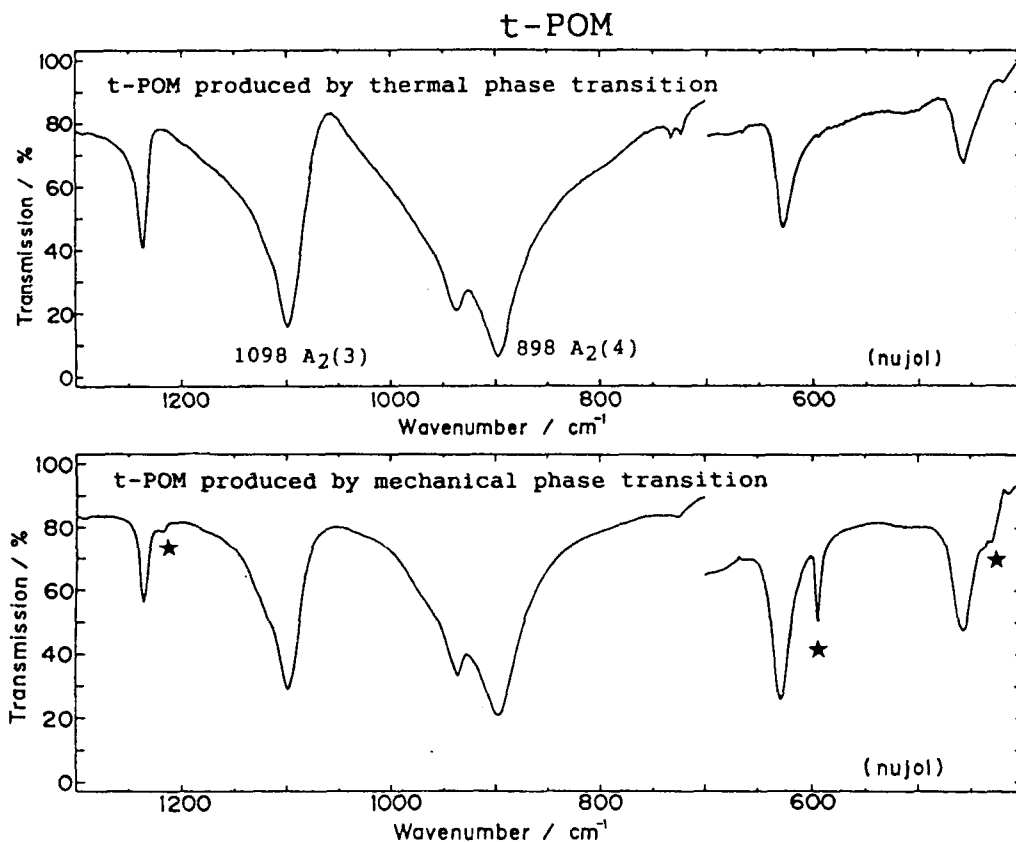
t-POM

Fig. 4.5. Mid-infrared spectra of t-POM produced by the thermal phase transition (upper) and the mechanical deformation induced phase transition (bottom) from particle o-POM to t-POM phase. The bands indicated by the asterisks are due to the orthorhombic phase.
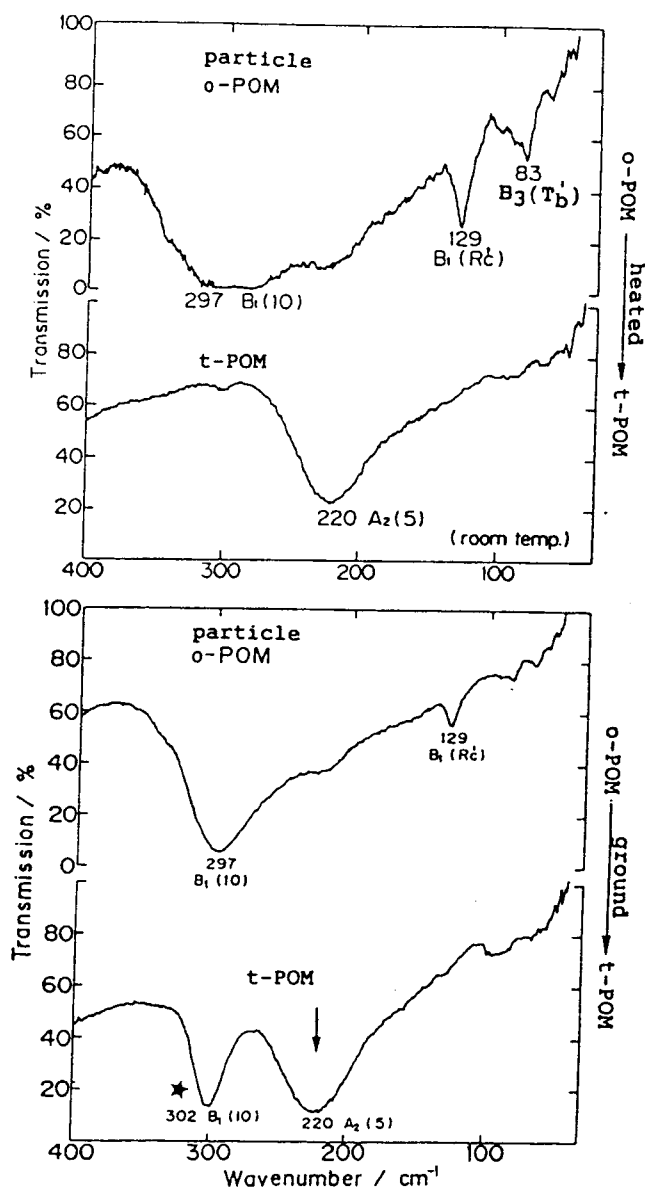
Fig. 4.6. Far infrared spectral change on the thermal phase transition (upper) and the mechanical deformation induced phase transition (bottom) from the particle sample of o-POM to t-POM phase. The bands indicated by the arrows are due to the trigonal phase.

to the A_2 symmetry species having transition dipole along the chain axis exhibit remarkable high-frequency shift (by as large as 100 cm^{-1}) as the sample goes from ECC to FCC, whereas the infrared-active E_1 bands having transition dipoles perpendicular to the chain axis and the infrared-inactive Raman bands of the A_1 and E_2 species are unshifted. Such a very specific spectral feature can be utilized for the characterization of the morphological structure of t-POM samples. The A_2 frequencies of typical FCC and ECC crystals, and those of the t-POM sample generated from Sample II through the o→t thermal phase transition are summarized in Table 4.1. It is confirmed that the t-POM crystal generated through the phase transition consists of extended molecular chains. The high melting point (at 187°C) of the t-POM crystal, as described in the preceding section, supports that the morphology of the resultant t-POM crystal is of the ECC-type. As described in the next chapter, the o-POM particles (Sample II) used as the starting material are of ECC morphology, and the o-POM crystal of the FCC type gives the t-POM crystal of the FCC type through the thermal phase transition. Therefore the ECC or FCC morphology of the starting crystals is kept on the thermal phase transition.

Table 4.1. A_2 modes in t-POM Crystals

A_2 modes	Solution grown(FCC)	Needle crystal(ECC)	Particled t-POM (This work)
(2)	1385	1385	1384 cm^{-1}
(3)	1136	1097	1098
(4)	1002	897	898
(5)	235	220	220

The structural changes accompanied with the thermal phase transition from the orthorhombic to trigonal phase were followed for the first time on micron-sized single crystal by using the Raman microprobe technique.

REFERENCES

1. M. Kobayashi, H. Morishita, M. Shimomura and M. Iguchi, Macromolecules, **20**, 2453 (1987)

2. M. Kobayashi, H. Morishita, T. Ishioka, M. Iguchi, M. Shimomura and T. Ikeda, J. Mol. Struct., **146**, 155 (1986)

3. H. Morishita and M. Kobayashi, Rep. Progr. Polym. Phys. Phys. Jpn., **30**, 131 (1987)

4. H. Morishita, M. Kobayashi, M. Shimomura, M. Iguchi and H. Kuwahara, Sci. Bull. Fac. Edyc., Nagasaki Univ., **41**, 1 (1989)

5. H. Morishita, M. Kobayashi, M. Shimomura and M. Iguchi, Sci. Bull. Fac. Educ. Nagasaki Univ., **39**, 47 (1988)

6. M. Kobayashi, T. Adachi, Y. Matsumoto, H. Morishita, T. Takahashi, K. Ute and K. Hatada, J. Raman Spectrosc., **24**, 533 (1993)

7. M. Iguchi, H. Kanetsuna and T. Kawai, Makromol. Chem., **128**, 63 (1969)

8. M. Iguchi and I. Murase, Makromol. Chem., **176**, 2113 (1975)

9. M. Iguchi, Br. Polym. J., **5**, 195 (1973)

10. M. Iguchi and I. Murase, J. Crystal Growth, **24/25**, 596 (1974)

11. M. Kobayashi, Y. Itoh, H. Tadokoro, H. Shimomura and M. Iguchi, Polym. Commun., **24**, 38 (1983)

12. M. Iguchi, Polymer, **24**, 915 (1983)

13. T. Komatsu, S. Enoki and A. Aoshima, Polym. Preprint. Jpn.,

35, 3712 (1986)

14. S. Enoki, T. Komatsu and A. Aoshima, Polym. Preprint. Jpn., 35, 3716 (1986)

15. V. Zamboni and G. Zerbi, J. Polym. Sci., Part C, 7, 153 (1964)

16. M. D'Alagni, P. De Santis, A. M. Liquori and L. Mazzarella, Nuovo Cimentc, XXXI, 1368 (1964)

17. G. A. Carazzolo and M. Mammi, J. Polym. Sci., Part A, 1, 965 (1963)

18. H. Tadokoro, T. Yasumoto, S. Murahashi and I. Nitta, J. Polym. Sci., 44, 266 (1960). T. Uchida and H. Tadokoro, Polym. Phys. Ed., 5, 63 (1967)

19. M. Shimomura, M. Iguchi, Polymer, 23, 509 (1982)

20. M. Shimomura, M. Iguchi and M. Kobayashi, Polymer, 29, 351 (1988)

21. M. Shimomura, Y. Tanabe, Y. Watanabe and M. Kobayashi, Polymer, 31, 1411 (1990)

22. H. Tadokoro, M. Kobayashi, A. Kobayashi and S. Murahashi, J. Chem. Phys., 38, 703 (1963)

Chapter 5.

Pressure-Induced Phase Transition of Poly(oxymethylene) from the
Trigonal to the Orhtorhombic Phase:
Effect of Morphological Structure

5.1. Introduction

As for solid-state phase transition of poly(oxymethylene)
from the trigonal to the orthorhombic form, Preedy et al.[1]
suggested that the phase transition occurred when t-POM was
compressed at low temperature. Miyaji and Asai[2] found by means
of X-ray diffraction that the trigonal form transformed partly to
the orthorhombic form by compressing a t-POM sample (solution
grown lamellar crystal) in a diamond anvil cell at a pressure as
high as 1.4 GPa.

The trigonal form is obtained in variuos morphological
structures situated in-between the two extreme cases of fully
extended chain crystal (ECC) and folded chain crystal (FCC),
depending on conditions of sample preparation and/or of sample
processing. Typical ECC samples have been obtained as micron-
sized needle-like[3-5] and feather-shaped[6] single crystals through
a heterogeneous cationic polymerization of trioxane. Micron-
sized moth-shaped[7,8] and rod-like[7,8] single crystals obtained
through thermal phase transition of o-POM single crystals belong
to this category[9-11] (refer to the preceding chapter).
Especially, the needle-like single crystal is known as a polymer
whisker having the highest crystal perfection. A typical FCC
sample has been obtained by crystallization from dilute solutions

as hexagon-shaped lamellar crystals consisting of regularly folded molecular chains, with the stem length of about 10 nm.[12,13]

In a series of previous papers,[14-17] it has been demonstrated that the vibrational spectrum of t-POM exhibits a specific change depending on crystal morphology of the samples. The bands due to the A_2 symmetry species, having the transition dipole moments along the chain axis, show remarkable high-frequency shifts (by as large as 100 cm^{-1}) in the FCC sample compared with those of the ECC sample. On the other hand, the E_1 bands having the transition dipole moments perpendicular to the chain axis and the infrared-inactive A_1 and E_2 Raman bands appear at the same frequencies in both FCC and ECC samples. Such a specific spectral phenomenon can be used for the characterization of the morphological structure of t-POM samples.

In this chapter, the pressure-induced phase transition from t-POM to o-POM is investigated by means of infrared and Raman spectroscopies, using typical ECC and FCC samples of t-POM as the starting materials. Our efforts are focused on solving following problems.

1) We are concerned with the role of the morphological structure in the solid-state phase transition of POM. It is important to know how the phase transition behavior of POM is influenced by the crystal morphology of the starting sample and whether the original morphology is retained or altered during the transition.

2) Concerning the origin of the above-mentioned specific spectral feature found in t-POM, it is important to confirm whether the spectral change with morphology is limited to the

case of t-POM or it is generally observable for polymer crystals including o-POM.

5.2. Experimental Section

The typical FCC sample of t-POM used was deposited from a 0.5 wt% bromobenzene solution of Delrin 500 (E. I. du Pont de Nemours & Company, Inc., Wilmington, DE) kept at 130°C. The precipitates were freeze-dried with n-hexane, giving a fine powder sample (solution grown t-POM sample). The typical ECC sample used was the needle-like single crystals of t-POM.

The t-POM samples of both ECC and FCC, in the neat or in a mixture with KBr powder, were compressed in a piston cylinder cell made of stainless steel at various pressures up to 2.5 GPa for 10-30 min. After removal of pressure, the obtained pellets of diameter 13 mm were picked out of the cell and subjected to the spectral measurements.

Absorption spectra in the mid-infrared region were measured with a JASCO A3 grating spectrometer and a JASCO 5MP FT-IR spectrometer. Far-infrared spectra were taken with a HITACHI FIS-3 grating spectrometer. The Raman spectra were measured with a JASCO NR-1000 double monochromator using the 514.5 nm excitation beam from an Ar^+ laser.

5.3. Results and Discussion

5.3.1. Spectral Changes on Phase Transition

The pressure-induced phase transition of POM is accompanied by changes in molecular conformation (from the 9/5 to 10/5 helix) and molecular packing (from the hexagonal to orthorhombic unit cell). The transition occurs in the direction opposite to the

thermal phase transition.

Fig. 5.1 shows changes in the mid-infrared spectrum of the ECC (right) and FCC (left) samples of t-POM with increasing magnitude of the applied pressure. Of the two spectra indicated by the same magnitude of pressure, the lower one is of the sample compressed for a longer time (about five times). The absorption bands associated with the generated orthorhombic form (marked with arrows) increase in intensity with increasing pressure or duration of compression. When the compressed samples are heated at about 100°C for an hour or more, all the o-POM bands disappear completely through the thermal phase transition to t-POM, as indicated at the bottom of each series of spectra.[7] These bottom spectra are almost the same as those of the starting t-POM samples. Fig. 5.2 shows the Raman spectral changes for the same procedures. The 909 cm^{-1} band due to the generated orthorhombic phase increases in intensity with increasing pressure, and disappears completely on heating above 100°C.

The conversion of the pressure-induced phase transition is plotted as a function of the magnitude of applied pressure in Fig. 5.3. Here, the conversion, c, was estimated from the integrated absorption intensity ratio of the 630 cm^{-1} band assigned to $E_1(9)$ of t-POM and the 595 cm^{-1} band assigned to $B_2(9)$ of o-POM, I_{630}/I_{595}, according to the equation

$$1/c = 1 + [I_{630}/I_{595}][\varepsilon_{595}/\varepsilon_{630}]$$

where the ratio of the molar absorption coefficients of the two bands, $\varepsilon_{595}/\varepsilon_{630}$, was evaluated as follows. The I_{595} and I_{630} values of a compressed sample were measured first, and the sample
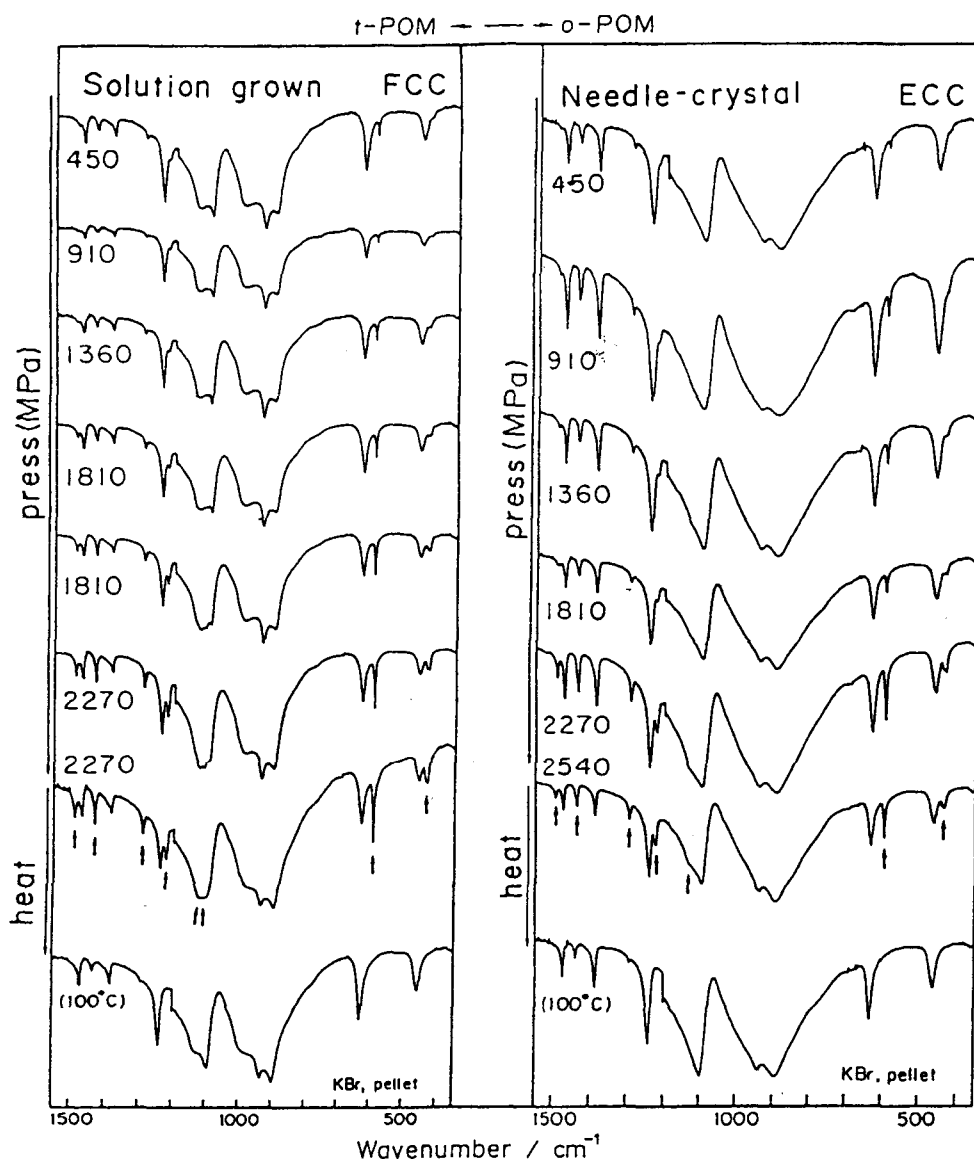
Fig. 5.1. Infrared spectral changes in the mid-infrared region on the pressure-induced phase transition of POM from the trigonal to the orthorhombic phase and successive thermal transition in the reverse direction. The bands indicated by the arrows are due to the orthorhombic phase generated. Starting [right side] from the needle-like single crystals (ECC samples) and [left side] from the solution-grown lamellar crystals (FCC sample) of the trigonal phase. The numbers indicate the applied pressure.
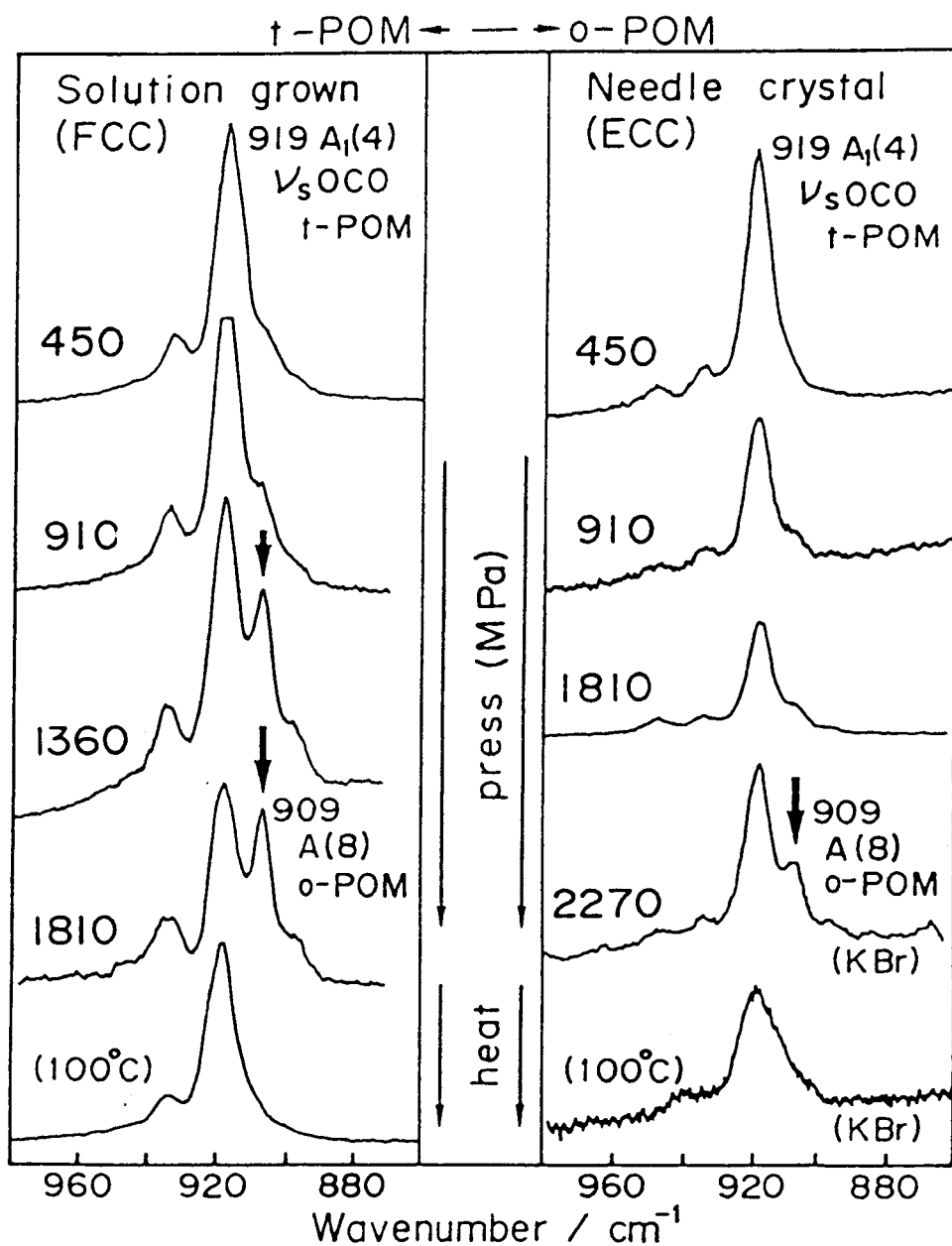
Fig. 5.2. Raman spectral change (in the C-O stretch region) on the pressure-induced phase transition of POM from the trigonal to the orthorhombic phase and successive thermal transition in the reverse direction. The bands indicated by the arrows are due to the orthorhombic phase generated. Starting from the ECC (right) and FCC (left) samples of the trigonal phase. The numbers indicate the applied pressure.
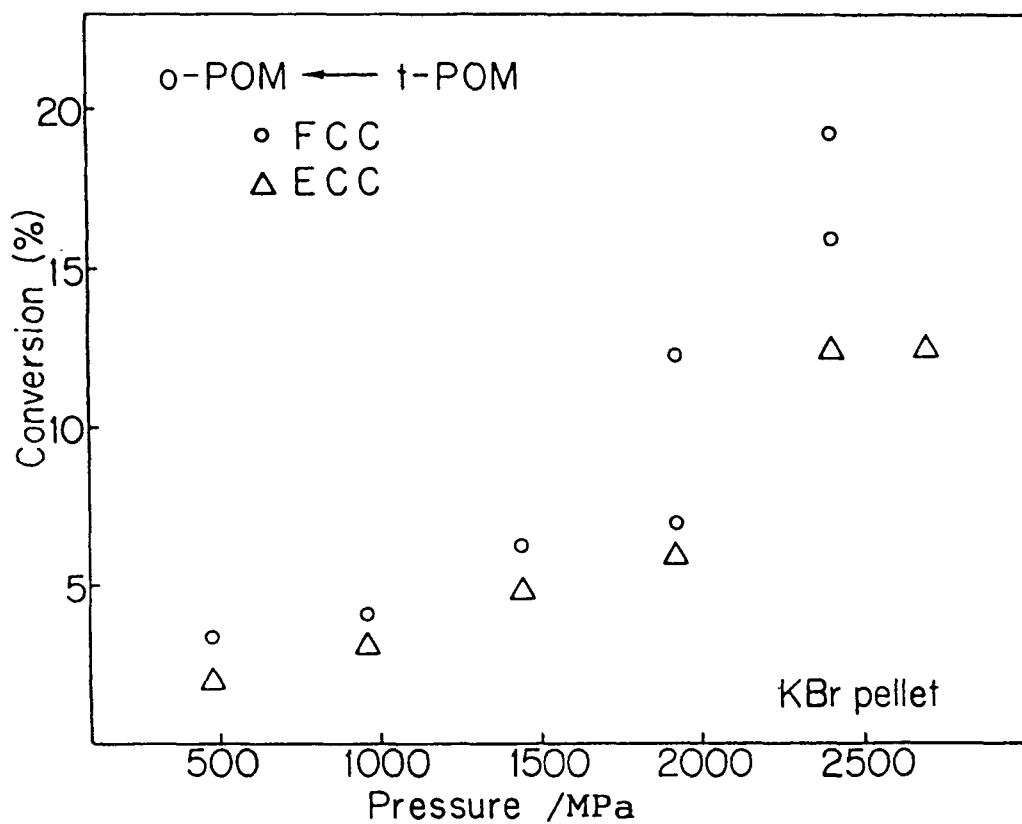
Fig. 5.3. Pressure dependence of conversion to the orthorhombic phase from the ECC and FCC samples of poly(oxymethylene).

was heated at 100°C in order to transform the orthorhombic phase to the trigonal phase, and then the increment in the I_{630} value on the thermal phase transition, ΔI_{630}, was measured. The ratio $\varepsilon_{595}/\varepsilon_{630} = I_{595}/\Delta I_{630}$ was obtained. Fig. 5.3 indicates that the solution grown FCC sample transforms more easily to o-POM than the needle-like ECC sample.

As demonstrated in **Chapter 4**, the thermodynamic stability of the trigonal phase is attributed to the rotational fluctuation of the (9/5) molecules around the chain axes. Under high pressure, such molecular motion is hindered by decrease of intermolecular distances. This stabilizes the orthorhombic phase. Hindrance of the molecular motion in o-POM is reflected to very sharp infrared and Raman band profiles compared with those of t-POM (see Figs. 5.1 and 5.2).

Contrary to the above two samples, the pressurized superdrawn filaments of t-POM having the ECC-type morphology (Chapter 3) did not transform to the o-POM phase by compressing up to 2 GPa. We recall the fact that o-POM powder samples transform to t-POM by rolling. Because the resultant t-POM part is oriented along the chain direction as shown in Figs. 2.6 and 2.7, the tensile stress along the c axis might induce this transformation. There exists residual tensile stress in the superdrawn filaments, and it stabilizes the trigonal phase, and prevents the pressure-induced phase transition.

It should be noted that the pressure-induced phase transition did not occur under the hydrostatic compression (heterogeneous pressure) up to 2 GPa as had been pointed out by Miyaji.[18] Therefore, some of the shear components of the stress tensor may contribute to the occurrence of the phase transition.

There is a fact that the o-POM phase generated by the pressure-induced phase transition does not transform to t-POM on heating at 69°C, i.e., the transition temperature of the as-polymerized o-POM samples, and the transformation does occur on heating above 100°C. This suggests that the existence of the residual stress in the compressed solid prevents the o→t phase transition.

Thus, behaviors of the thermal and pressure-induced phase transitions of POM are influenced to a great extent by the residual stress present in the mechanically processed solid samples.

5.3.2. Infrared Spectral Feature of the Generated Orthorhombic Phase

The B_1 modes are active in both infrared and Raman spectra, having transition dipole moments parallel to the chain axis (the c axis). The B_2-B_3 pairs of spectral bands correspond to the Davydov split pairs due to the intermolecular interactions between two molecules in the unit cell. They have the transition dipole moments perpendicular to the chain axis (see **Chapter 3**).

Fig. 5.4 shows infrared spectral changes for the 10th B_2-B_3 split pair of o-POM, which corresponds to the 10th E_1 mode at 457 cm^{-1} of t-POM, during the t→o pressure-induced phase transition and the successive thermal o→t transition measured on the FCC and ECC samples of starting t-POM. In both cases, the B_2-B_3 split pair appears at the same frequencies (at 439 and 433 cm^{-1}) but relative intensity of the split components differs between the two samples.

Fig. 5.5 shows the far-infrared spectral changes during the same procedure for the 10th B_1 band of o-POM, which corresponds
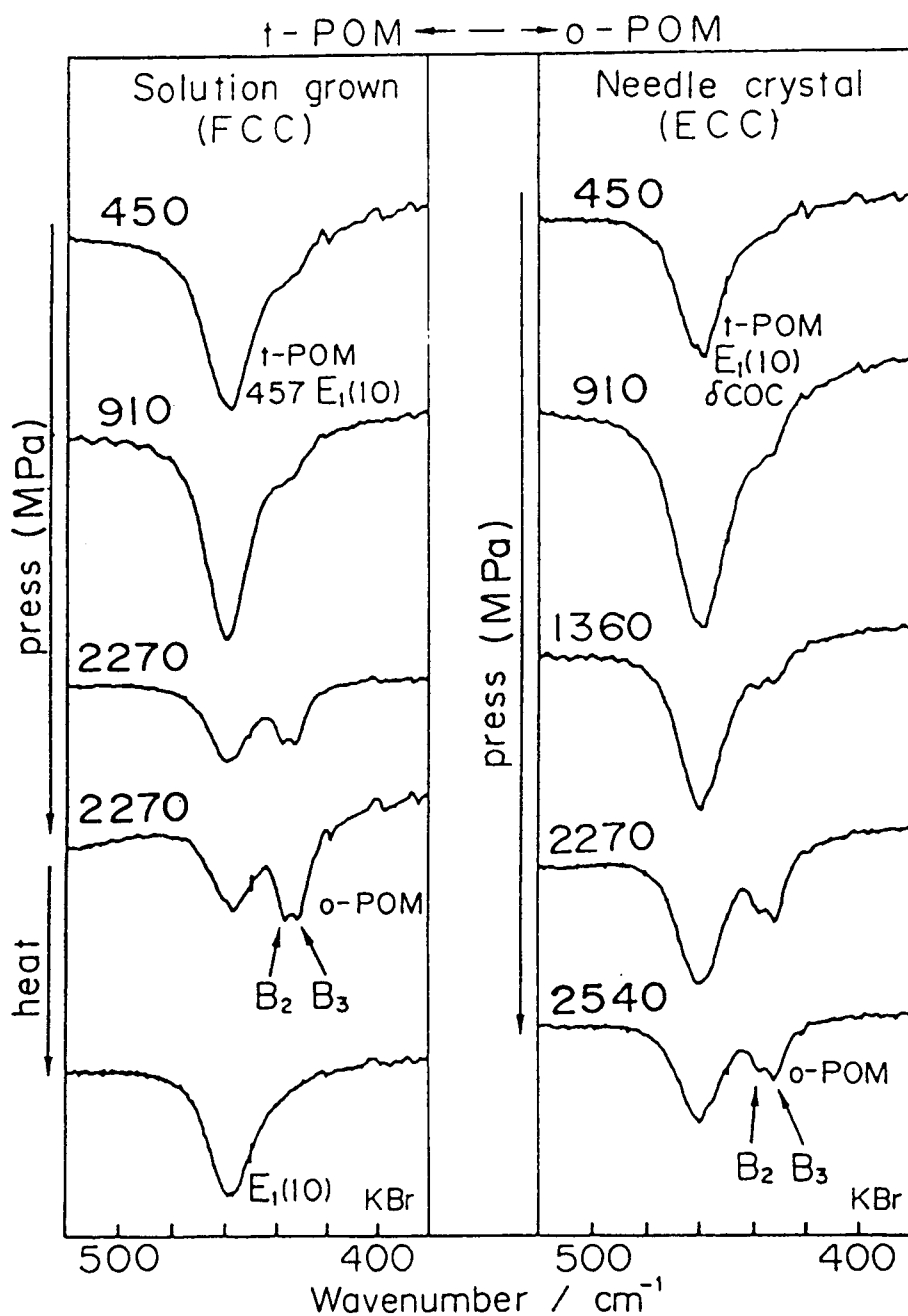
Fig. 5.4. Infrared spectral changes of the $E_1(10)$ of the trigonal phase and $B_2(10)-B_3(10)$ of the orthorhombic phase of POM on the pressure-induced phase transition from the trigonal to the orthorhombic phase. Starting from the ECC (right) and FCC (left) samples of the trigonal phase. The numbers indicate the applied pressure.

Fig. 5.5. Far infrared spectral changes of the torsional mode
[A$_2$(5) of the trigonal phase and B$_1$(10) of the orthorhombic
phase] on the pressure-induced phase transition of POM from the
trigonal to the orthorhombic phase, starting from the ECC (right)
and FCC (left) samples of the trigonal phase. The numbers
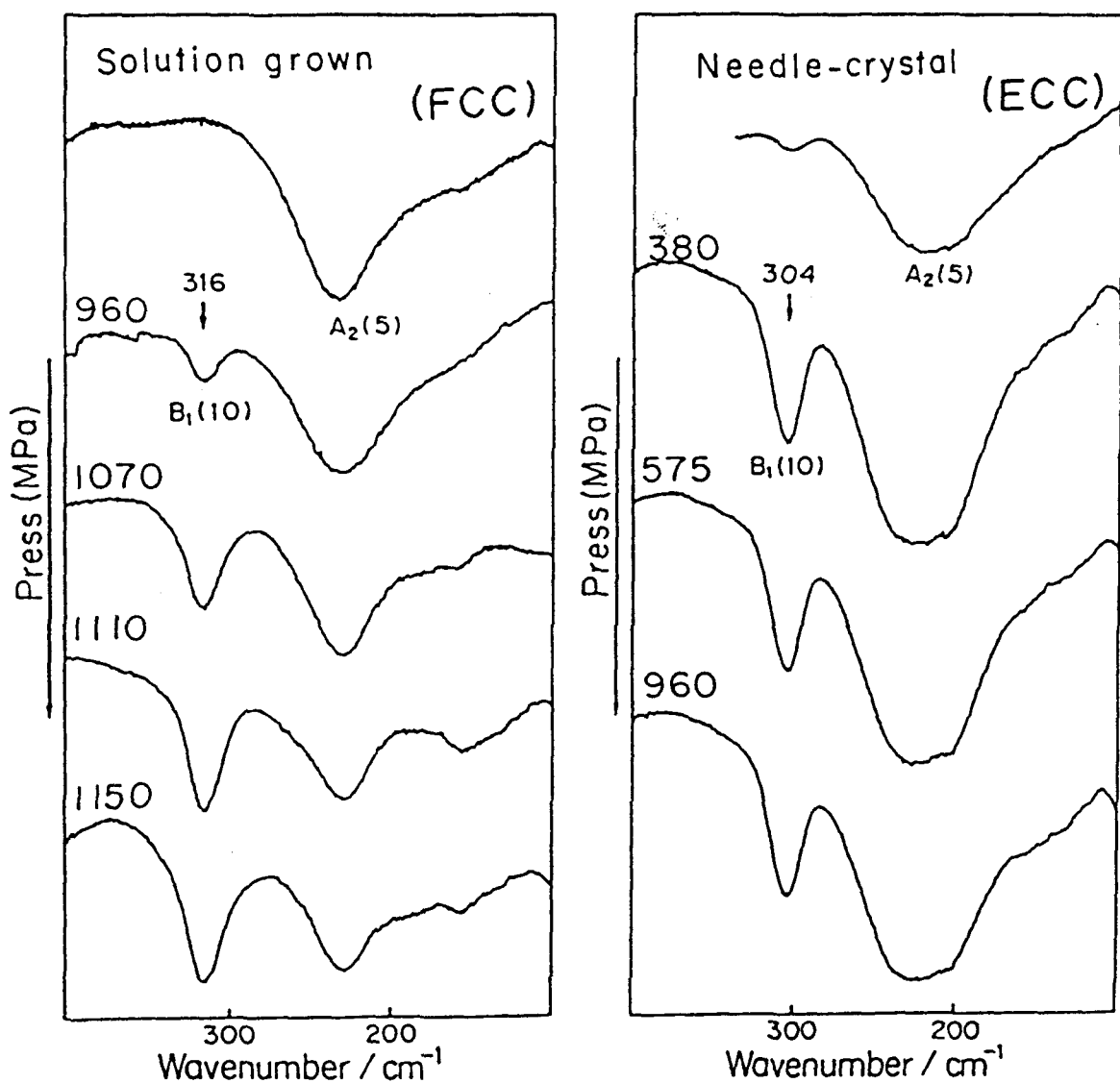indicate the applied pressure.

to the 5th A_2 band of t-POM. Contrary to the case of the 10th

B_2-B_3 pair, the $B_1(10)$ mode (marked with arrows) of o-POM

generated from the solution-grown FCC t-POM sample appears at 316

cm^{-1}, while the same mode of o-POM generated from the needle-like

ECC t-POM sample appears at 304 cm^{-1}. The latter frequency is

very close to that of the particle sample consisting of rod-like

single crystals (a typical ECC sample) of o-POM (at 297 cm^{-1},

Fig. 4.6).[10] The discrepancy between 297 and 304 cm^{-1} may be

caused by a little distortion of the perfect ECC structure during

the compression. The 316 cm^{-1} band (at room temperature) of the

o-POM sample generated from the FCC starting sample can be

recognized as the $B_1(10)$ mode frequency of the FCC sample of o-

POM, while the 304 cm^{-1} band as that of the ECC sample. This is

the same tendency as the case of t-POM, where the $A_2(5)$ mode

appears at 236 cm^{-1} in the FCC sample, while it appears at 220

cm^{-1} in the ECC sample.[15]

For-infrared spectra of the compressed ones were measured

also at liquid N_2 temperature (upper spectra of Fig. 5.6) in

order to confirm the difference in the $B_1(10)$ mode frequency

between FCC and ECC. The same magnitude of the frequency gap (12

cm^{-1}) of the $B_1(10)$ mode between ECC and FCC was obtained in the

both samples, although the $B_1(10)$ mode frequencies themselves are

blue-shifted with lowering temperature.

For other absorption bands of o-POM in the mid-infrared

region, the similar comparison was performed by using the

subtraction technique in order to remove the interference by

strong absorptions associated with the remaining t-POM. The

infrared spectrum corresponding to that of pure o-POM generated

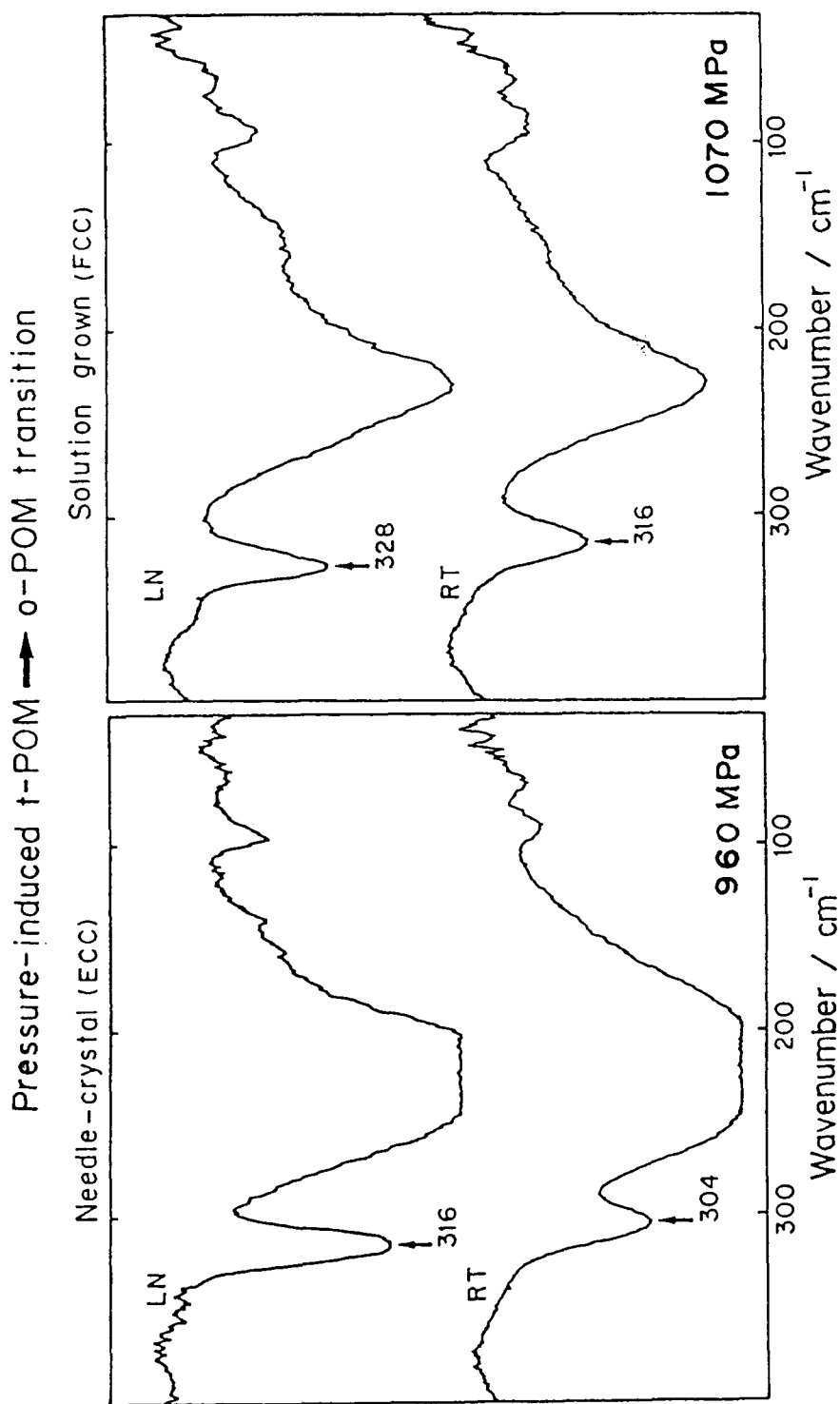from a particular starting t-POM sample was obtained by the

Pressure-induced t-POM → o-POM transition

Needle-crystal (ECC)   Solution grown (FCC)

960 MPa   1070 MPa

Wavenumber / cm^{-1} Wavenumber / cm^{-1}

Fig. 5.6. Far infrared spectra in the region of torsional modes, A$_2$(5) belonging to t-POM and B$_1$(10) belonging to o-POM, for the ECC (left) and FCC (right) samples measured at room temperature and liquid N$_2$ temperature. The bands indicated by the arrows are due to the B$_1$(10) of o-POM.
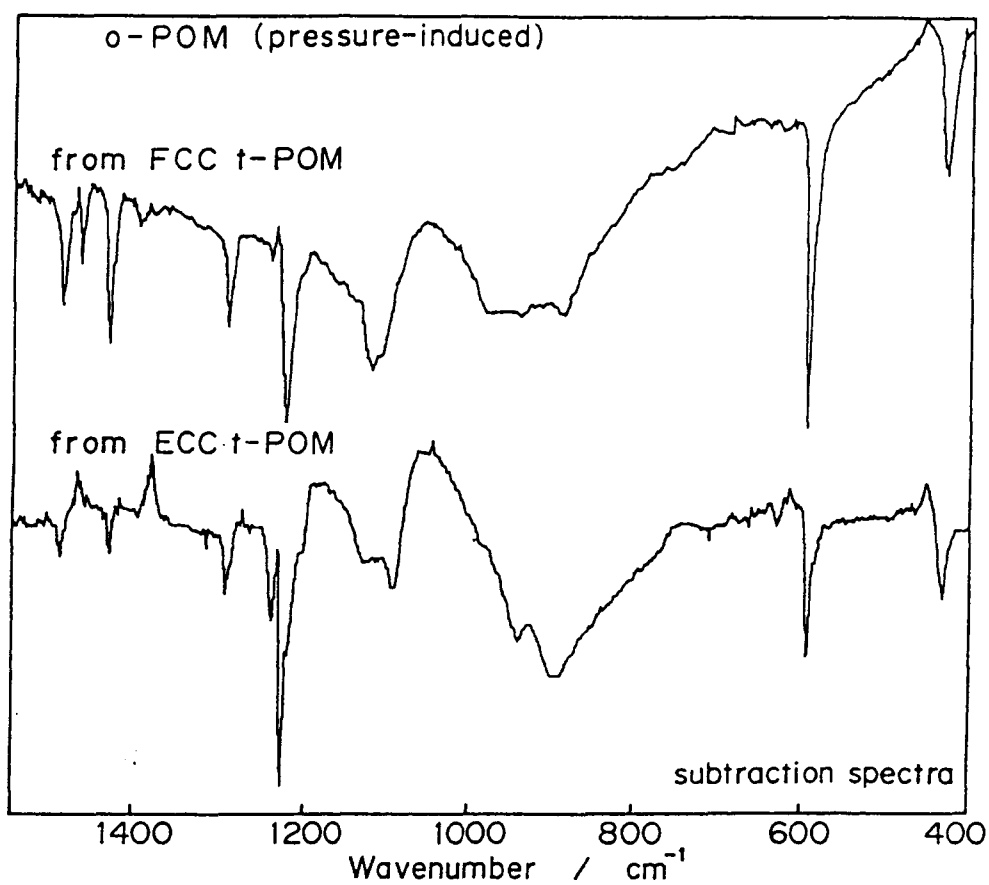
Fig. 5.7. Infrared spectra of o-POM generated by the pressure-induced phase transition from the FCC (upper) and ECC (bottom) samples of t-POM. The spectra are obtained by the subtraction technique.

following procedure. The spectrum of a compressed sample was recorded and memorized first (spectrum A); then the sample was heated at 100°C for an hour or more in order to convert the generated orthorhombic phase to the trigonal phase, and its spectrum was recorded (spectrum B). The subtraction A - B gave the spectrum for the pure o-POM generated by the pressure-induced transition. Fig. 5.7 shows the subtraction spectra of o-POM generated from the ECC and FCC samples of t-POM in the region of 1500-400 cm^{-1}. At a glance, these infrared spectra were remarkably different from each other in the 1150~800 cm^{-1} region, and the $B_2(6)$ (~1220 cm^{-1}), and $B_2(9)$ modes (~595 cm^{-1}).

In order to obtain more convincing information about the morphology-dependent IR spectral change, we measured the subtraction spectra using an FT-IR instrument. Fig. 5.8 shows the subtraction spectra of o-POM generated from the ECC and FCC t-POM samples.   The $B_1(6)$ and $B_1(8)$ bands of o-POM generated from the FCC sample exhibit a remarkable high-frequency shift (by 25 cm^{-1} and 92 cm^{-1}, respectively) compared with the corresponding bands of o-POM generated from the ECC sample, whereas the B_2 and B_3 modes appear at the same frequencies in both o-POM samples. The frequencies of the infrared-active modes of o-POM measured on the ECC and FCC samples were summarized in Table 5.1. Specific frequency shifts caused by the difference in morphological structure of o-POM were found only for the B_1 bands having the transition dipole moments parallel to the chain axis. The perpendicular B_2 and B_3 bands as well as the infrared-inactive Raman bands due to the A species appear at the same frequencies in the ECC and FCC samples (see Fig. 5.2).

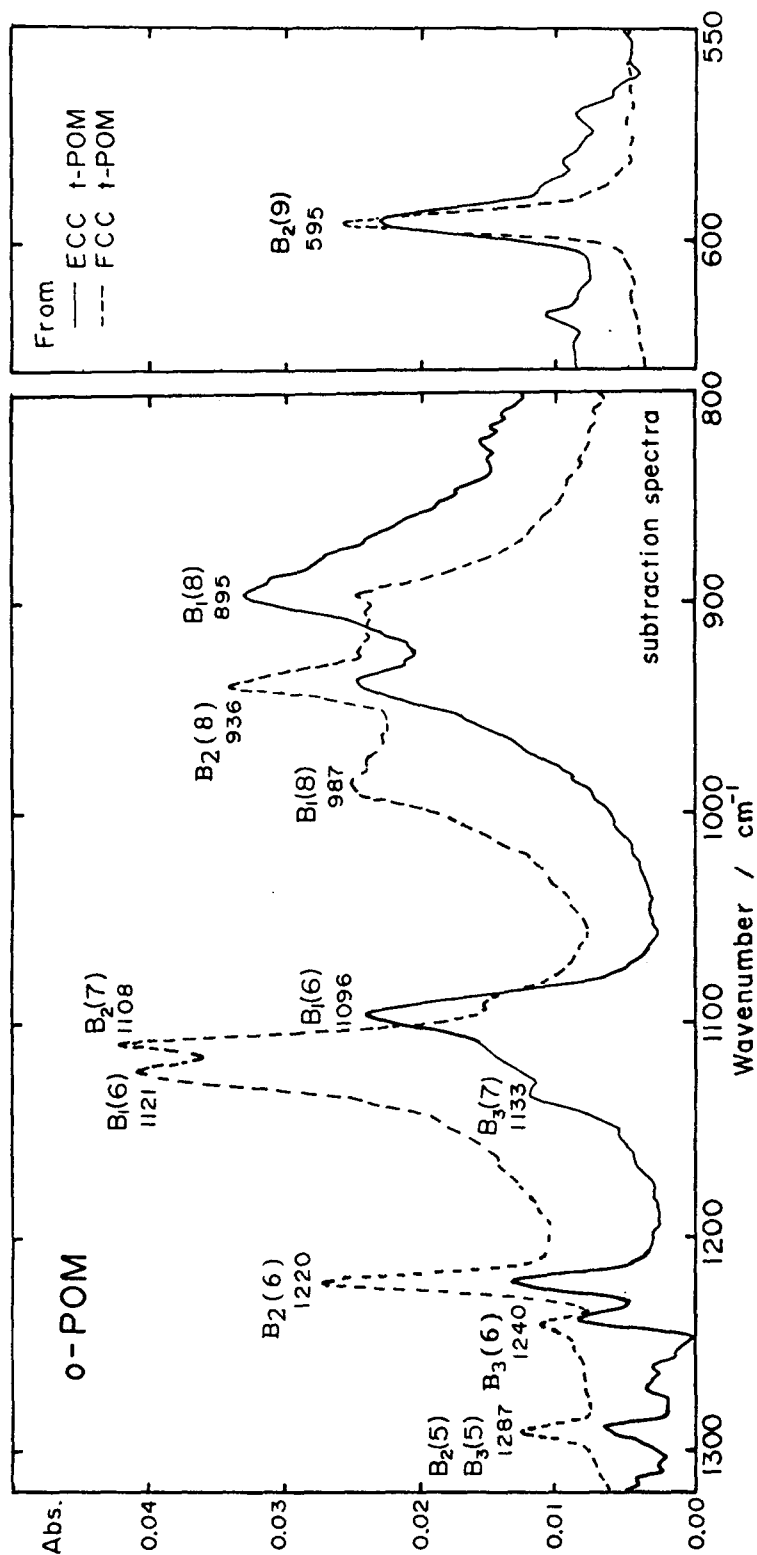As for the $B_2(6)$-$B_3(6)$ split pair of the FCC sample, the B_2

Fig. 5.8. Fourier transform infrared spectra of pure orthorhombic poly(oxymethylene) generated by the pressure-induced phase transition from the ECC (the solid line) and FCC (the broken line) samples of the trigonal phase. The spectra are obtained by the subtraction technique.

Table 5.1 Frequencies of the optical active zone-center modes observed for ECC and FCC samples of orthorhombic poly(oxymethylene) (cm^{-1})

modes	ECC[a]	FCC[b]	$\Delta\nu$[c]
$B_2(5)+B_2(5)$	1287 m	1287 m	0
$B_3(6)$	1240 m	1240 m	0
$B_2(6)$	1220 s	1220 s	0
$B_3(7)$	1133 s	*int.*	
$B_2(7)$	*int.*	1108 vvs	
$B_1(6)$	1096 vvs	1121 vvs	25
$B_1(8)$	895 vvs	987 vvs	92
$B_2(8)$	936 vvs	936 vvs	0
$A(8)$[d]	909	909	0
$B_2(9)+B_3(9)$	595 vs	595 vs	0
$B_2(10)$	439 m	439 m	0
$B_3(10)$	433 m	433 m	0
$B_1(10)$	304 m	316 m	12

[a] Rod-like single crystals obtained as a by-product of a cationic polymerization of trioxane.

[b] Obtained from the ECC sample of trigonal poly(oxymethylene) through pressure-induced phase transition.

[c] Frequency gap: ν(FCC) - ν(ECC).

[d] Raman data.

int.: Interferred by a strong B_1 band.

component is more sensely than the B_3 component, indicating that the o-POM crystallites generated from powder samples of FCC t-POM take a preferential orientation. On reference to the infrared spectra measured on plane-oriented moth-shaped single crystals and powder sample of o-POM (Fig. 2.20), the relative intensity of the B_2-B_3 split pair of the compressed sample is rather close to that of the plane-oriented moth-shaped single crystals, suggesting that the *a* axis of the resultant o-POM crystallites orients preferably along the direction of the compression. This fact shows that some of the stress tensor components (presumably, the shear component), other than the hydrostatic pressure take part in the occurrence of the pressure-induced phase transition.

From these experimental results, we are able to deduce the following conclusions: (1) the ECC or FCC morphology of the starting t-POM is retained during the pressure-induced phase transition, (2) the specific morphology dependent infrared spectral change found first in t-POM is observed also in o-POM, (3) some of the stress tensor components, other than the hydrostatic pressure, contribute to the occurrence of this phase transition.

REFERENCES

1. J. E. Preedy and E. J. Wheeler, Nature Phys. Sci., **236**, 30 (1972)
2. H. Miyaji and K. Asai, J. Phys. Soc. Jpn., **36**, 1497 (1974)
3. M. Iguchi, Brit. Polym. J., **5**, 195 (1973)
4. M. Iguchi and I. Murase, J. Crystal Growth, **24/25**, 596 (1974)
5. M. Iguchi, I. Murase and K. Watanabe, Br. Polym. J.,

6. M. Iguchi, H. Kanetsuna and T. Kawai, Makromol. Chem., **128**, 63 (1969)

7. M. Kobayashi, H. Morishita, M. Shimomura and M. Iguchi, Macromolecules, **20**, 2453 (1987)

8. Morishita, M. Kobayashi, M. Shimomura, M. Iguchi and H. Kuwahara, Sci. Bull. Fac. Educ., Nagasaki Univ., **41**, 1 (1989)

9. M. Kobayashi, Y. Itoh, H. Tadokoro, M. Shimomura and M. Iguchi, Polym. Commun., **24**, 38 (1983)

10. M. Kobayashi, H. Morishita, T. Ishioka M. Iguchi, M. Shimomura and T. Ikeda, J. Mol. Struct., **146**, 155 (1986)

11. H. Morishita and M. Kobayashi, Rep. Prog. Polym. Phys. Jpn., **30**,131 (1987)

12. D. C. Basset, F. R. Dammont and R. Salovey, Polymer, **5**, 579 (1964)

13. D. R. Carter and E. J. Baer, J. Appl. Phys., **37**, 4060 (1966)

14. M. Shimomura and M. Iguchi, Polymer, **23**, 509 (1982)

15. M. Shimomura, M. Iguchi and M. Kobayashi, Polymer, **29**, 351 (1987)

16. M. Shimomura, Y. Tanabe, Y. Watanabe and M. Kobayashi, Polymer, **31**, 1411 (1990)

17. M. Shimomura, M. Iguchi and M. Kobayashi, Polymer, **31**, 1406 (1990)

18. H. Miyaji, J. Phys. Soc. Jpn., **39**, 1346 (1975)

Chapter 6.

Summary and Concluding Remarks

     This thesis has dealt with the following subjects: (1) Full

vibrational assignments of o-POM and t-POM fundamentals based on

IR and Raman polarization data measured on micron-size single

crystals with the aid of normal modes calculation, and (2)

clarification of the role of crystal morphology in the solid-

state phase transitions of POM: The thermal phase transition from

o-POM to t-POM and the pressure-induced phase transition from t-

POM to o-POM.

     The main results and conclusions obtained are summarized

below.

Chapter 2. Structure and Vibrational Spectra of Single Crystals
of Orthorhombic Poly(oxymethylene)

     Polarized Raman spectra of metastable orthorhombic

polyoxymethylene (o-POM) were obtained for the first time by

using the Raman microprobe technique on micron-size o-POM single

crystals. Based on these polarization data, the symmetry species

of the Raman bands were determined. In measuring the three-

dimensional Raman polarization, the polarization scrambling

occurring in the microprobe technique played an important role.

This is caused by sharp condensation of the incident laser beam

at the focal point in the sample through an object lens with high

magnification (or short focal length) and also by wide-angle

collection of the scattered light with the same object lens. The scrambling effect was investigated in detail by the analysis of the changes in the intensity ratio of the doublets due to the B_2-B_3 Davydov split pairs by varying the optical conditions such as the magnification of the objective and the apperture size in the optical path.

Polarized infrared spectra of o-POM single crystals were also obtained using the micro-infrared technique. The polarized infrared and Raman data of the o-POM lattice were obtained also from the study of a single crystal of orthorhombic modification of deca(oxymethylene)diacetate that is a linear oligomer of POM possessing in the o-POM sublattice structure.

Using these spectral data, we performed full vibrational assignments of o-POM with the aids of the normal modes calculation. At the same time, we determined the orientation of the crystallographic axes in the moth-shaped o-POM single crystal.

Chapter 3.   Vibrational Spectroscopic Study on Trigonal
             Poly(oxymethylene) Consisting of the Extended
             Chain Morphology

Moth-shaped t-POM single crystals were obtained by thermal phase transition of o-POM single crystals having the same crystal habits. The obtained t-POM crystals were found to have a typical ECC morphology. Their polarized Raman spectra were obtained for the first time by means of the microprobe technique. The symmetry species of the Raman bands were decided on the basis of the observed polarizations.

Ordinary right-angle polarized Raman spectra of t-POM were

measured on pressurized superdrawn filaments having high transparency and ECC-type crystal morphology. Assignments of the Raman-active modes including the E_2 vibrations, which mostly remain unassigned so far, were performed. Spectra of deuterated t-POM of an ECC crystal morphology were obtained and analyzed also.

The $E_1(7)$ and $E_1(8)$ modes were found to exhibit the LO-TO splitting characteristic of non-centrosymmetric crystal lattice. The angular dispersion of the LO component for these modes was also observed. This fact suggested that one t-POM crystallite should be chiral consisting only of right- or left-handed helical molecules, although equal amounts of the two types of crystallites are racemized each other in the whole sample.

Chapter 4. Vibrational Spectroscopic Study on the Solid-State Phase Transition of Poly(oxymethylene) Single Crystals from the Orthorhombic to the Trigonal Phase

Behavior of the thermal phase transition from o-POM to t-POM (o→t transition) were investigated on micron-size single crystals of POM by means of DSC and vibrational spectroscopy.

Polarized microscope observation showed that the crystal habit, the crystal shape and the appearance of parallel striations on the crystal face of the starting o-POM single crystals remained unchanged throughout the o→t thermal phase transition. The resultant t-POM crystals showed clear birefringence characteristic of a single crystal form. Thus, we could obtain the moth-shaped t-POM single-crystal having the size and the optical clearness suitable for the polarized micro-Raman measurement.

The polarized micro-Raman spectra taken on the t-POM single crystals demonstrated that the direction of the crystallographic c axis remained unchanged through the thermal phase transition.

The resultant t-POM crystals were proved to have the ECC morphology from the following facts that (1) the A_2 bands, whose frequencies were known to shift remarkably with variation in crystal morphology, appeared at the same positions as those of the needle-like single crystals (a typical ECC sample), and (2) the resultant t-POM crystals melted around 190°C, more than 10°C higher than the commercial t-POM resin.

The DSC thermogram showed that the phase transition took place at 69°C on heating with an endotherm of $\Delta H = 0.6$ kJ/mol per CH_2O unit. Therefore, the thermodynamic stability of the trigonal phase at ambient is not responsible for the enthalpy, but for the entropy attributed to rotational fluctuation of the molecules around the chain axes. Occurrence of the molecular motion was suggested by sharp smearing of the far-infrared 101 cm^{-1} band due to the rotatory lattice mode on heating process from liquid N_2 temperature to room temperature.

We concluded that o-POM single crystals transformed to t-POM keeping the crystal habit and the molecular chain orientation as well as the crystal morphology (ECC) unaltered during the phase transition.

Chapter 5.   Pressure-Induced Phase Transition of
             Poly(oxymethylene) from the Trigonal to the
             Orthorhombic Phase:
             Effect of Morphological Structure

Using t-POM crystals typical of both the FCC and ECC

morphologies as the starting materials, we investigated pressure-induced phase transition from t-POM to o-POM by means of the infrared and Raman spectroscopies.

Content of the generated o-POM phase increased with increasing pressure applied during uniaxial compression. Trigonal POM of the FCC type transformed more easily to the o-POM phase than t-POM of the ECC. When the compressed samples of t-POM (both FCC and ECC) were heated at about 100°C for more than an hour, the generated o-POM phase disappeared completely (the thermal phase transition of the reverse direction), giving rise to infrared spectra very close to those of the uncompressed t-POM samples.

Infrared parallel bands due to the $B_1(6)$, $B_1(8)$ and $B_1(10)$ modes of o-POM generated from an FCC t-POM sample appeared at significantly high frequencies compared with the corresponding bands of o-POM generated from the ECC t-POM sample. Thus, in case of o-POM, remarkable frequency shifts due to the difference in crystal morphology were observed for the infrared-active B_1 bands having the transition dipole moments parallel to the chain axis. This behavior is similar to the case of the A_2 modes of t-POM. The FCC and ECC morphologies of the starting t-POM single crystals were confirmed to remain unchanged during the pressure-induced phase transition.

The intensity ratio of the infrared B_2-B_3 Davydov split components of o-POM generated by compressing a KBr pellet of the starting t-POM differ from that of the unoriented powder sample of as-polymerized o-POM. This suggests that the shearing elements of the applied stress tensor, rather than the hydrostatic pressure, induce the pressure-induced phase

transition.

Throughout the present work, use of highly ordered single crystals made a contribution for solving important problems concerning the vibrational spectroscopy and phase transition of the POM crystals. In this respect, the preparation of such samples was the indispensable first step of this work. In Appendix 1, we will thus describe the generation of rod-like single crystals of t-POM having a new habit.

Use of the Raman microprobe technique makes the polarization measurement possible for micron-size single crystals of the polymer as well as for micron-sized limited domains of bulk samples. This new technique opens a new field of space-resolved spectroscopy, which is applicable to the study of other complicated micro-structures of polymers and long-chain compounds. As an example of this type of application, micro-characterization of microdomain structures on Orth Ⅱ/Mon overgrowth crystals of stearic acid B form is investigated in Appendix 2. There, we deal with thermodynamic stability among polymorphs and polytypes of stearic acid, and propose the phase diagram for the modifications. In the course of this work we found a new technique for the micro-characterization of stacking disorder of molecular layers. We also successfully established with the polarization scrambling effect in the Raman microprobe technique. We will introduce some examples as application of the Raman microprobe technique in this appendix.

List of publications

The contents of this thesis have been or will be published in the following papers.

1. Vibrational Spectroscopic Study on Polymorphism and Molecular Aggregation States in Polyoxymethylene.

   M. Kobayashi, H. Morishita, T. Ishioka, M. Iguchi, M. Shimomura and T. Ikeda, J. Mol. Struct., <u>146</u>, 155 (1986)

2. Vibrational Spectroscopic Study on the Solid-state Phase Transition of Poly(oxymethylene) Single Crystals from the Orthorhombic to the Trigonal Phase.

   M. Kobayashi, H. Morishita, M. Shimomura and M. Iguchi, Macromolecules, <u>20</u>, 2453 (1987)

3. Polarized Raman Spectra of Trigonal Polyoxymethylene.

   H. Morishita, M. Kobayashi and T. Komatsu, Rep. Progr. Polym. Phys., Jpn., <u>30</u>, 131 (1987)

4. Vibrational Spectroscopic Study on the Orientation of Orthorhombic Polyoxymethylene Single Crystal.

   H. Morishita and M. Kobayashi, Rep. Progr. Polym. Phys., Jpn., <u>30</u>, 139 (1987)

5. Vibrational Spectroscopic Study of Orthorhombic Polyoxymethylene.

   H. Morishita, M. Kobayashi, M. Shimomura and M. Iguch, Sci. Bull. Fac. Educ., Nagasaki Univ., No.23, 47 (1988)

6. Pressure-induced Phase Transition of Poly(oxymethylene) from the Trigonal to the Orthorhombic Phase: Effect of Morphological Structure.

   M. Kobayashi, H. Morishita and M. Shimomura, Rep. Progr. Polym. Phys., Jpn., <u>31</u>, 473 (1988)

7. Vibrational Spectroscopic Study on Trigonal Polyoxymethylene Consisting of the Extended Molecular Chains.
   Sci. Bull. Fac. Educ., Nagasaki Univ., No.40, 41 (1989)

8. Pressure-induced Phase Transition of Poly(oxymethylene) from the Trigonal to the Orthorhombic Phase: Effect of Morphological Structure.
   M. Kobayashi and H. Morishita, Macromolecules, 22, 3726 (1989)

9. Vibrational Spectroscopic Study on the Solid-State Phase Transition of Polyoxymethylene I.On the Phase Transition from the Orthorhombic to the Trigonal System.
   H. Morishita, M. Kobayashi, M. Shimomura, M. Iguchi and H. Kuwahara, Sci. Bull. Fac. Educ., Nagasaki Univ., No.41, 1 (1989)

10. On the Morphology of Rod-like Trigonal Polyoxymethylene Single Crystal.
    H. Morishita, M. Kobayashi, H. Kuwahara, M. Shimomura and M. Iguch, Sci. Bull. Fac. Educ., Nagasaki Univ., No.41, 13 (1989)

11. Vibrational Spectroscopic Study on the Solid-State Phase Transition of Polyoxymethylene II.Pressure-induced Phase Transition of Polyoxymethylene from the Trigonal to the Orthorhombic Form.
    H. Morishita and M. Kobayashi, Sci. Bull. Fac. Educ., Nagasaki Univ., No.44, 23 (1991)

12. Polarized Raman and Infrared Studies of Single Crystals of Orthorhombic Modification of Polyoxymethylene and Its Linear Oligomer: Crystal Structures and Vibrational Assignments.
    M. Kobayashi, T. Adachi, Y. Matsumoto, H. Morishita,

T. Takahashi, K. Ute and K. Hatada, J. Raman. Spectrosc., <u>24</u>, 533 (1993)

13. Vibrational Spectroscopic Study on Trigonal Poly(oxymethylene) Consisting of the Extended Chain Morphology.

H. Morishita and M. Kobayashi, Macromolecules, to be published.

Related papers

1. The vibrational Spectra and Structures of $H_3C-X-CH_3$ (X=O, CH_2, NH).

K. Hamada and H. Morishita, Z. Phys. Chem., <u>97</u>, 295 (1975)

2. The Proton NMR Spectra of CH_3-X-H (X=O, S, Se, Te).

K. Hamada and H. Morishita, Jpn. J. Appl. Phys., <u>15</u>, 748 (1976)

3. The Synthesis and the Raman and Infrared Spectra of Methyltellurol.

K. Hamada and H. Morishita, Syn. React. Inorg. Metal-Org. Chem., <u>7</u>, 355 (1977)

4. The Raman, Infrared and Proton NMR Spectra and Structures of Dimethyl Chalcogenides.

K. Hamada and H. Morishita, J. Mol. Struct., <u>44</u>, 119 (1978)

5. The Synthesis of Diethyl Ditelluride and the Raman and Infrared Spectra and Structures of Diethyl Dichalcogenides.

K. Hamada and H. Morishita, Synth. React. Inorg. Metal-Org. Chem., <u>11</u>, 597 (1981)

6. Raman, Infrared and H-NMR Spectra of Hexamethyldisiloxane and Hexamethyldisilazane.

K. Hamada and H. Morishita, Spectrosc. Letters, <u>16</u>, 717

(1983)

7. Raman, Infrared and H-NMR Spectra of
   Hexamethyldisilylchalcogenides.
   K. Hamada and H. Morishita, Spectrosc. Letters, <u>19</u>, 815
   (1986)

8. Study of Micropolytype Structures in Crystals of Stearic Acid
   B Form by the Raman Microprobe Technique.
   H. Morishita, T. Ishioka, M. Kobayashi and K. Sato, J. Phys.
   Chem., <u>91</u>, 2273 (1988)

9. Stability, Occurrence and Step Morphology of Polymorphs and
   Polytypes of Stearic Acid I.Stability and Occurrence.
   K. Sato, M. Kobayashi and H. Morishita, J. Cryst. Growth, <u>87</u>,
   236 (1988)

10. Micro-Raman Spectra on Orth II/Mon Overgrowth Crystals of
    Stearic Acid B Form.
    H. Morishita, M. Kobayashi, K. Sato, F. Kaneko and Y. Furuya,
    Sci. Bull. Fac. Educ., Nagasaki Univ., No.43, 19 (1990)

Generation of New Habit of t-POM Single Crystals

1. Introduction

As described in Chapter 1, various crystal habits of t-POM single crystals were obtained so far. Recently, we prepared single crystals of t-POM having a new habit. In this appendix, preparation and characterization of thus obtained single crystals are dealt with.

2. Preparation of Rod-like Single Crystals of t-POM

Single crystals having new habit[1] were generated through a heterogeneous cationic polymerization of trioxane, which produced the crystalline particle sample of o-POM[2] (refer to Chapter 2). Trioxane was prepared by heating formaldehyde, which was generated from paraformaldehyde and water in the presence of silicotungstic acid as catalyst.[3] Trioxane dissolved in cyclohexane was refluxed at 100°C for one day under the presence of metallic sodium in an atomosphere of dehydrated Ar. Thereafter, the solution was separated from solid materials by distillation. Immediately after adding boron trifluoride ether complex the solution was shaken vigorously. Subsequently, extremely small quantity of water (rather moisture) was added and the solution was shaken again vigorously. The solution was set in an oven kept at 55°C for 3 days to proceed the polymerization of trioxane. Finally, the polymerization reaction was terminated by adding triethylamine.

A thin film of t-POM was formed on the wall of the reaction vessel, and a number of small particles of ~2 mm diameter were formed on the film surface contacted with liquid and gaseous phases (Fig.1A). The particles consisted of a number of transparent rod-like crystals of POM (Figs.2A and 3A). These crystals show optical birefringence under crossed nicols and have a fine edge characteristic of single crystals and give the IR spectrum characteristic of the trigonal form (Fig.4A).

The crystal habit, shape and appearance of the t-POM single crystals thus generated are similar to those of the particle crystals of o-POM. The particle crystals of o-POM were produced when the polymerization reaction was carried out at 50°C. On the other hand t-POM particles were produced at 55°C as described above. This fact suggests that thermodynamic stability of the t-POM phase is still more stable than that of the o-POM phase in
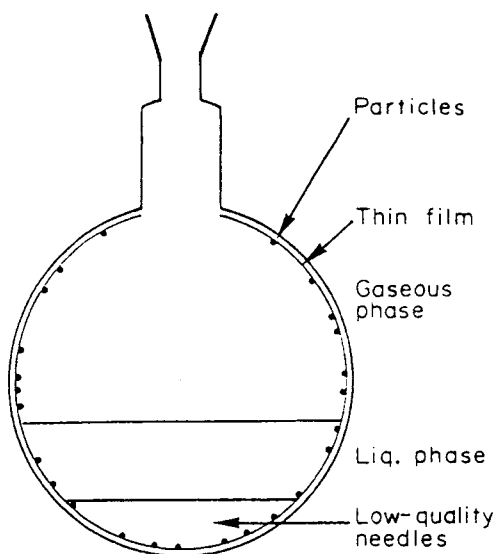
Fig.1A. Schematic illustration of t-POM formed in the reaction vessel.
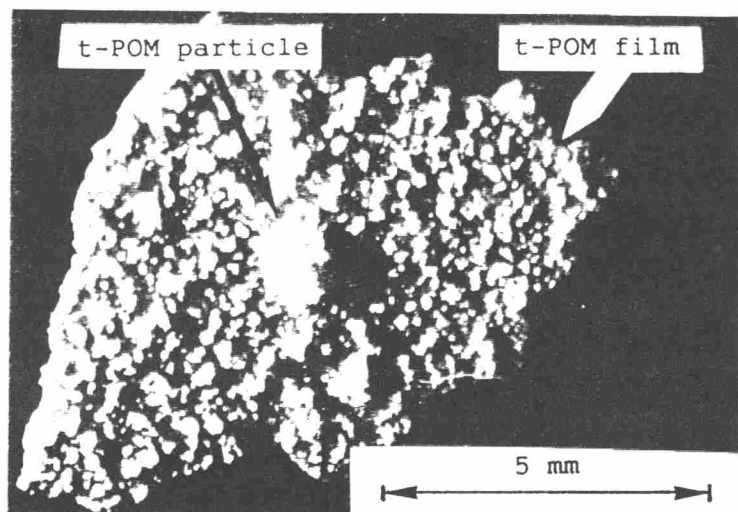
Fig.2A. Macro-photograph of t-POM particles formed on t-POM film.
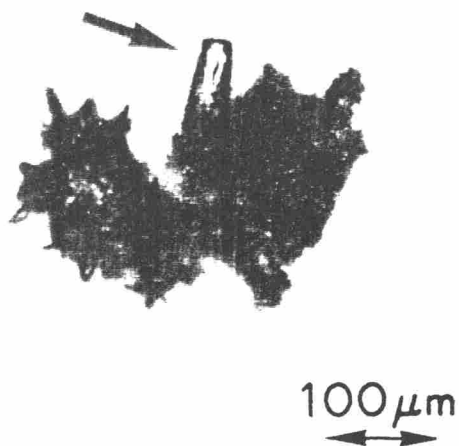
Fig.3A. An optical micro-photograph of t-POM particles consisting of rod-like single crystals.
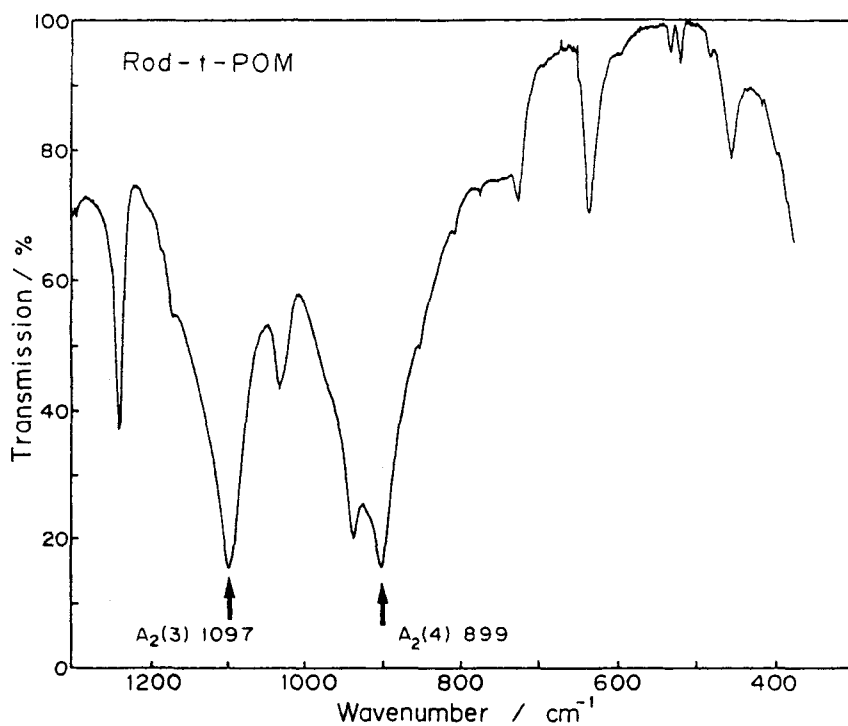
Fig.4A. Infrared spectrum of the single crystals of t-POM measured by Nujol mull method. The A₂ bands marked with an arrows.
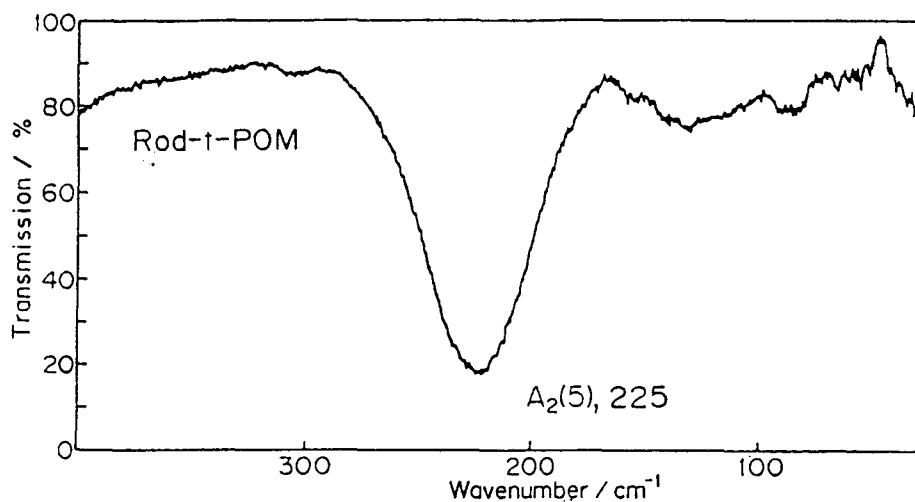

Fig.5A. Far-infrared spectrum of the single crystals of t-POM measured by Nujol mull method.

the higher-temperature range below the thermal phase transition temperature (at 69°C) of o $\rightarrow$ t-POM.

3. Infrared Spectra of Rod-like Single Crystals of t-POM

The $A_2(3)$ and the $A_2(4)$ IR bands appear at 1097 and 899 cm^{-1} (Fig.4A), respectively, indicating that the crystal has the ECC-type morphology (refer to Chapter 3). The far-infrared spectrum is shown in Fig.5A. The $A_2(5)$ mode appears at 225 cm^{-1}. The frequency is slightly higher than that (at 220 cm^{-1}) of the typical ECC of t-POM.[4,5] The single crystal melts around 190°C, corresponding to melting point of the typical ECC of t-POM, more than 10°C higher than the FCC t-POM. Thus, we concluded that the single crystals of t-POM obtained were of the ECC-type morphology.

REFERENCES

1. H. Morishita, M. Kobayashi, H. Kuwahara, M. Shimomura and M. Iguchi, Sci. Bull. Fac. Educ., Nagasaki Univ., No. 41, 13 (1989)

2. M. Iguchi, Polymer, 24, 915 (1983)

3. K. Yoshida, T. Iwasako and J. Shyoutomo, JP (A), 56/118079 (1981)

4. M. Shimomura and M. Iguchi, Polymer, 23, 509 (1982)

5. M. Shimomura and M. Iguchi and M. Kobayashi, Polymer, 29, 351 (1988)

Application of Raman Microprobe as a New Technique for

Characterization of Microdomain Structures

1. Introduction

In crystalline solids of organic long-chain compounds

forming lamellar structures there is a higher-order structural

variation that originates from the difference in the stacking

mode of monomolecular or bimolecular layers. This is called

"polytypism" in distinction from "polymorphism" which is

concerned with the structural difference within one molecular

layer. This was first noted more than three decades ago by an

optical microscopic observation of step patterns on the as-grown

crystal surface.[1] For some monoclinic modifications of n-

alkanes [the (011) type monoclinic form] and n-fatty acids (the B

form), also, two basic polytypes, i.e., the single-layered

monoclinic (abbreviated as Mon) and the double-layered

orthorhombic (Orth II) polytypes were found to be obtained as

well-grown single crystals. Mon corresponds to the ordinary

monoclinic form where all the molecular layers stack in the same

sense and one layer construct the crystallographic repeating

unit. The crystal structures of n-hexatriacontane, $n-C_{36}H_{74}$,[2]

and stearic acid, $C_{17}H_{35}COOH$, B form[3] belonging to this polytype

were determined by the X-ray diffraction method. In Orth II, the

orientation of molecular layers changes alternately by 180°

rotation about the axis normal to the layer surface, forming a

double-layered unit cell. This structure has been confirmed by the X-ray[4-6] and vibrational spectroscopic methods[5-7] for n-alkanes and the stearic acid B form. Fig.1B (a) illustrates the crystal structures along with space group symmetry elements of the Mon[3] and Orth II[6] polytypes of the stearic acid B form. In Fig.1B (b) the schematic representation of the chain orientation in the polytype is given. In (a), the *a* and *b* axes in Mon defined in ref.3 are interchanged with each other for the sake of convenience. In (b) the oblique lines represent molecular or dimer chains inclined to the lamellar surface.

Through a series of vibrational spectroscopic investigation on polytypism in long-chain compounds, Kobayashi *et al.* have revealed that polytype structures of the compounds are identified definitely by Raman spectroscopic measurements in low frequency region.[5-7] Moreover, from the vibrational frequency data obtained by the Raman (the optic phonons) and Brillouin spectra (the acoustic phonons) they were able to get information about thermodynamic as well as mechanical properties of the two basic polytypes.[8,9] As for thermodynamic stability of polytypes in the stearic acid B form, Sato *et al.* predicted by a lattice dynamical calculation of Gibbs energy that Orth II should be more stable than Mon by about 0.7 kJ mol^{-1} in the vicinity of room temperature. Although the energy difference between the polytypes is very small, only one-tenth of that between different polymorphs (for example, it is 6.4 kJ mol^{-1} between the B and C forms of stearic acid), this prediction was substantiated, at least qualitatively, by comparing the solubility for a solution and crystal growth behavior (the frequency of occurrence from solution) between the two basic polytypes.[8,10] As for the
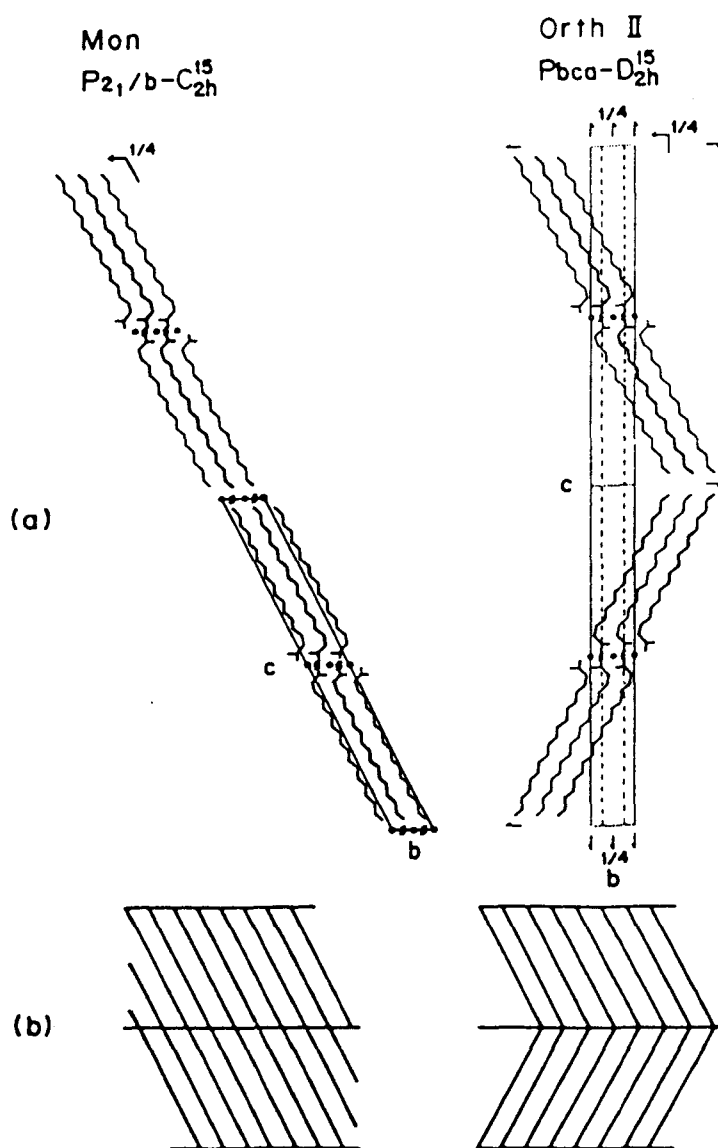
Fig. 1B. (a) Crystal structures of the Mon and Orth Ⅱ polytypes
of stearic acid B.

(b) The schematic representation of the chain orientation.
breath line; the lamellar plane.

comparison of the solubility on the two polytypes, it was found that when single-crystal specimens of Orth II and Mon were put in a nearly saturated decane solution kept at 30.0 ± 0.05°C, the growth of the Orth II crystal took place at the expense of the Mon crystal.[8]   The same result was seen also at 20.0 and 15.0°C.[10] Thus, we concluded that Orth II crystal had a lower solubility for the solution, being more stable, than Mon in the temperature range of 15-30°C.

In addition to polytypism, it has been known that the relative stability of the two polymorphs on stearic acid, B and C, undergoes a delicate change at various temperatures, B is more stable than C below 32°C and this fact is reversed above 32°C.[11-13]   In these previous works, however, the concept of polytypism has been disregarded. Therefore, in order to get a full understanding on the stability of the solid phase relation on stearic acid, the phase diagram must be elucidated by taking both polymorphism and polytypism into account.

In order to approach to this problem, we investigated the overgrowth phenomenon on the seed crystal of a particular polytype of stearic acid B, for example Mon, at the expense of the coexisting crystal of other polytypic and/or polymorphic structure.[8,10]   The polytype structure of the overgrown part was identified by comparing the Raman spectrum in low frequency region of a resultant whole crystal with that of the starting seed crystal. With this method we needed a crystal size large enough to be measured by the ordinary Raman spectroscopy, and we were unable to follow the heterogeneous structural changes that might take place during the overgrown process in the crystal.

In the present work, we made develop the use of the Raman

microprobe technique for the microcharacterization of a polytype structure in a micron-sized domain of the overgrowth crystals. In the optical microscopic viewfield, we observed some growth of spiral steps of Orth Ⅱ of the stearic acid B form on one side surface of the overgrowth crystal in the saturated n-hexane solution at 23°C, when Mon of the stearic acid B was used as a starting seed crystal.

2. Experimental Parts

2.1. Crystal Growth

Single crystal specimens of Mon and Orth Ⅱ polytypes of the stearic acid B form were grown from a n-hexane solution through isothermal crystallization. They were lozenge-shaped plates of 50-200 μm thickness and several millimeter width with an acute interedge of 75°C (the characteristic value of the B form). The basal planes of the crystals are parallel to the crystallographic (001) plane and the a and b axes are located parallel to the acute and obtuse bisectrices of the lozenge, respectively. The polytype structure of every crystal used for the experiment was checked by the low-frequency Raman spectrum.[6] Crystals of the C form having an acute interedge of 55° (the characteristic value of the C form) were obtained in a crystallization process from n-hexane solution either by cooling or by an isothermal method.

A single crystal of B(Mon) (the seed crystal) was put in a small vessel containing a n-hexane solution nealy saturated with the C(Mon) crystal (Fig.2B). The temperature of the solution system was controlled within ±0.02°C in a thermostat. After several hours the seed crystal was picked out of the vessel and was subjected to optical microscopic observation. Fig.3B shows
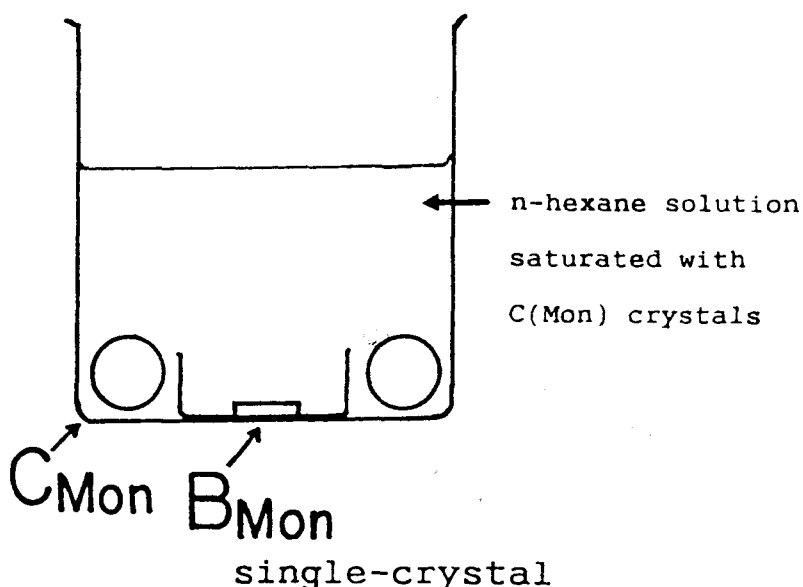
Fig. 2B. The schematic diagram of the preparation of
B(Orth Ⅱ)/B(Mon) overgrowth crystal.

optical micrographs of two basal planes of the overgrowth crystal
after 9 hours at 23°C. There are typical dissolution hillocks on
one surface (a) which contacted the bottom of the vessel, and
growth spiral steps of newly formed crystal on the other surface
(b) which faced the solution. On photograph (b), the measuring
position subjected to microfocus Raman measurement are indicated.
Similar overgrowth experiments were carried out at various
temperatures and by using a seed crystal of B(Orth Ⅱ).

2.2. Raman Microprobe Measurements

     Fig.4B shows the optical system of the Raman microprobe.
The 514.5 nm excitation light (Ar$^+$ laser) polarized in a
particular direction (adjusted by rotating the half-wavelength
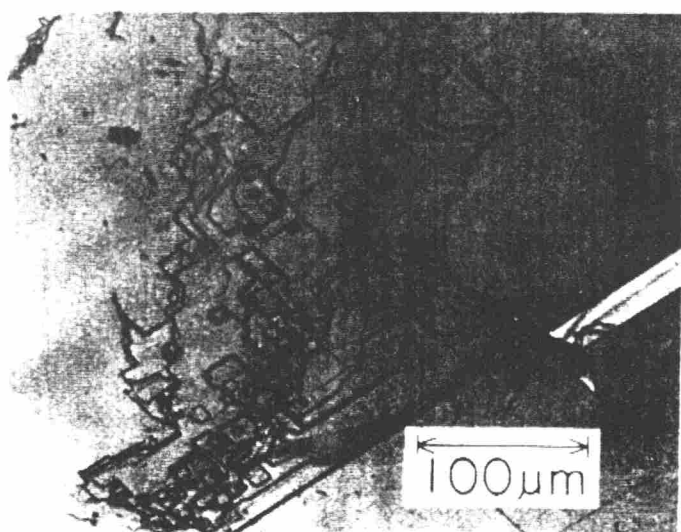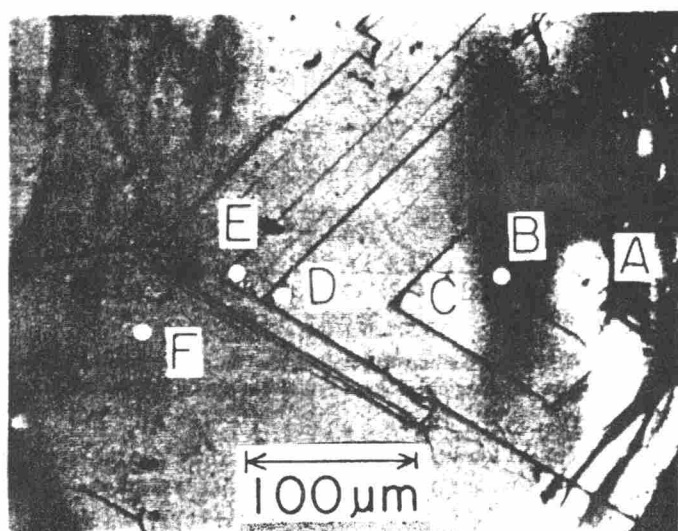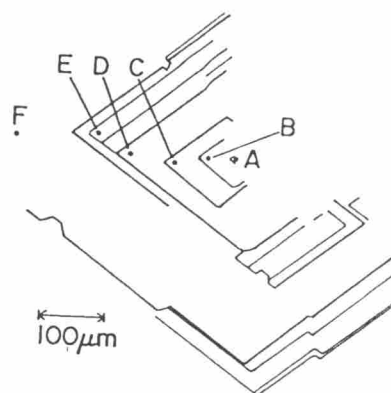
Fig. 3B. Optical micrographs of two basal plane of a B(Mon) seed
crystal of the stearic B form subjected to an overgrowth process
in n-hexane solution saturated with C(Mon) crystals at 23°C for 9
hours.

(a) Dissolution hillocks and (b) growth spiral steps of a newly
formed crystal, the positions subjected to microfocus Raman
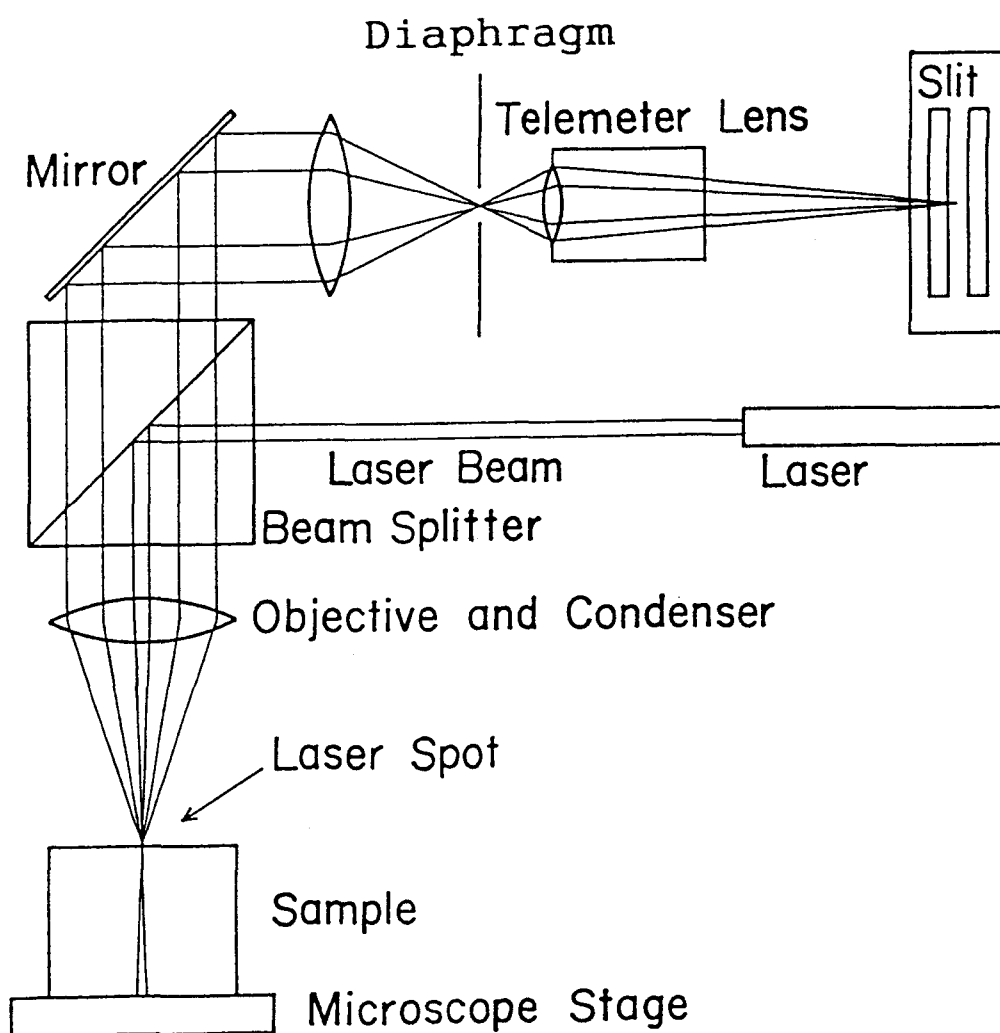measurement being indicated.

Fig. 4B. The optical system of the Raman microprobe.

plate) is focussed on a selected position (on a surface or interior) of the sample on the microscope stage through an objective. The diameter of the laser spot at the focal point depends on the magnification (or the numerical aperture, NA) of the objective used as will be described below. The depth of the focal point measured from the surface of the sample can be adjusted with a microgauge with a precision of 1 μm. The focal position on the crystal surface is monitored by a TV camera. The backward scattered light is collected by the same objective, passes through a beamsplitter, and enters the monochromator through a telemeter lens. Before the entrance slit there are an analyzer and a polarization scrambler as in the case of ordinary Raman measurements. If necessary, an iris diaphragm that acts as a spatial filter is inserted controlling the spatial-resolving power.

Since polytypism is a higher-order structural variation, the difference in polytype structure is reflected in the vibrational spectra in the low-frequency region below 50 cm^{-1}.[5-7] Therefore, the most important task in the present work is to extend the available frequency range to a few reciprocal centimeters. This was achieved by the use of the double monochromator with a 100 cm focal length. Another essential point is to select an optically clear and flat surface of the sample as the measuring position. This is checked in the microscope viewfield by the appearance of well-defined Newton's ring centered at the focal point of the incident laser beam and their smooth movement with the vertical shift of the focal point. With an entrance and exit slit width of 60 μm, which corresponds to ca. 0.5 cm^{-1} spectral resolution, we are able to be free from the interference of the Rayleigh

wings down to 2 cm^{-1}.

Fig.5B shows typical polarized microfocus Raman spectra taken on single crystals of (a) pure B(Mon) and (b) pure B(Orth Ⅱ), using a x100 objective (NA = 0.90 in vacuo). The laser beam was focussed at the (001) surface of crystals. The spectral difference between two polytypes is most conspicuous in the c(ab)$\bar{\text{c}}$ polarization among the polarized spectra. The Raman bands at 21.0 and 6.9 cm^{-1} for B(Orth Ⅱ) and those at 23.3 and 10.5 cm^{-1} for B(Mon) are used as the key bands for the polytype characterization. These low-frequency bands are due to the coupled modes between the rotation (about an axis perpendicular to the dimer chain) and the bend of the dimer chain as a whole. They correspond to the modes of the lowest transverse acoustic branch (TAM mode, one of the ν_9 branches) of the infinitely long polymehtylene chain.[14]

Fig.6B shows the c(ab)$\bar{\text{c}}$ spectra at the surface of the overgrown crystals of stearic acid B form produced at 25°C (upper spectrum) and 19.5°C (bottom spectrum) in the overgrown process used the B(Mon) seed crystals, respectively. The upper spectrum is characteristic of B(Orth Ⅱ), while the lower spectrum is of B(Mon).

3. Micropolytype Structure of Ortho Ⅱ/Mon Overgrowth Crystal of Stearic Acid B Form

We discuss the micropolytype structure of the overgrown crystal (in the overgrowth process of 9 hours at 23°C) of stearic acid B form, the crystal having a transparent lozenge-shaped plate with 3.82 mm long-axis, 2.89 mm short-axis and about 150 μm thikness.

Stearic acid B
(a) Mon

c(ab)c̄

c(aa)c̄

c(bb)c̄

40   30   20   10   0
Wavenumber/cm⁻¹

(b)Orth II

c(a b)c̄
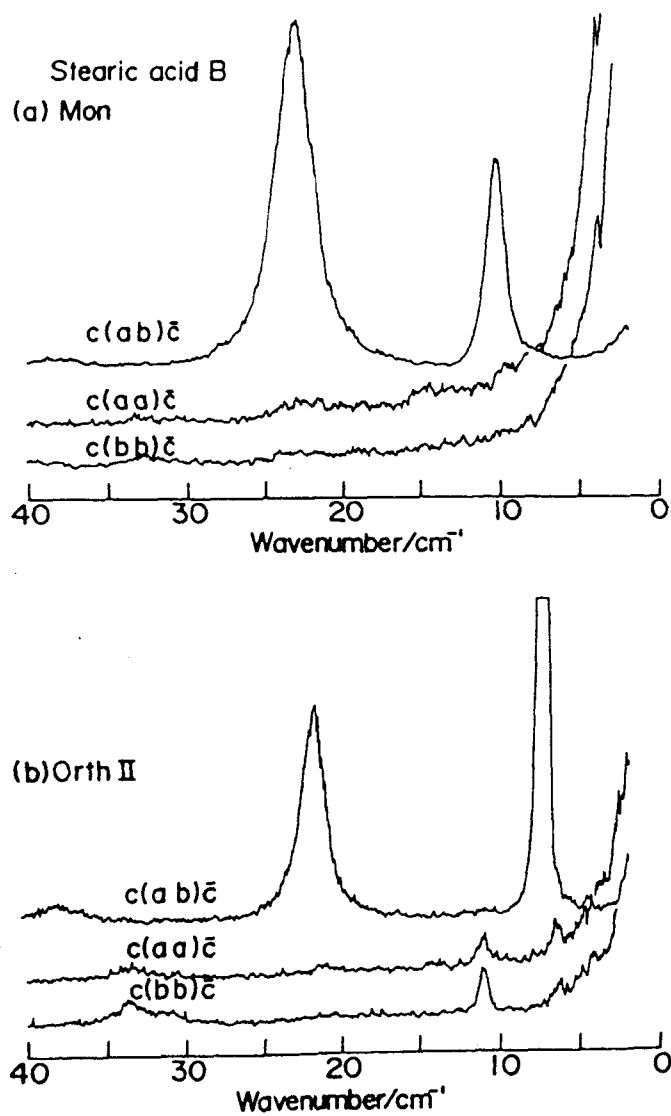
c(aa)c̄

c(bb)c̄

40   30   20   10   0
Wavenumber/cm⁻¹

Fig. 5B. Polarized microfocus Raman spectra taken on a single crystals of (a) B(Mon) and (b) B(Orth Ⅱ), using a x100 objective, F value 4.
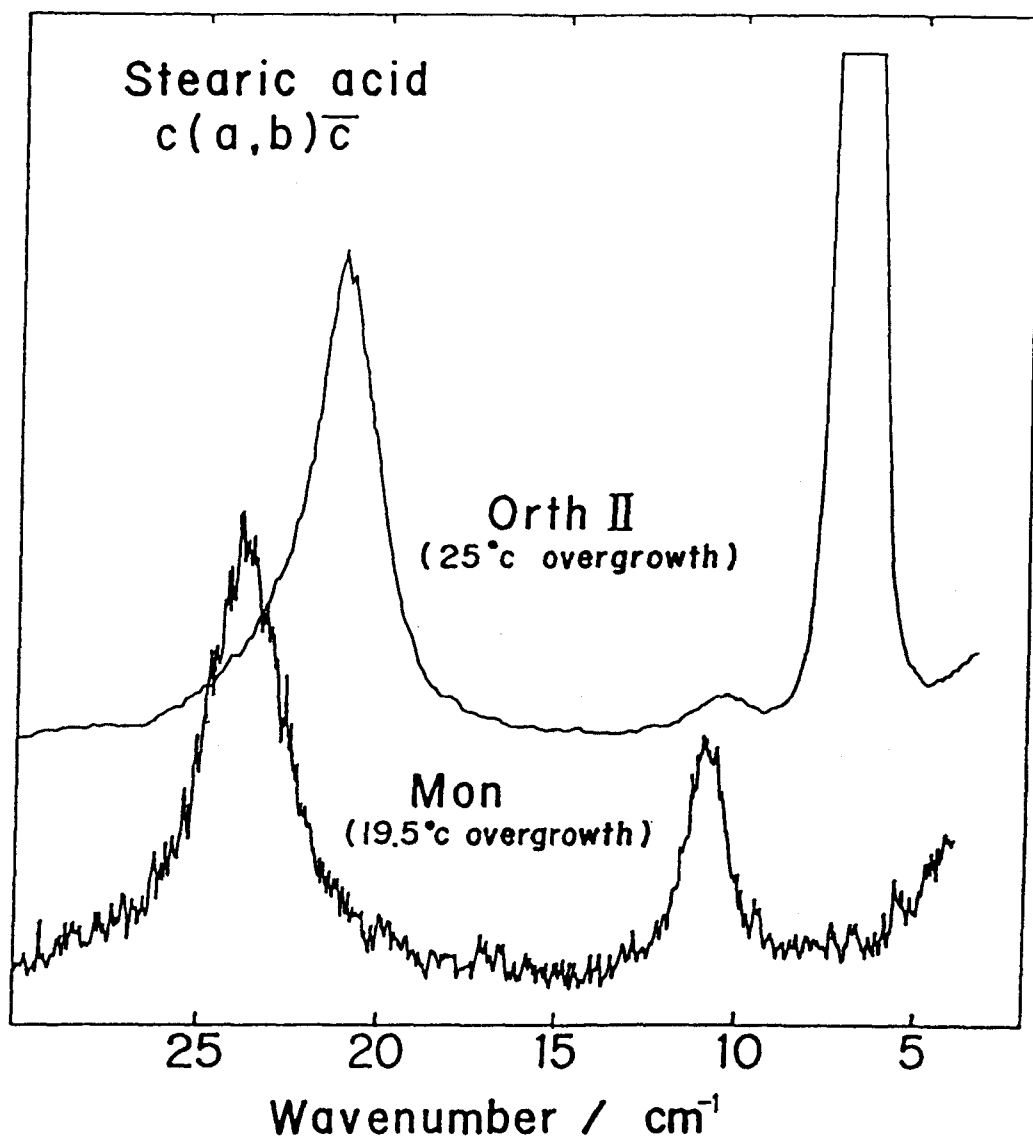
Fig. 6B. The c(ab)c̄ component of the micro-Raman spectra taken on the surface of the overgrowth crystals of stearic acid, using a x100 objective, F value 4.

upper; overgrowth crystal at 25.0°C

bottom; overgrowth crystal at 19.5°C

Fig.7B shows the c(ab)c̄ spectra taken at four different points (A, B, D and F marked in Fig.3B) on the growth spiral steps using objectives of different magnification, x100, x50 and x20, and the diaphragm opening of F = 4. In all cases, the laser beam was focussed at the surface of each step. At point A, the highest step, the spectrum taken with the x100 objective is almost characteristic of pure Orth II containing a small contribution from Mon. The intensities of the Mon bands increase with a decrease in the magnification and also with a decrease in the step heigh, from point A to F. It is clear that spatial resolution along the depth direction depends on the magnification or NA of the objective used.

Fig.8B shows the spectral change with the depth of the focal point (measured from the step surface) taken at point D with the x100 objective and F = 32. In this case, the Mon bands do not appear when the focal point is located at the surface of the crystal. It is shown that the resolution of Raman microprobe is much improved compared with Fig.7B by changing the diaphragm opening (the F value). By shifting the focal point from the step surface into the interior, the spectra change continuously from that typical of Orth II to that typical of Mon below 14 μm at point D. Similar depth profiles were also obtained at other measuring points. These spectral results indicate clearly that the spiral steps overgrown on the B(Mon) seed crystal are of the Orth II polytype structure, and the boundary between Orth II and Mon exists at difinete depth position from the spiral surface. On the other hand, all of the spectra taken at various points on the dissolution hillocks of the reverse surface are typical of Mon (Fig.9B). Thus, a part of the B(Mon) seed crystal (on the
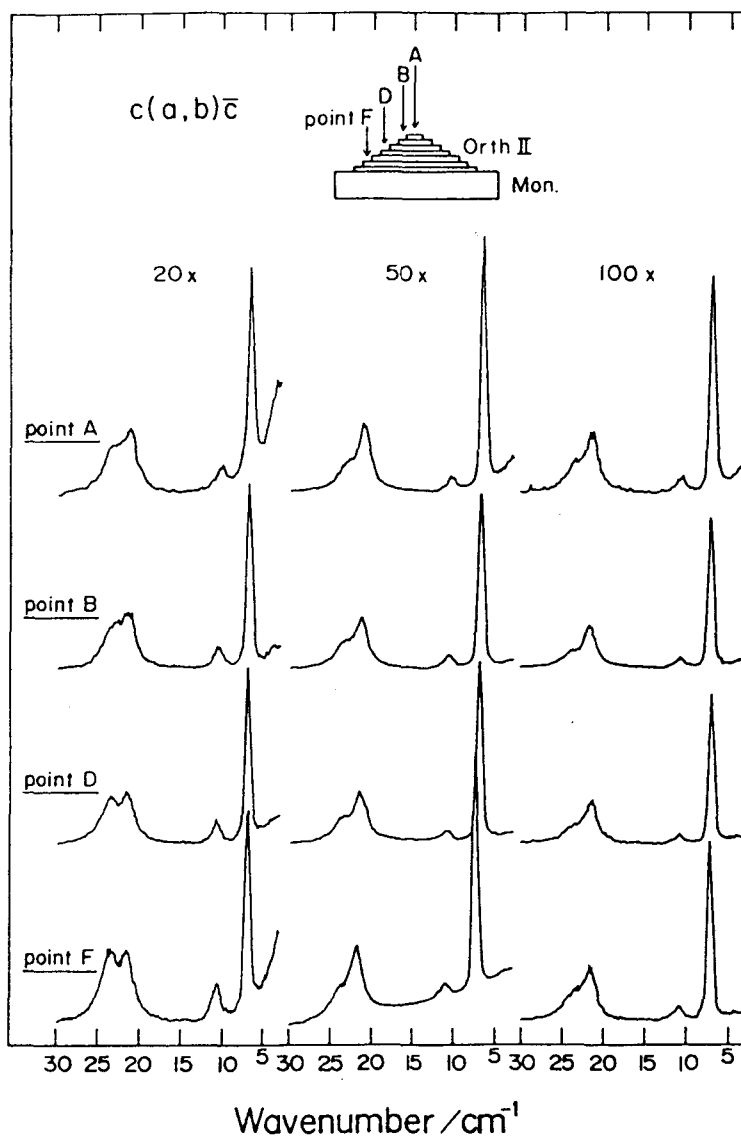
Fig. 7B. The c(ab)c̄ component of the micro-Raman spectra taken at four measuring points on the growth steps in Fig.3B. (b) using objectives of different magnifications, using F value is 4.
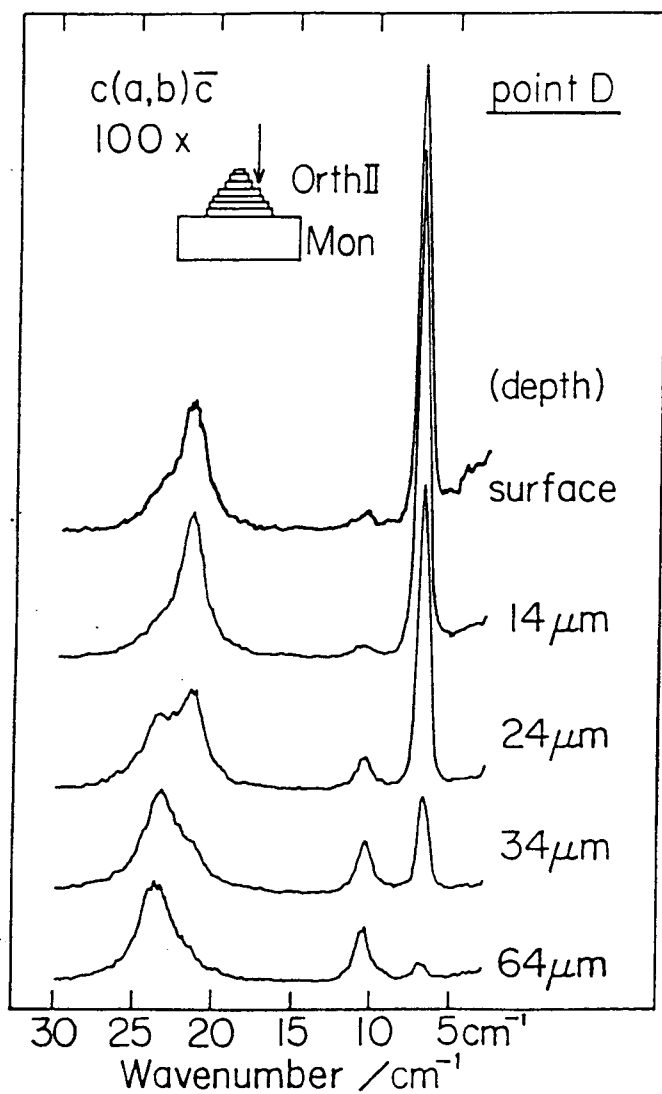
Fig. 8B. The c(ab)c̄ component of the micro-Raman spectra taken at the measuring point D on the depth profile, using a x100 objective, F value 32.

basal plane attached to the bottom of the vessel) dissolves and, at the same time, overgrowth of B(Orth Ⅱ) takes place on the other basal plane that faced to the mother liquor. This process occurs in the temperature range of 32-23°C.

In ref.8, Kobayashi et al. showed by the ordinary Raman measurements that below 22°C a normal overgrowth of B(Mon) took place on a B(Mon) seed crystal. This conclusion was derived from the absence of the B(Orth Ⅱ) bands, even the strongest band at 6.9 cm^{-1}, in the crystals grown in the low-temperature range. In order to confirm the conclusion, the overgrowth steps produced in the low temperature range were investigated selectively by the microscope technique. A B(Mon) seed crystal was put in a saturated n-hexane solution kept first at 19.5°C and the temperature was changed repeatedly between 20.5°C and 18.5°C at intervals of 1 hour. During this process dissolution and crystal growth take place repeatedly. After five cycles, we found that growth spiral steps appeared on the crystal surface. The microfocus Raman spectrum taken by focussing at the step surface was typical of a Mon polytype as shown in the bottom of Fig.6B.

When B(Orth Ⅱ) crystals were used as the seed for the overgrowth experimental, the overgrown part was found always to be of the Orth Ⅱ polytype, indicating that B(Orth Ⅱ) is more stable than B(Mon) over the whole temperature range investigated.

From the experimental results, combined with previous results concerning the relative stability of the B and C forms, the stability relation among the three crystalline phases can be derived. The stability increase in the following order: B(Mon) < B(Orth Ⅱ) < C(Mon) at T > 32°C,[13] B(Mon) < C(Mon) < B(Orth Ⅱ) at 32°C > T ≥ 23°C, and C(Mon) < B(Mon) < B(Orth Ⅱ) at T ≤ 23°C.
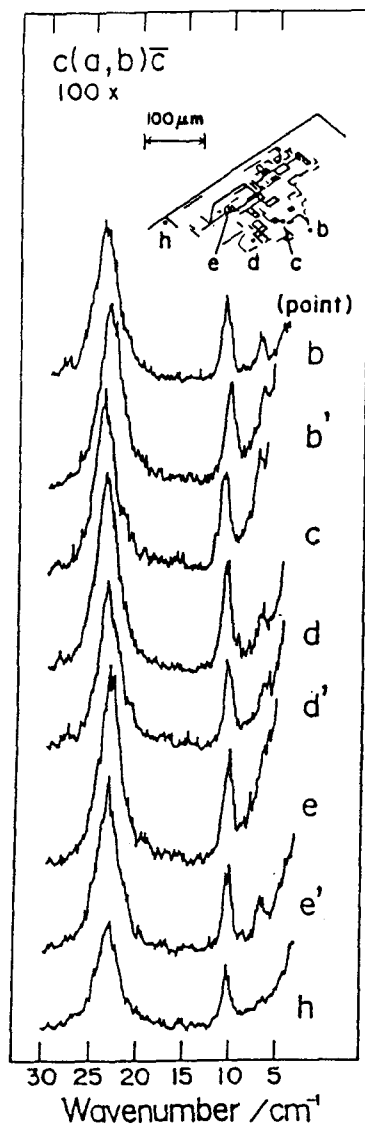
Fig. 9B. The c(ab)c̄ component of the micro-Raman spectra taken at various measuring points on the dissolution hillocks of the reverse surface in Fig.3B. (a), using a x100 objective, F value 4.

4. Application of Raman Microprobe Method

4.1. Observation of the Boundary of Different Polytype Structures

Fig.10B shows the schematic diagram of the scattered light passing through the optical system of the Raman microprobe apparatus. Measured area (inside the circle described in the figure) in the sample depends on diaphragm opening which is inversely proportional to the F value. When the diaphragm is opened, the measured area gets wider (left side of Fig.10B).

Fig.11B shows the schematic diagram of the measured area with small and large circles centered at the focal point that locates at the boundary between B(Mon) and B(Orth Ⅱ) polytypes in an overgrown crystal. Large circle indicates the case of smaller F value, and small one larger F value. The diagram is drawn under the assumption that the boundary plane is parallel to the basal plane of the crystal and the reflection and absorption of the light by the sample are disregarded. If the magnitudes of the Raman tensor of the 23.3 cm^{-1} band due to Mon and the 21.0 cm^{-1} band due to Orth Ⅱ are equal to each other, intensities of those bands become equal when the incident laser beam is focused at the boundary of the two polytypes. If the incident beam is focused upper the boundary, with increasing F value the 21.0 cm^{-1} band due to Ortho Ⅱ becomes strong in intensity, and in the reverse case the 23.3 cm^{-1} band due to Mon becomes strong.

With this idea, we tried to clarify microcharacterization of the overgrowth crystal and to estimate the depth position of the boundary between Mon and Orth Ⅱ in the overgrowth crystal. Fig.12B shows the $c(ab)\bar{c}$ spectra on the depth profile at the measuring point F', the depth of 16 ~ 26 μm at intervals of 2 μm

Diaphragm   Diaphragm
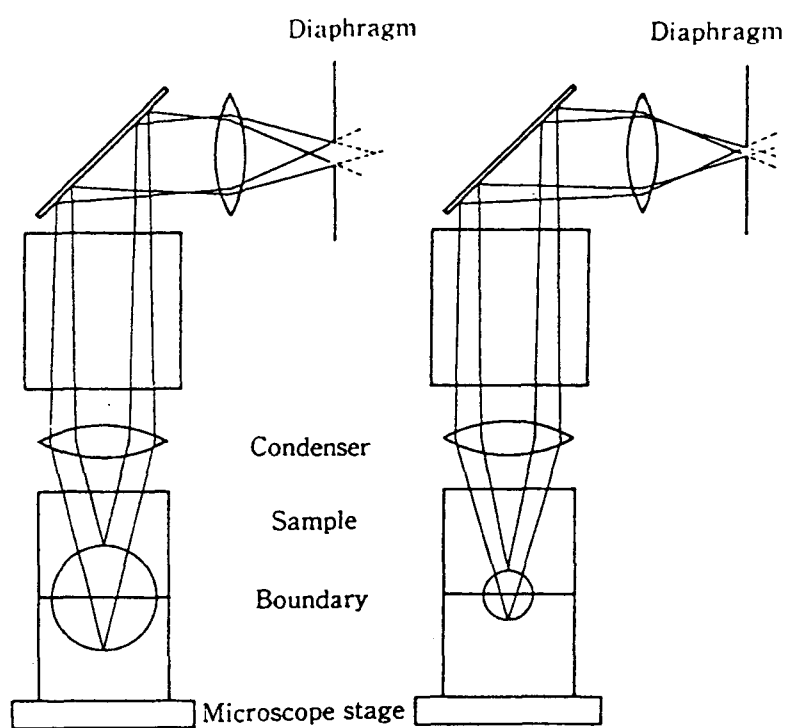
Condenser

Sample

Boundary

Microscope stage

Fig. 10B. The schematic diagram of the detectable regions of the
sample depended on diaphragm opening.

left side; opened up the diaphragm

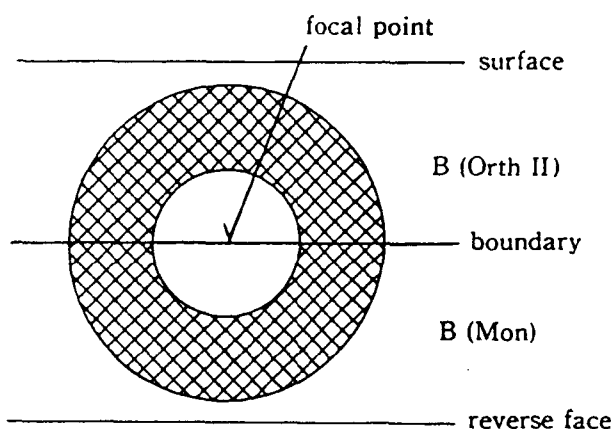right side; closed down the diaphragm

Orth Ⅱ/Mon
Overgrowth crystal

Fig. 11B. The schematic diagram of the detectable regions of the B(Orth Ⅱ)/B(Mon) overgrowth crystal depended on diaphragm opening (F values).

large circle; opened up the diaphragm (a small F value)

small circle; closed down the diaphragm (a large F value)

the hached area; (a small F value) - (a large F value)

with 16 (the dotted line), 22 (the broken line) and 32 (the solid line) of F values, and subtruction spectra of [(F=22) - (F=32)] (left side of the figure). The relative intensities of the 23.3 and 21.0 cm^{-1} bands measured with vaiuos F values were similar to each other in these spectra at 20 μm depth. In the spectra below 18 μm depth, the 21.0 cm^{-1} band due to Ortho II increased in intensity with increasing F value. In the spectra above 22 μm depth, the 23.3 cm^{-1} band due to Mon increased in intensity with increasing F value. Judging from the depth profiles, we concluded that the boundary at the measuring point F' is located at the depth position 20 μm below the spiral surface of the overgrowth crystal, and the overgrown part above the boundary consists of the Ortho II polytype and the lower part consists of Mon. In other measuring points of the overgrowth crystal, the boundary of the two polytypes was found to locate around 20 μm depth.

4.2. Removing of Polarization Scrambling Effect on Polarization Measurements in Micro-Raman Spectrometry

In Chapter 2, we mentioned the importance of the polarization scrambling effect in considering the microfocus spectra. We investigated further the polarization scrambling phenomena in the micro-Raman technique.

Fig.13B shows the micro-Raman spectra (with x100 objective) of the moth-shaped single crystal of o-POM. The Z(XX)$\overline{Z}$ and Z(XY)$\overline{Z}$ spectra were measured by ordinary back scattering. The Z(XX+XY)$\overline{Z}$ spectrum was measured by setting the polarizer parallel to the X direction of the single crystal and without analyzer. In the Z(XX+XY)$\overline{Z}$, Raman bands due to the A species (marked in the
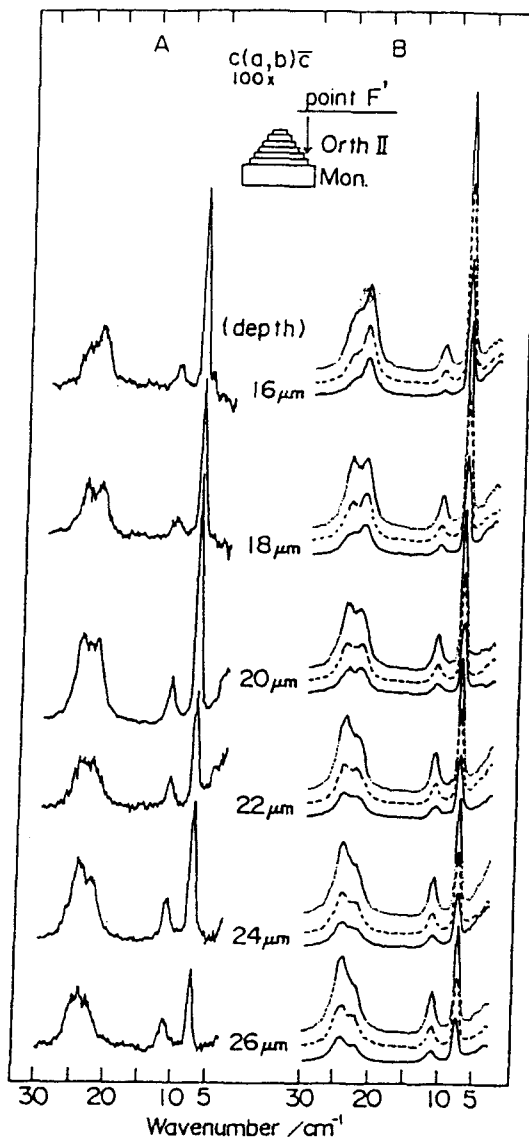
Fig. 12B. The c(ab)c̄ component of the micro-Raman spectra taken

at the measuring point F' on the depth profile.

right side: the dotted line; F = 16, the broken line; F = 22,

          the solid line; F = 32

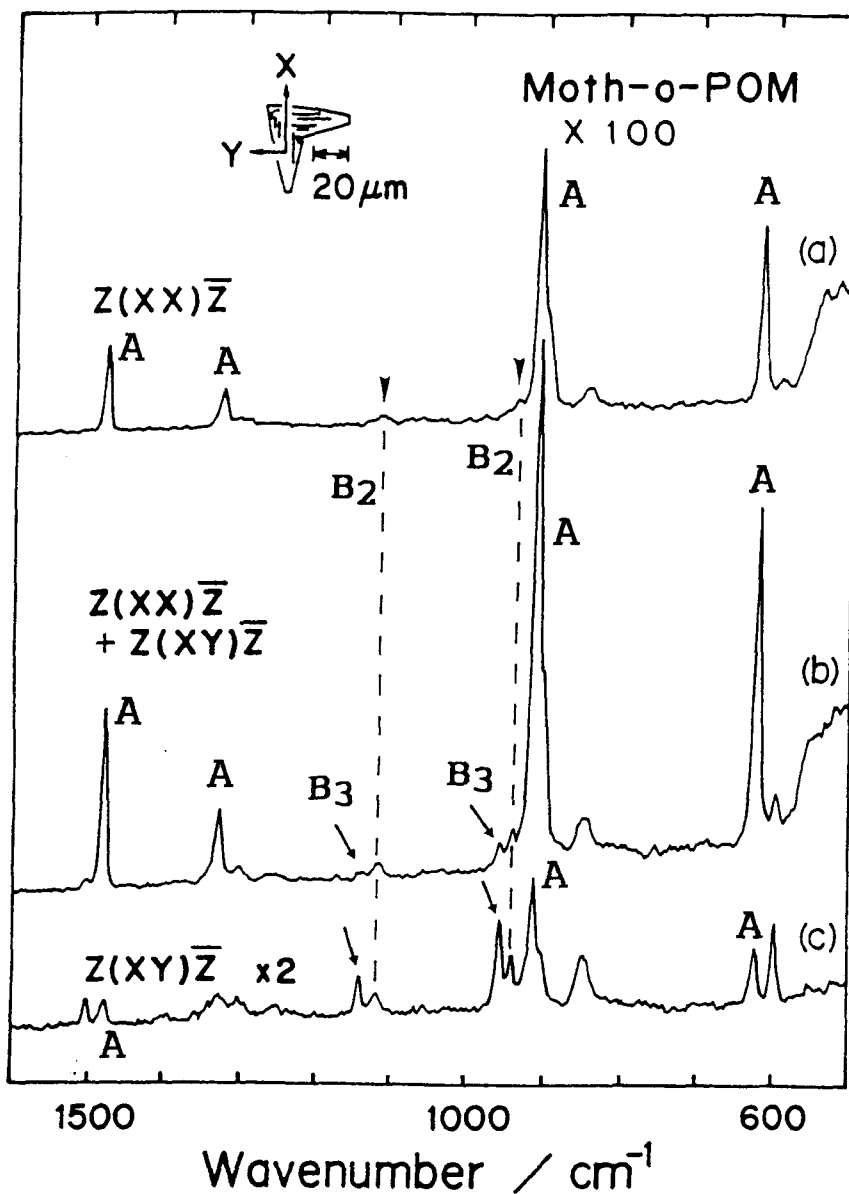left side: the subtruction spectra of (F = 22) - (F = 32)

Fig. 13B. The effect of polarization scrambling on B_2 vibrational modes in the (XX) and (XY) polarizations of moth-shaped o-POM single-crystal with x100 objective. the middle spectrum; without an analyzer

figure) were observed strongly, and the B_2 and B_3 bands were observed weakly. The relative intensities of the B_2 and B_3 modes in Davydov split pairs observed around 1120 and 950 cm^{-1} were almost similar to each other. In the $Z(XY)\bar{Z}$, the B_3 modes (marked with arrows) were observed more intensely than the B_2 modes (described in Chapter 2). In the $Z(XX)\bar{Z}$, the B_2 bands (marked with arrowheads) were observed due to the polarization scrambling effect in addition to the inherent A modes, but the B_3 modes were not observed. These facts indicate that the B_3 modes originally having (cb) components appear in the $Z(XY)\bar{Z}$ [a(cb)$\bar{a}$], and in the a(cc)$\bar{a}$ the B_3 modes are not mixed into the inherent A modes having (cc) components but the B_2 modes having (ca) components are preferentially mixed and observed selectively. These spectral results concerning the polarization scrambling in the micro-Raman measurements have been supported theoretically by Turrell *et al.*[15,16]

Fig.14B shows the micro-Raman spectral changes in the $Z(XX)\bar{Z}$ and $Z(YX)\bar{Z}$ before (b) and after [(c), and (a)] the insertion of the aperture I or aperture II (see Fig. 2.2). The objective x100 was used, and the focal position of the incident beam was fixed at the crystal surface. The aperture I cuts peripheral parts of the laser beam (incident light), and the aperture II cuts the scattered light which passes through the peripheral area of the objective. By inserting these apertures, the relative intensities of the polarization scrambling components decreased. It was clear that the Raman bands marked with arrows in the $Z(YX)\bar{Z}$ spectra appeared as the polarization scrambling components.

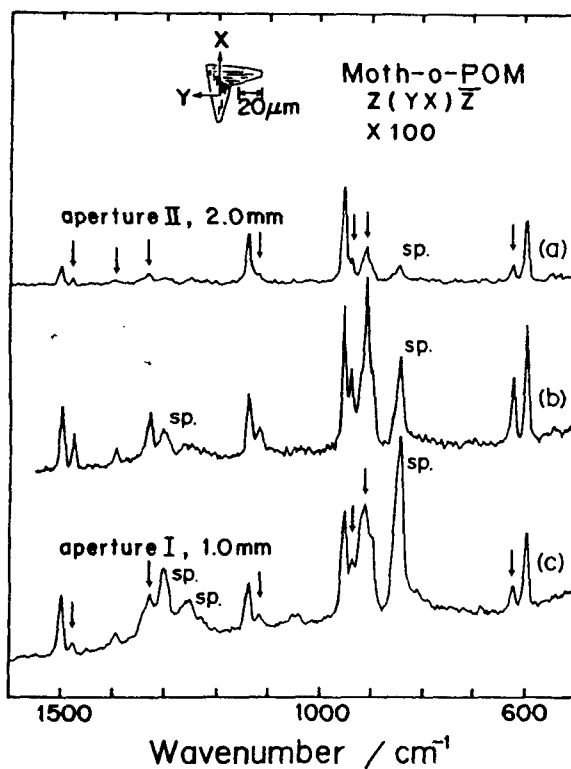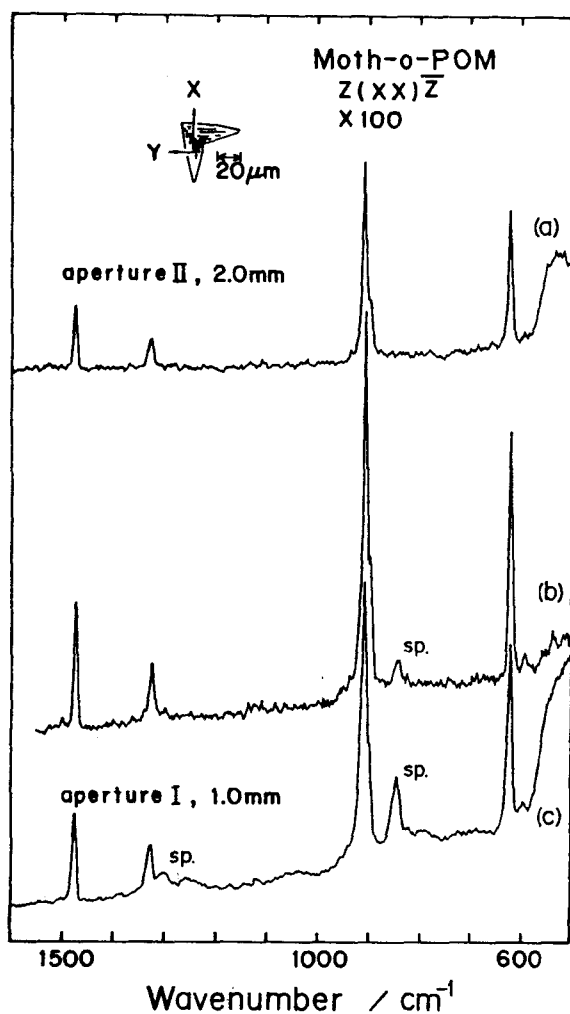These observations of the polarization scrambling in the

Fig. 14B. Spectral change based on polarization scrambling by insertion of the aperture I with diameter of 1 mm (bottom), and the aperture II with diameter of 2 mm (upper) in the (XX) and (YX) polarizations. Bands marked with sp. are bands induced by objective itself.

micro-Raman technique are useful so as to assign the Raman-active fundamentals and to decide the orientation of a micron-sized single crystal.

4.3. Limitations of Detection by the Raman Microprobe Technique

Although the micro-Raman technique is used for the in situ measurement of micron-sized samples, sharply focused laser irradiation induces phase changes or decomposition of the samples unless the thermal energy converted from the light is liberated effectively. We succeeded to measure polarized Raman spectra of the needle-like t-POM single crystal having a hexagon-shape with about 2 μm diameter. The laser power used was 200 mW. The single crystals usually suffer damage (melting and decomposition) even when such a low power as 80 mW was supplied to the laser. In order to liberate the energy, the incident beam was defocused a little to reduce the power density, and the single crystal was fitted onto a slide glass. Use of a cold stage cell and a water immersion objective would be expected to reduce thermal decomposition.

Fig.15B shows polarized micro-Raman spectra of a feather-shaped single crystal of t-POM less than 1 μm thickness having a thin platelet with twin habit as large as about 5 μm width.[17,18] The Raman measurement was made at 5°C with 200 mW laser power for a sample put on a brass plate in order to liberate thermal energy. This measurement shows limitation of detection for the thickness of polymer samples by this method.

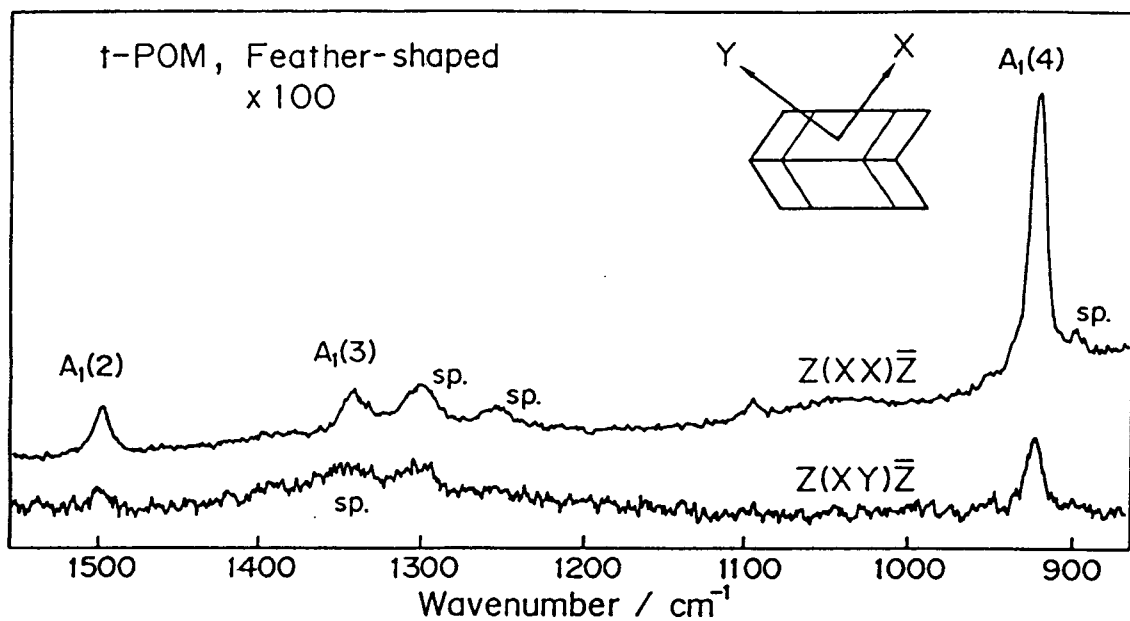These methods are applicable also to microdomain analysis in other organic materials.

Fig. 15B. Polarized micro-Raman spectra of feather-shaped single crystal of ECC t-POM. Bands marked with sp. are bands induced by objective itself.

REFERENCES

1   S. Amelinckx, Acta Crystallogr., 8, 530 (1955). 9, 16
    (1956). 9, 217 (1956)

2   H. M. M. Shearer and V. Vand, Acta Crystallogr., 9, 379
    (1956)

3   M. Goto and E Asada, Bull. Chem. Soc. Jpn., 51, 2456 (1978)

4   R. Boistelle, B. Simon and G. Pepe, Acta Crystallogr., Sect
    B, 32, 1240 (1976)

5   M. Kobayashi, T. Kobayashi, Y. Itoh, Y. Chatani and
    H. Tadokoro, J. Chem. Phys., 72, 2024 (1980)

6   M. Kobayashi, T. Kobayashi, Y. Itoh and K. Sato, J.Chem.
    Phys., 80, 2897 (1984)

7   M. Kobayashi, K. Sakagami and H. Tadokoro, J. Chem. Phys.,
    78, 6391 (1983)

8   M. Kobayashi, T. Kobayashi,Y. Itoh and K. Sato, Bull.
    Mineral., 109, 171 (1986)

9   M. Kobayashi, T. Kobayashi, Y. Cho and F. Kaneko, Makromol.
    Chem. Macromol. Symp., 5, 1 (1986)

10 K. Sato, M. Kobayashi and H. Morishita, J. Crystal Growth.,
    87, 236 (1988)

11 K. Sato and R. Boistelle, J. Colloid Interface Sci., 94, 593
    (1983)

12 W. Beckmann, R. Boistelle and K. Sato, J. Chem. Eng. Data,
    29, 211 (1984)

13 K. Sato and R. Boistelle, J. Crysta Growth, 66, 441 (1984)

14 M. Tasumi, T. Shimanouchi and T. Miyazawa, J. Mol.
    Spectrosc., 9, 117 (1963). 11, 422 (1963)

15 G. Turrell, J. Raman Spectrosc., 15, No.2, 103 (1984)

16 C. Bremard, P. Dhamelincourt, J. Laureyns, and G. Turrell,

Applied Spectrosc., **39**, No.6, 1036(1985)

17 M. Iguchi, H. Kanetsuna and T. Kawai, Makromol. Chem., **128**, 63 (1969)

18 M. Iguchi, Br. Polym. J., 5, 195 (1973)

.

.